ADVANCED ELECTRON BEAM EVAPORATION

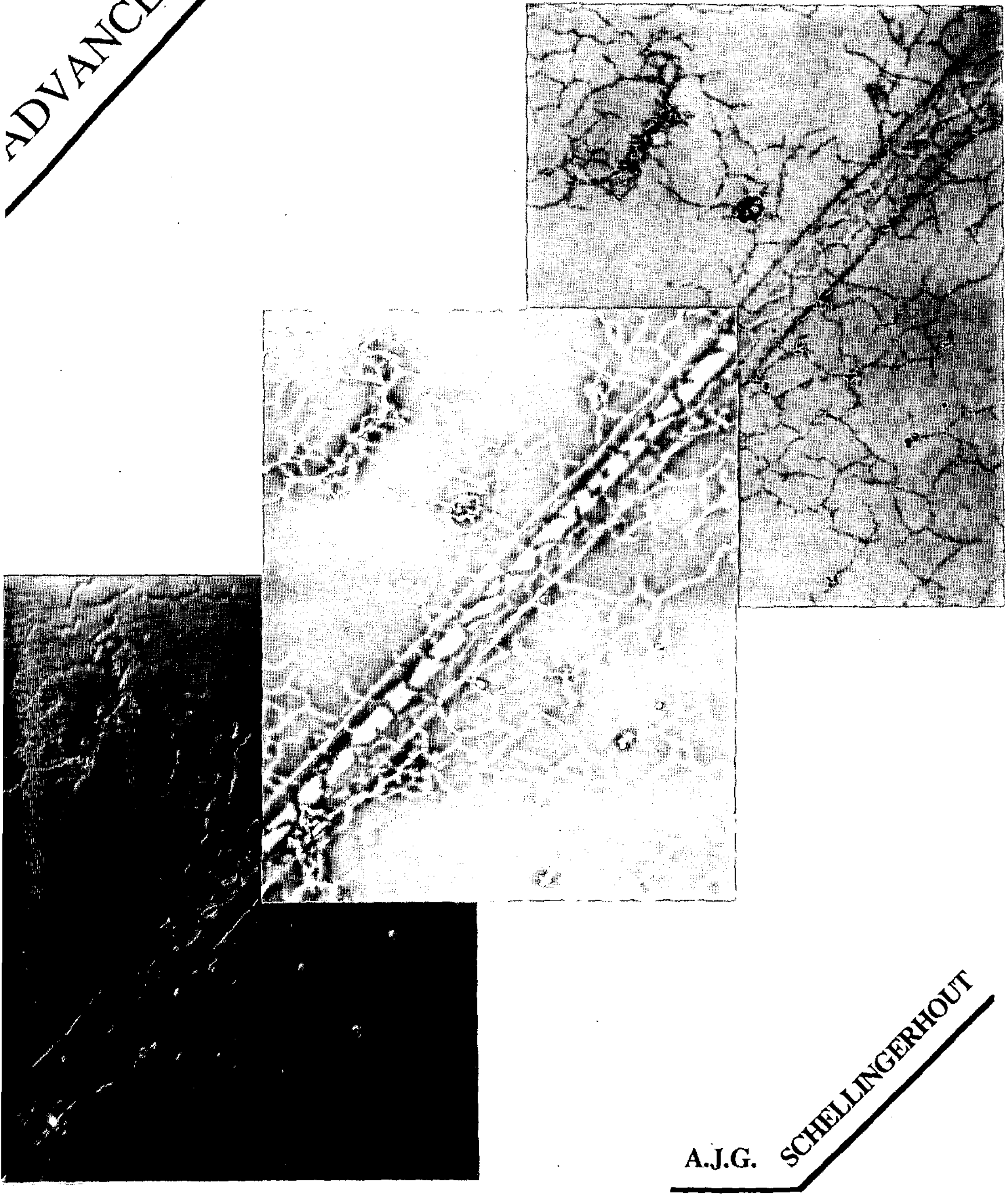

A.J.G. SCHELLINGERHOUT

ADVANCED ELECTRON BEAM EVAPORATION

ADVANCED ELECTRON BEAM EVAPORATION

Proefschrift ter verkrijging van de graad van doctor aan de Technische
Universiteit Delft, op gezag van de Rector Magnificus,
prof. drs. P.A. Schenck,
in het openbaar te verdedigen ten overstaan van een
commissie door het College van Dekanen daartoe aangewezen, op

dinsdag 6 september 1988 te 14.00 uur

door

Abraham Jacob Guillaume Schellingerhout

geboren te Gouda

natuurkundig ingenieur

krips repro meppel

Dit proefschrift is goedgekeurd door de promotoren
Prof.dr.ir. J.E. Mooij en Prof.dr.ir. T.M. Klapwijk

Financiële steun voor het in dit
proefschrift beschreven onderzoek is verleend door de
Stichting voor Fundamenteel Onderzoek der Materie (FOM).

voor

een

boekenkast

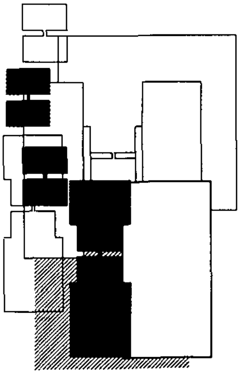

Table of contents

Chapter 1 Introduction

Advanced electron beam evaporation 1
Deposition 2
Junction fabrication 4
Results 7
References 9

Chapter 2 Rate control for electron gun evaporation

Introduction 11
Theory 12
E-guns 15
Sensors 17
Mass spectrometer 19
Rate controller 20
Beam profile 24
Conclusions 26
References 27

Chapter 3 Mass spectrometer controlled fabrication of Si/Ge superlattices

References 34

Chapter 4 Critical thickness for pseudomorphic growth of Si/Ge alloys and superlattices

Introduction 36
Critical thickness 38
Superlattices 44
Energy barrier and strain 47
Discussion 50
Conclusions 51
References 52

Chapter 5 Fabrication of low-capacitance josephson-junctions

References 54

Chapter 6 Oxygen concentration and microstructure of granular aluminium

Introduction 58
Fabrication 59
Oxygen incorporation 61
Oxygen concentrations 63
Calculated resistivities 67
Conclusions 71
References 72

Chapter 7 Strong electric field effect in granular aluminium
References 82

Chapter 8 Analysis of $Y_1Ba_2Cu_3O_{7-y}$ thin films on sapphire substrates made by electron beam evaporation
Introduction 85
Fabrication 85
Results before annealing 87
Results after annealing 88
Conclusions 92
References 93

Appendix I Growth and characterization of a sinusoidally modulated Nb/V superlattice
References 98

Appendix II Critical modulation amplitude in monocrystalline Nb/V and Ta/V superlattices
Introduction 101
Growth 101
Elastic energy 102
Results and discussion 103
Conclusion 105
References 105

Appendix III A strong voltage dependence of the conductivity in granular aluminium
Introduction 107
Experimental 107
Measurements 108
Discussion and conclusion 109
References 111

Appendix IV Ion source
References 112

Summary 114

Samenvatting 116

Levensloop 118

INTRODUCTION

ADVANCED ELECTRON BEAM EVAPORATION

This thesis contains a collection of papers which have at a first glance little in common. However, they have all been written in the course of a project to develop an advanced technology to fabricate superconducting junctions with a barrier material which has a metal insulator (MI) transition. The title of this thesis is based on the common aspect shared by almost every chapter, namely the fabrication of complex multilayers and alloys by electron beam evaporation. As every chapter of the thesis has been written as a separate paper, some topics are discussed more than once (especially the evaporation system). The author apologizes for this inconvenience.

The research project was started to fabricate submicron Nb_3Sn Josephson junctions. The junctions made with this (old) high T_c material have the advantage of a twice larger product of the critical current and the resistance, which gives the possibility of faster and more sensitive devices. The interest was mainly initiated by the research on and fabrication of a superconducting computer by IBM. The expectation was that there would be an increasing interest in these superconducting junctions in the future. However, IBM cancelled the research program for the super conducting computer just at the beginning of the project for the fabrication of the Nb_3Sn Josephson junctions (1-12-1983). A reconsideration was necessary. The decision was taken to change the project into an investigation of the properties of a possible new class of barrier materials.

Superconducting tunnel junctions consist of two superconducting electrodes separated by a thin insulator (1 -3 nm). Quantum mechanical tunneling of electrons through a potential barrier causes the electric conduction. [1] The junctions with a high current density have very thin insulating layers between the electrodes. A different type of superconducting junctions is a SNS- junction which has two superconducting electrodes (S) separated by a normal (non-superconducting) metal (N). The electrical transport is caused by diffuse electron motion. Probably there is a gradual transition from the thin insulating layer barrier with electron tunneling to a normal metal barrier with diffuse electron transport. The barrier should be made of a material with a metal-insulator transition. This transition is a continuous change in the conductivity from a metal to an insulator as a function of the concentration of the constituents in the barrier material. This transition is observed in several materials like Nb_xSi_{1-x}, [2] granular aluminium [3] and Au_xGe_{1-x} .[4] At the critical composition the conductivity will become zero when the temperature falls to zero Kelvin. Tunneling measurements on these materials showed that the density of states at the Fermi level also approaches zero at this transition. By a study of electrical conduction of superconducting junctions as a function of barrier composition and barrier thickness, we wanted to obtain a better understanding of the cross-over from diffuse electron transport into transport by electron tunneling. Furthermore, this investigation would possibly lead to a better understanding of the electrical conduction of the barrier material itself. The barrier material was planned to be Nb_xSi_{1-x}.

In order to realize this research project two important technical problems had to be solved. First, the deposition control. The material for the barriers exhibit a metal insulator transition as a function of the composition, which means that in order to fabricate homogeneous layers with a controlled composition, the deposition control is crucial. The barrier materials are evaporated in an ultra high vacuum system with two electron gun evaporators. Second, the junction fabrication. In order to study the physical properties of the barrier a junction fabrication method must be used which does not influence the barrier properties. Thus a well defined junction process had to be developed.

DEPOSITION

The materials are deposited by electron beam evaporation in an ultra high vacuum system. The system is shown in fig.1. The system is pumped with a turbo molecular pump, a titanium sublimator, and many cryo panels. It is, after the proper procedures, capable of evaporating materials in a background pressure of 10^{-7} to 10^{-6} Pa.

The substrates can be placed into two heaters. One has a temperature range from 120 K to 900 K in which the substrates are placed parallel to the centers of both electron guns to obtain a phase-spread in the deposited layers. The second heater has a temperature range from room temperature to 1300 K, in which the substrates are placed to minimize the phase-spread. The special feature of this evaporation system is the control of both fluxes of the electron gun evaporators. Both fluxes are measured with a single mass spectrometer which is switching every 16 ms between the mass numbers of the two evaporated materials. The signal of the mass spectrometer is demultiplexed into two signals of the evaporation rate of both electron guns. This rate is stabilized by applying feedback to the filament and the wehnelt of the electron guns.

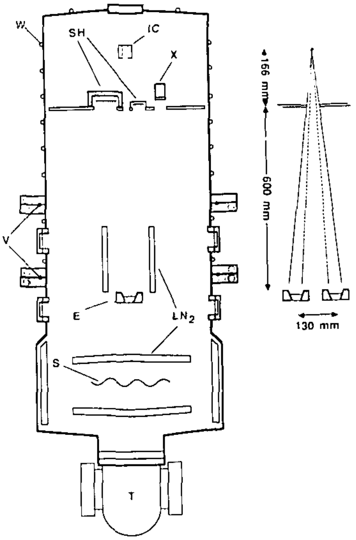

Fig.1 Schematic drawing of the evaporation system. LN_2 = liquid nitrogen panels. S = titanium sublimator. T = turbo molecular pump. E = electron gun evaporator. V= viton rings. IC = mass spectrometer. X = quartz crystal. SH = sample holders. W = water cooling.

This stability is crucial for the fabrication of materials with a metal insulator transition. The system was originally equipped with manufacture-supplied feedback electronics, but many reproducibility and reliability problems resulted in the redesign of many components. The final set-up for the rate control feedback is shown in fig. 2. Important general aspects of the rate control of electron-gun evaporators are discussed in chapter 2

During the same period the system was used for a project to fabricate metallic superlattices. [5] The fabrication of these materials also depends heavily on the rate stability of the components. These superlattices were used to gain experience with the UHV system and led to improvements of the system including the rate control. Some of the results are discussed in appendix I and II.

With the experience gained by using the UHV system, it was possible to reduce the pressure during evaporation. In this way epitaxial growth of silicon and germanium became feasible. Successful attempts have been made to fabricate high quality single crystal silicon germanium superlattices. These layers have been studied by X-ray diffraction to obtain the rate stability of the feedback system. This discussion is given in chapter 3.

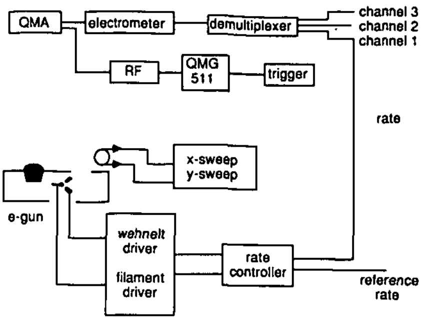

Fig.2 Schematic drawing of the rate control system. QMA = ionization chamber and mass selection. RF = radio frequency generator. QMG511 = mass spectrometer. The rate controller is shown in a separate drawing.

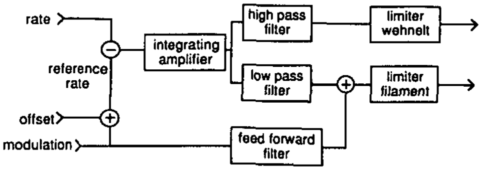

RATE CONTROLLER

The critical thickness for dislocation-free growth of SiGe alloys is a controversial and puzzling problem. Si_xGe_{1-x} alloys have a lattice-constant larger than the lattice-constant of the Si substrate on which the alloys are epitaxially grown. The elastic energy increases with the thickness of the alloy. Dislocations emerge at the critical thickness to reduce the elastic energy in the epitaxial layer. In chapter 4, the critical thickness of SiGe superlattices is discussed.

JUNCTION FABRICATION

The junction fabrication method which had to be developed was the selective niobium anodization process (SNAP). [6] The favorable property of this process is that the fabrication of the three layers occurs without breaking the vacuum, with the processing to a junction afterwards. In this project the three layers are a bottom layer of Nb, a Nb_xSi_{1-x} barrier, and a Nb top electrode. This method of junction fabrication results in well-defined samples. The SNAP is capable of making small junctions with dimensions in the order of microns. This is necessary for the $Nb/Nb_xSi_{1-x}/Nb$ trilayers in order to be able to neglect the influence of the upper contact electrode on the measurements .[7] The estimated resistance of the junction must be much larger than the resistance of the contact layer on top of the junction area .

The fabrication process for the junctions is shown in fig. 3.

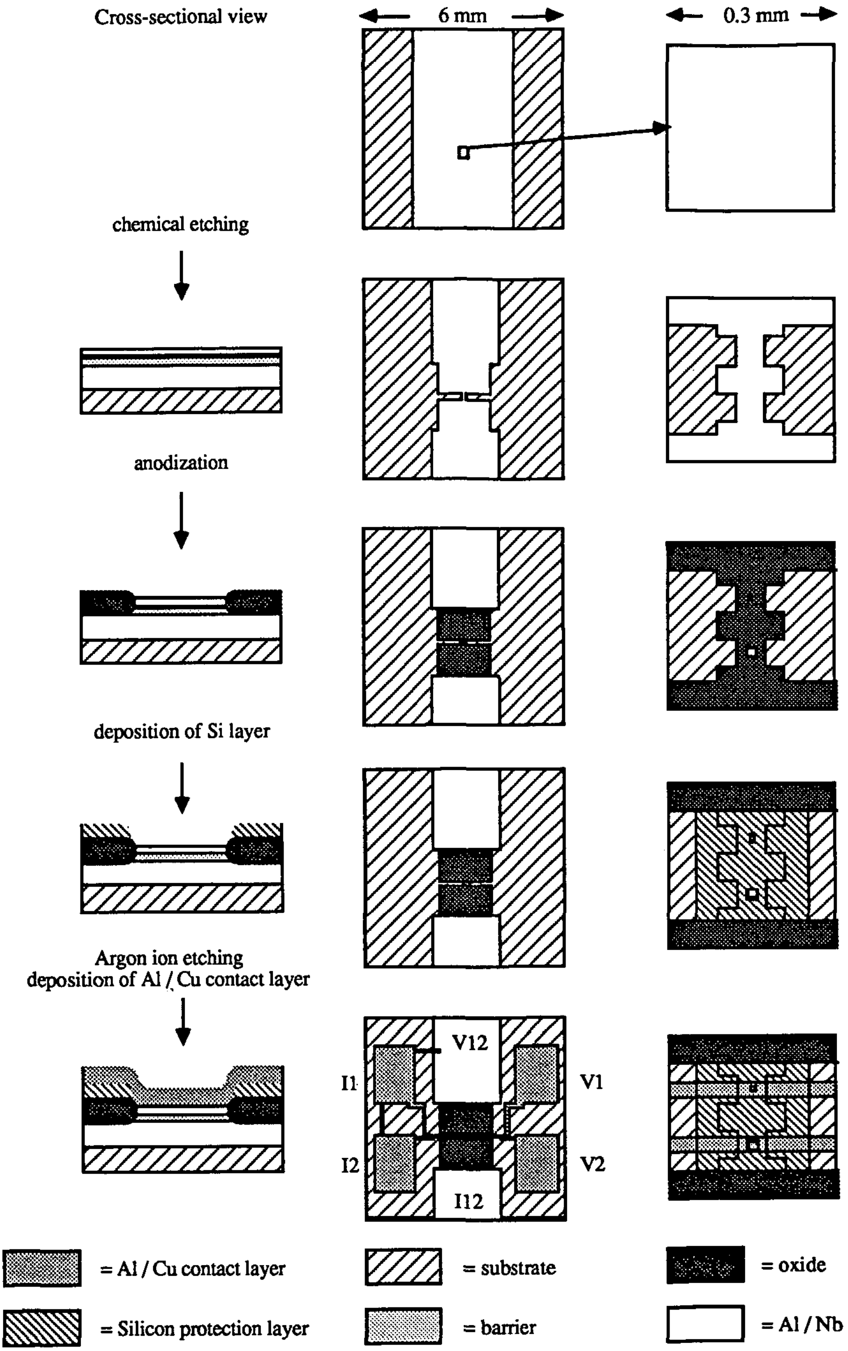

Fig. 3 Junction fabrication process

It is applied for Nb/barrier/Nb and Al/barrier/Al trilayers. The reason for the aluminium version of the process is given in the following paragraph. The junction fabrication has the following stages. (1) A pattern is chemically wet etched in the evaporated trilayer. This step reduces the possibility of short circuits and makes aligning feasible with the photoresist patterns of the following fabrication stages. (2) The trilayer is anodized. Niobium in a solution of 34 ml g H_2O, 76 ml ethylene glycol and 4 g $(NH_4)_2SO_4$ and aluminium in a solution of 3% H_3PO_4 in H_2O adjusted to a pH = 7 with KOH. The photoresist pattern is made with two exposures in which the coarse pattern is made with proximity printing. The small squares are patterned with a projection microscope. [8] (3) A silicon protection layer is evaporated to reduce the possibility of non-defined current paths. The lift-off of the silicon layer is improved with a chlorobenzene soak. [9] (4) The last step is the deposition of an aluminium or copper contact electrode. But before this layer is deposited, metal oxide on top of the upper aluminium or niobium layer must be removed. This is performed by sputtering with argon with an ion source, which is placed in the vacuum chamber in which the contact electrode is deposited. The ion gun was home-built according to a design of Harper. [10] Some of the technical drawings of the ion source are shown in appendix IV. The ion source was used to make a bridge structure for the fabrication of low capacitance Josephson junctions. This is discussed in chapter 5.

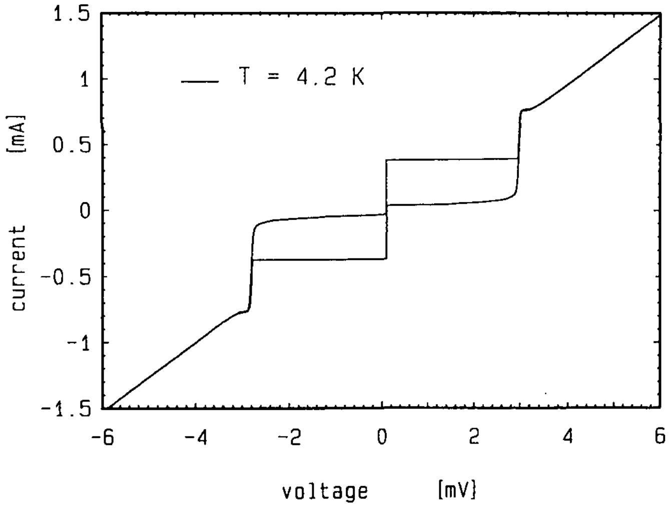

Fig.4 I-V characteristic of a Nb/Al Al_2O_3 Al /Nb Junction.
The temperature is 4.2 K.

The junction fabrication process was tested on a Nb/Al Al_2O_3 Al/Nb [11] and $Al/Al_2O_3/Al$ trilayers. Figure 4 shows the superconducting gap structure of the Nb junction. Figure 5 shows the tunnel characteristic of an Al junction. The barrier height is 2.5 eV and the barrier thickness is 1.6 nm. [12 13]

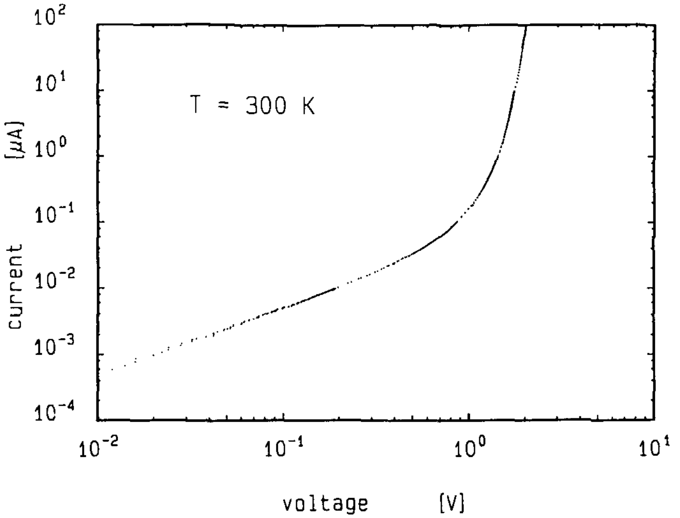

Fig.5 I-V characteristic of a Al /Al_2O_3 /Al tunnel junction. The temperature is 300 K.

RESULTS

Layers of Nb_xSi_{1-x} were deposited. The measurements of these layers have been compared to published results.[2] The metal insulator transition was observed in the material and the layers showed the same temperature dependence. However, the conductivity as a function of the concentration was much steeper than expected. The concentration measurements showed a much larger prefactor K in the relation $\sigma = K\ (n-n_c)^{\nu}$ with n_c is the critical concentration. This larger prefactor can also be extracted from other reported data. [14]

Granular aluminium has, as NbSi, a metal insulator transition. The samples for these investigations have been fabricated with conventional deposition techniques. The selective anodization process could also be applied to aluminium since aluminium is easy to anodize. This method of making aluminium junctions is, apart from making Al/granular aluminium/Al junctions, interesting because many complex structures can be fabricated in combination with the selective chemical wet etching of Al and of Al_2O_3.[15] The structures of the type $Nb/Nb_xSi_{1-x}/Nb$ and Al/granular aluminium/Al could be developed easily in parallel because of the similarities in fabrication technology. The interesting reason to investigate both systems is the difference in micro-structure. NbSi is amorphous while granular aluminium consists out of metallic grains of approximately 3 nm embedded in an insulating matrix of Al_2O_3 .

When the junction fabrication and the deposition control could be routinely used, we started with the granular aluminium barriers hoping for an easier deposition control. It turned out that this hope was in vain. In chapter 6 measurements on granular aluminium layers are discussed. A different application of the anodization of aluminium is discussed in chapter 6 as well. It can be used to determine the oxygen concentration in the granular aluminium.

The first samples which were electrically characterized had a barrier of granular aluminium with a thickness of a 100 nm. This barrier was made to test the geometry by the verification of known properties of granular aluminium. However, these barriers showed a unexpected strong non-linear conduction. Appendix III gives the first interpretation. A possible explanation for the non-linear resistance is discussed in chapter 7.

After the revolutionary discovery of a new class of high T_c materials,[16] it became important to fabricate thin layers of these materials. The UHV system was very suitable because of the rate control of the fluxes. The layers were evaporated in a three-week interval beginning at 4 May 1987. The results are described in chapter 8. These layers were the last samples fabricated in the UHV system by the author. The priorities for the investigations changed. Therefore the M-I barrier project was cancelled to make the system available for the fabrication of high T_c superconductors.

Acknowledgment: I would like to thank Drs J. Kortlandt for the fabrication of the
Nb /Al Al_2O_3 Al/Nb junctions.

Graag wil ik speciaal R.H.M. van de Leur bedanken voor de grote bijdrage die hij geleverd heeft bij het tot stand komen van dit proefschrift.

Alle studenten die een bijdrage geleverd hebben aan dit proefschrift zijn:

P.M.J. Verberne
C.A. van der Jeugd
E.J. van Kersbergen
J.G.W. Wechgelaer
H.M. Appelboom
A.J. van Run
J.A. Kokkedee

REFERENCES

1 T.M. Klapwijk, Proceeding of SQUID 85 editors H.D. Hahlbohm and H.L.Lübbig, Walter de Gruyter Berlin , 1,(1985)

2 G. Hertel, D.J. Bishop, E.G. Spencer, J.M. Rowell, and R.C. Dynes, Phys. Rev. Lett. **50** ,743, (1983)

3 R.C. Dynes and J.P. Garno,Phys. Rev. Lett. **46** ,137, (1981)

4 W.L. McMillan and J. Mochel,Phys. Rev. Lett. **46** ,556, (1981)

5 R.H.M. van de Leur, thesis Technical University Delft, 1988

6 H. Kroger, L.N. Smith, and D.W. Jillie, Appl.Phys.Lett.**39**, 280, (1981)

7 R.J. Pederson and F.L. Vernon, Jr, Appl.Phys.Lett.**10**, 29, (1967)

8 D.W. Palmer and S.K. Decker, Rev Sci Instrum., **44**, 1621, (1973)

9 M. Hatzakis, B Canavello and J.M. Shaw, Proceedings of Microcircuit Enginering 80, editor R.P. Kramer, Delft University Press , 439, (1981)

10 J.M.E. Harper, J.J. Cuomo and H.R. Kaufman, J. Vac Sci. Technol., **21** ,737, (1982) and **21** ,725, (1982)

11 M. Gurvitch, M.A. Washington, H.A. Huggins, and J.M. Rowell, IEEE trans Magn **19** , 791, (1983)

12 J.G. Simmons, J.Appl.Phys, **34**, 1793, (1963)

13 R. Meservey, P.M. Tedrow and J.S. Brooks, J.Appl.Phys, **53**, 1563, (1982)

14 A.S. Barrera and M.R. Beasley, IEEE Trans.Magn. **23**, 866, (1987)

15 J.E. Lewis and R.C. Plumb, J.Chem Soc., **105** , 496, (1958)

16 J.G. Bednorz and K.A. Müller, Z. Phys. B, **64**, 189 (1986)

CHAPTER 2

RATE CONTROL FOR ELECTRON GUN EVAPORATION

A.J.G. Schellingerhout, M.A. Janocko[a], T.M. Klapwijk[b], J.E. Mooij

Department of Applied Physics, Delft University of Technology, Delft,
The Netherlands

[a]Westinghouse R&D Center, Pittsburgh, Pennsylvania, U.S.A.

[b]Department of Applied Physics, University of Groningen, Groningen,
The Netherlands

ABSTRACT

Principles for obtaining high quality rate control for electron gun evaporation are discussed. The design criteria for rate controllers are derived from this analysis. Results are presented which have been obtained with e-guns whose evaporation rate is controlled by a wehnelt electrode or by sweeping of the electron beam. Further improvements of rate stability can be obtained by improved design of e-guns and power supplies.

INTRODUCTION

A stable evaporation rate is crucial for accurate fabrication of advanced alloys and multilayers in molecular beam epitaxy (MBE) systems. Low melting point materials are evaporated from effusion cells in which rate stability is obtained by accurate temperature control. However, high melting point materials must be evaporated with electron gun evaporators. The evaporation rate stability of an electron gun with a constant electrical power is not adequate for demanding MBE applications. Rate stability of an e-gun can be improved by creating a feedback loop. To do this, the evaporation rate is measured with a sensor and compared with a reference value. The sensors commonly used for rate control are quartz crystal monitors, ion gauges, detectors based on electron impact emission spectroscopy (EIES, Sentinel) or mass spectrometers. The sensor generates an electrical signal which is related to the evaporation flux impinging on the sensor. A feedback controller compares this rate signal to a reference value and produces an output signal which is usually used to control the electrical power of the e-gun, and may also control some other operating characteristic of the electron gun, such as beam sweep amplitude which can change the evaporation rate. The problem of feedback applied to an e-gun has hitherto not been addressed in a systematic manner. In this paper a model is presented for the rate control feedback loop. After the discussion of the separate components of the loop, which are the electron gun and the rate sensor, the design criteria for the rate controller are given. Also presented are results of rate stability tests in which optimized feedback controllers were used at a UHV system at Westinghouse [2] with a Temescal SFIH-270-2 electron gun and at Delft with a Balzers ESQ 300U electron gun. In the Temescal gun, beam sweep amplitude adjustment is used as a fast control mechanism to control the evaporation rate [3], while in the Balzers a wehnelt electrode is used [4]. In both cases the rate sensor is a Balzers QMG 511 mass spectrometer. The results show a high degree of noise suppression in the evaporation rate. As shown by experiments further improvement may be expected from improved e-guns and power supplies.

THEORY

A linear model for a rate control feedback system is given in fig.1. The components are described by linear transfer functions, the sensor by $H_2(j\omega)$ and the controller plus source by $H_1(j\omega)$. The reference voltage input is $I(j\omega)$.The evaporation rate (flux) is $O(j\omega)$. All the sources of drift or noise in the evaporation rate are put into the model by a function $N(j\omega)$, which is called the evaporation noise.

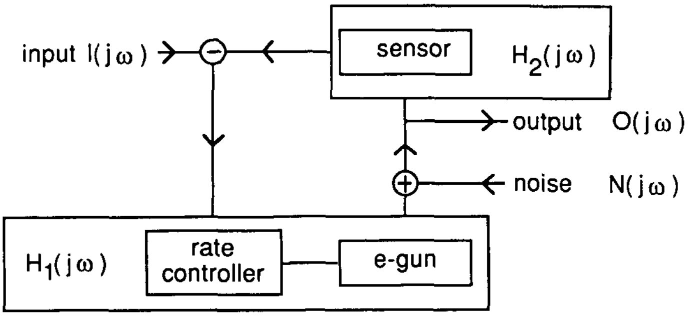

Fig.1 Model for the feedback loop. The evaporation noise $N(j\omega)$ in the evaporation rate $O(j\omega)$ is suppressed by the feedback loop. The sensor, with transfer function $H_2(j\omega)$, measures the rate. The sensor output is compared with a reference input $I(j\omega)$. The rate controller makes the correction signal to the electron gun. The transfer function of the rate controller and the e-gun is $H_1(j\omega)$.

Following conventional analysis of feedback loops [1], the input- output transfer function of the feedback loop is obtained.

$$O(j\omega) = \frac{H_1(j\omega)}{1 + H_2(j\omega)\, H_1(j\omega)} I(j\omega) \qquad (1)$$

The error ratio of the feedback loop is given by R* as defined in

$$O(j\omega) = \frac{1}{1+H_2(j\omega)\, H_1(j\omega)} N(j\omega) = R^*\, N(j\omega) \qquad (2)$$

Feedback is applied to obtain a high degree of noise suppression of the evaporation noise, which implies a low error ratio R*. The factor R* given in eq (2) determines the quality of the rate control. If it would be possible to make the loop gain $H_2(j\omega)\ H_1(j\omega)$ infinite, the result would be a complete suppression of the noise $N(j\omega)$ and eq (1) would simplify to

$$O(j\omega) = \frac{1}{H_2(j\omega)} I(j\omega) \qquad (1a)$$

This results in the inverse transfer function of the sensor, which implies that a constant voltage input $I(j\omega)$ would result in a constant rate. The next step is to make a number of assumptions concerning the transfer functions $H_1(j\omega)$ and $H_2(j\omega)$. They will lead to a simple model of the feedback loop, which is still capable of describing the e-gun rate control problem.

The sensor transfer function $H_2(j\omega)$ is set equal to a constant K_s which implies an infinite bandwidth. The same assumption is made for the transfer function of the electron gun, $H_e(j\omega) = K_e$. The rate controller is modeled with the transfer function $H_R(j\omega) = A \frac{1}{1+j\omega RC}$, with gain A and a time constant RC. We find with $H_1(j\omega) = H_R(j\omega).H_e(j\omega)$ that the evaporation rate is given by:

$$O(j\omega) = \frac{1}{\frac{1}{AK_e} + K_s} \frac{1}{1 + j\omega\frac{RC}{1+AK_eK_s}} I(j\omega) \qquad (3)$$

and

$$O(j\omega) = \frac{1}{1+AK_eK_s} \frac{1 + j\omega\ RC}{1 + j\omega\frac{RC}{1+AK_eK_s}} N(j\omega) \qquad (4)$$

The absolute value of the error ratio given by eq.(4) , is shown in fig.2. No suppression of the evaporation noise $N(j\omega)$ is present at frequencies higher than the bandwidth of the feedback loop, as is usual in feedback systems.

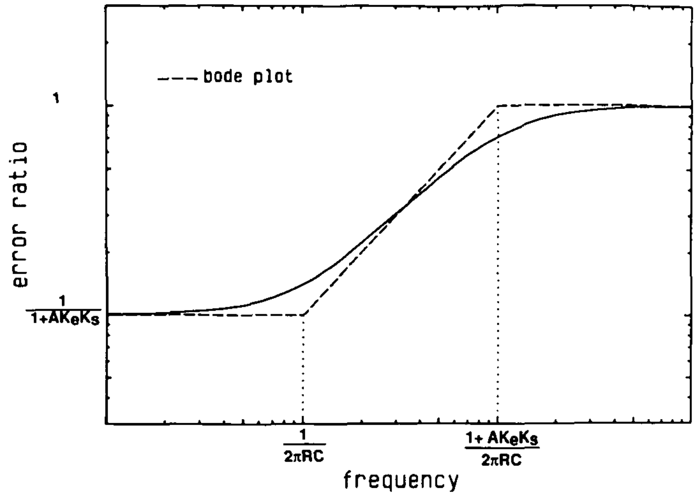

Fig.2 Schematic drawing of the absolute value of the error ratio as a function of the frequency (equation 4).

Before we proceed, a few elementary remarks must be added about ways to characterize the quality of a rate control system. The quality is usually determined by measuring the output voltage of the sensor. This output noise is the product of the evaporation rate noise and error ratio. Only the error ratio is determined by the feedback loop and a decrease in $N(j\omega)$ would also result in a more stable evaporation rate . As will be shown below, in future designs a reduction of $N(j\omega)$ can be achieved by redesigning the power supplies and the e-guns. If the quality of the feedback loop is expressed by the rms value of the output voltage noise, additional information will have to be provided. First, the bandwidth of the measuring device. Second, the evaporated material, since the amount of evaporation noise is strongly material dependent. Third the geometry of the system, meaning the position of the sensor and the substrate relative to the source.

A disadvantage of characterizing the quality by the output voltage noise of the sensor is that a stable sensor voltage does not necessarily mean a stable evaporation rate at the substrate position. A drift or change in the transfer function of the sensor used in the feedback loop is not observable in the output voltage. This applies also for a change in the spatial relation between the rate at the substrate position and at the sensor position (beam profile). The only correct method to analyze the feedback loop to obtain the rate stability $O(j\omega)$ is measuring the rate at the substrate with a method independent of the sensor used in the feedback loop. A method which can be used to determine the fluctuations afterwards is X-ray diffraction on alloys or superlattices.[5]

E-GUNS

In the model for the feedback loop, the transfer function of the e-gun is $H_e(j\omega) = K_e$ which implies a much larger bandwidth than the bandwidth of the feedback loop. This transfer function for the e-gun can be split into two parts. First, there must be a method to have control with a large bandwidth over the electrical power of the electron gun and second, the evaporation rate of the molten material in the e-gun must have a fast response when the power is changed. We start with the response time of the melt. In figure 3, a noise spectrum of the evaporation flux of Nb is shown. No feedback was applied during the measurement of this spectrum. The large noise peaks are at the line frequency of 60 Hz and the higher harmonics.

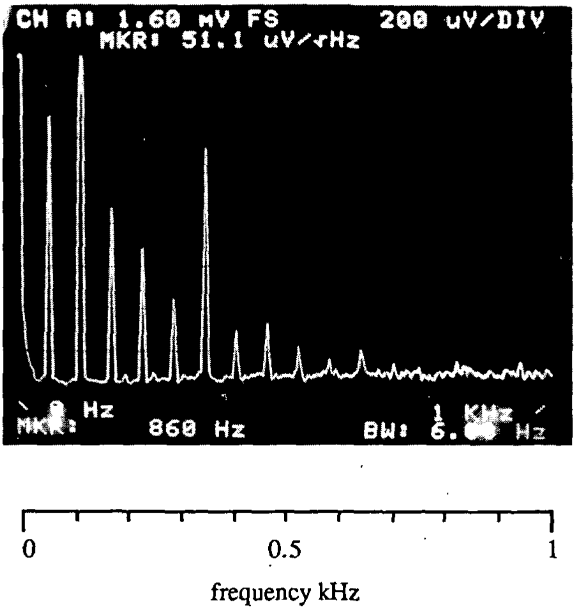

Fig.3 Noise frequency spectrum of the evaporation of Nb. The e-gun was a SFIH-270-2 with a Temescal power supply. The bandwidth of the electrometer of the mass spectrometer was 4kHz during this experiment. The spectrum analyzer was a Hewlett Packard 3582A

This spectrum shows that in this case the major noise components are caused by the power supply, and that the melt does not average these fast power fluctuations. This implies a very fast response time of the melt of Nb up to frequencies as high as 1 kHz. (These fluctuations are most likely caused by the AC current in the filament. The current produces a local magnetic field which results in a sweep of the electron spot on the melt.)

The response of the power output of an electron gun to a change in the control signal for filament current is usually slow. Estimates of the bandwidth are in the order of 0.1 to 1 Hz. To control the fast rate fluctuations a method with high frequency control must be used. This fast control can be obtained by a wehnelt electrode in front of the filament or by changing the sweep amplitude of the electron spot on the melt. The Balzers electron gun ESQ 300U has power control with a wehnelt electrode. The electronics to control the wehnelt voltage at 10kV, which is supplied by the manufacturer, allows for power variations with a bandwidth in the order of 140 Hz. Sweeping the electron spot over the melt is an alternative method to achieve fast rate control and applicable with the Temescal e-guns. A decrease in the rate is observed when the amplitude of the sweep is increased. Contrary to common belief this is not equivalent to an effective defocussing of the spot. As has been shown in fig.3, the response time of the melt is very fast which means that the evaporation flux can easily follow the sweep frequency. The decrease of the rate occurs because the spot dwells longer in a "cold" area. Of course this does not imply that the feedback loop does not operate. A larger sweep amplitude still results in a lower time average rate, so it is possible to stabilize the rate at low frequencies. However, this approach generates strong fluctuations in the evaporation rate at the sweep frequency. A much better solution would be to select a high sweep frequency, in comparison to the response of the melt. This situation will act effectively as a defocussed spot. However, the sweep frequencies presently employed in e-guns are strongly restricted by the sweep coils. The present power supplies for the sweep coils must be modified to allow extension of the sweep frequencies to higher frequencies. Even then the losses in the coils pose a major limitation.

To obtain adequate rate control by sweeping the spot with present e-guns, the sweep frequency must be carefully chosen. The frequency must be larger than the bandwidth of the loop. The fluctuations caused by the sweep are in this situation not detected by the feedback loop. However, even with sweep frequencies larger than the bandwidth problems might occur. Figure 4 shows two spectra of the evaporation of Nb performed with the Temescal gun with two different sweep frequencies (178 Hz, 180 Hz). They are approximately the highest usable frequencies which still have a reasonable sweep amplitude.

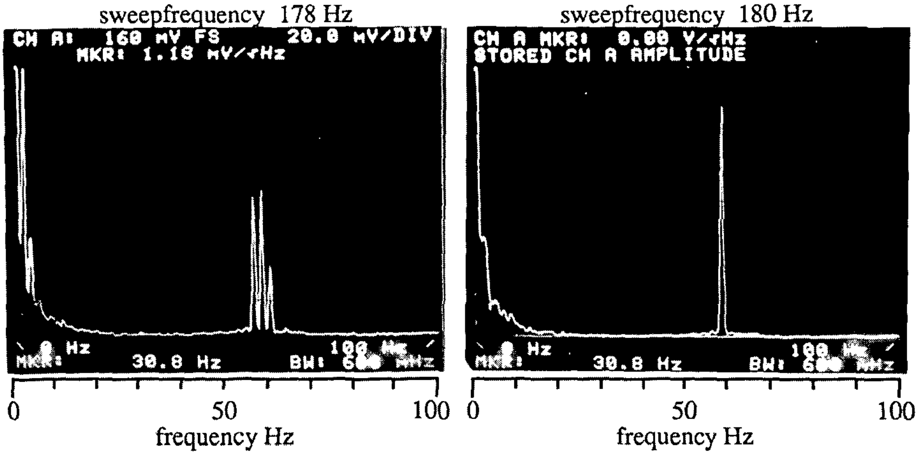

Fig.4 Noise frequency spectrum of the Nb evaporation rate with two different sweep frequencies. (178 and 180 Hz)

As can be noticed in fig.4b, the low frequency instability of the melt is increased when the sweep frequency is close to the line frequency. This is caused by the strong non linearity of the melt. In this case the best solution, without modifying the e-gun or power supply, is to lock the sweep frequency to 60 Hz or a higher harmonic of the line frequency. The wave form of the sweep current applied to the coils is at present not important because of the strong damping at high frequencies.

SENSORS

The evaporation rates are commonly measured with one of the following sensors: mass spectrometers [6], ion gauges [3], detectors based on electron impact emission spectroscopy (ESIS, sentinel) [7] and quartz crystal micro balances. Apart from the quartz crystals, all sensors measure the local density of evaporating atoms. The rate signal is obtained by multiplying with the average speed of the atoms, which is linear with $\sqrt{T}$. (T is temperature.) This results in an output signal which is not linear with the evaporation rate. This small correction, however, is usually neglected. All three sensors have the advantage of a long life time in vacuum, in contrast to quartz crystals which have to be replaced after being loaded with material. The quartz crystal sensor is often used as a calibration for the other three sensors.

Most sensors operate in a mode in which the output voltage is updated with a frequency f_s.

This updating of the output is equivalent to sampling the evaporation rate. The sampling procedure is error free when the bandwidth of the noise in the evaporation rate is smaller than the sampling bandwidth $\frac{f_s}{2}$. [8] As the evaporation noise spectrum is very broad, filtering before sampling is needed. Often an integration between the two sampling points is used which results in an attenuation of the higher frequencies beyond the sampling bandwidth. If the filtering is not sufficiently effective, the result will be extra low frequency noise caused by high frequency noise mixed down by the sampling process. Another problem associated with the sampling action of the sensor is that it leads to a strong limitation in the attainable noise suppression. The sampling causes a fundamental restriction in bandwidth which is connected with eq.(4), to the error ratio. So the noise suppression is limited by the sampling frequency. This means that the low sampling frequencies usually employed in sensors result in a limited attainable noise suppression.

The sensitivity of the sensor, which is the minimum detectable evaporation rate per unit time, is an important parameter in comparing different sensors. The sensitivity is the limit to which the evaporation noise can be suppressed by the feedback loop. Low pass filtering after the sensor in the feedback loop must be avoided. When filtering of the sensor output signal is needed, the filter should be placed outside the loop. If a higher resolution in evaporation rate is obtained by a decrease in update frequency f_s the noise suppression will decrease as well, because of the reduction in bandwidth. The sensitivity limits the minimum evaporation noise that can be detected. It is caused by other noise sources like shot noise in the signal, amplifier noise or environmental noise caused by ground loops or vibrations. The feedback loop does not discriminate between evaporation noise and all other noise sources which are in the sensor output. In the case of ideal feedback (eq 1a) all noise sources are suppressed and are no longer observable in the output signal. When this occurs the rate is following the other noise sources (with negative sign) and therefore the sensitivity is the minimum evaporation noise which can be successfully suppressed.

Other important aspects of rate sensors are the stability on the time scale of an evaporation run and the stability on a longer time scale. This long term stability can be by passed by frequent calibrations to a quartz crystal. The stability on the time scale of a evaporation run is crucial. As is already discussed, the stability of the output signal of the sensor in the feedback loop is not a good measure of the sensor stability.

MASS SPECTROMETER

The mass spectrometer as a rate sensor in a feedback loop has the advantage of a large sensitivity and a large bandwidth. The Balzers QMG 511, used as sensor in our experimental rate controllers, has the extreme sensitivity of 0.1 pm/s (bandwidth 1Hz) for Nb. The sensor to source distance is 76 cm. The distance of the substrate to the source is 60 cm. The mass spectrometer is equipped with an electrometer as a current amplifier. Based on the obtained sensitivity there is no need for an electron multiplier. The bandwidth of the electrometer is 240 Hz.

The main problem associated with a mass spectrometer as a rate sensor is the stability, because of the complexity of the instrument. Experiments with SiGe superlattices showed that the stability of the sensor during an evaporation run was smaller than 3% .[5] We tested the long term stability by calibration of the mass spectrometer with an ion gauge during a period of 14 days. The differences were always below 5 %. It was essential in these long term stability measurements to monitor the grid voltages of the mass spectrometer, to check whether they have changed.

A mass spectrometer is, like ion gauge sensors, sensitive to secondary electrons emitted by the electron gun. The sensitivity to this interference is much less when compared with the ion gauges, because of the ion extraction voltages used for the quadrupole analyzer and the geometrical shielding of the instrument. The occurrence of the secondary electrons is very easily observed when the mass spectrometer is set at a mass number where no ions are present. If the electrons are detected they will cause a negative current.

If the mass spectrometer is multiplexed between mass numbers, it will be possible to monitor two or more evaporating sources. The multiplexing is sampling of the evaporation rate and results in an additional limitation of the bandwidth. The multiplex frequency must be chosen as high as possible for the mass spectrometer. Limitations are the bandwidth of the electrometer and the stabilization time of the mass spectrometer at the new mass number. Both effects result in lost measuring time for monitoring the rate, which result in a decrease of sensitivity. Another problem is the reduced suppression of frequencies above sampling frequency. The flux is only measured a limited time which makes the filtering before the sampling less effective. In choosing the multiplex frequency, care must be taken to avoid interference with the line frequency (sweep frequency).

We tested the mass spectrometer in the multiplex mode by monitoring singly and doubly ionized tantalum ions(Ta^+ and Ta^{2+}). The Ta^+ signal output was used as the rate signal for the feedback loop. The results are shown in fig.5. The linearity between the two outputs shows that the multiplexing of the mass spectrometer also results in correct rate signals.

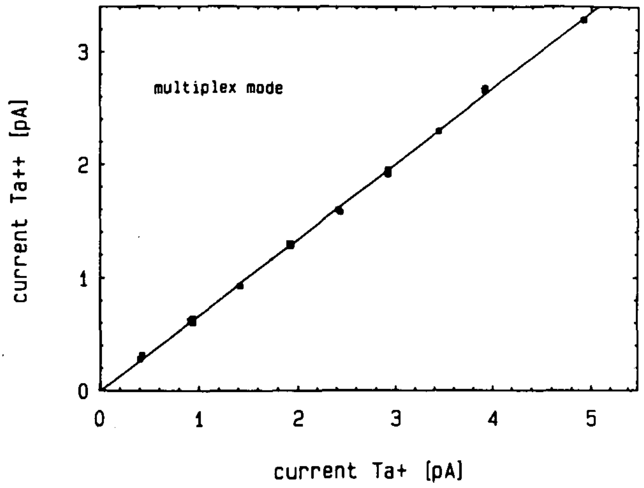

Fig.5 Output of the two channels of the mass spectrometer when it is multiplexing between Ta^+ and Ta^{2+} (mass number 181 and 90.5). The Ta^+ signal is used as rate signal for the feedback loop

RATE CONTROLLER

The rate controller is designed as an interface between the sensor and the electron gun. It can of course never improve on the limitation posed by the sensor. These limitations are the sensitivity and the bandwidth when this is caused by a sampling process. The quality of the electronic components in the rate controller will be considered ideal in the context of the feedback loop model.

The controller must limit the bandwidth of the feedback loop to the maximum permissible by the sensor. The controller with the transfer function $\frac{A}{1 + j\omega RC}$ has this property (eq 3). If the RC time is chosen comparable to the time scale of an evaporation run, a large low frequency noise suppression will be obtained which will result in an excellent DC stability of the rate. The obtained transfer function is of an integrating controller. The adjustment is very straightforward, involving only the gain A until sufficient noise suppression is obtained. Non linearities occurring in the transfer function K_e of the e-gun will result in small changes in gain which only results in changes in bandwidth. The commonly used PID controllers in these feedback loops are useless because of two reasons. First, since the bandwidth of the loop is already restricted by the sampling of the sensor, it is not possible to expand the bandwidth by a PID controller. Second, there are no time constants in the loop which must be compensated by the controller. When the electron gun is only equipped with a filament control, the assumption of the transfer function K_e with a large bandwidth is no longer valid and a more complex controller can be useful. But since the transfer function of the filament behaves as a higher order system only limited improvements can be achieved. Proportional gain can be implemented in the controller for the eventuality of materials with a time constant in the bandwidth of the feedback loop, but it should always be used with caution.

The controller must produce the low frequency control signal for the filament and the high frequency signal for the sweep amplitude or the wehnelt grid voltage. The schematic of this part of the feedback loop is drawn in fig 6. The subtraction of the output signal of the low pass filter with frequency f_c from the rate control signal, results in a high pass filter with the same frequency. This crossover filter in the rate controller results in an average constant spot size or an average constant wehnelt setting. The crossover frequency f_c of the filter can best be chosen well below the bandwidth of the filament. The result is an electronically determined crossover frequency which is very stable.

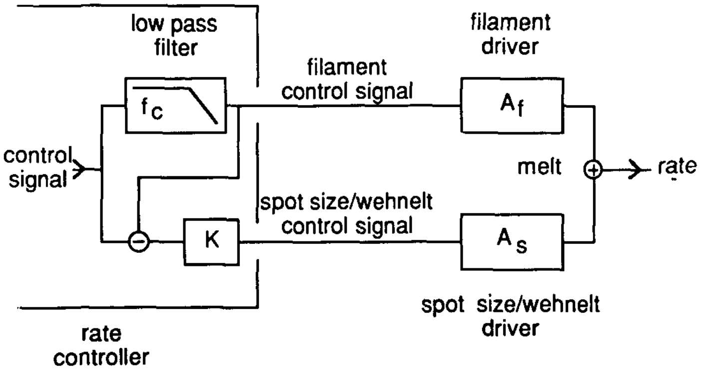

Fig.6 Linear model for the generation of the high and low frequency control signals.

The transfer function of fig 6 is

$$H_{vr} = \frac{A_f \left(1 + K \frac{A_s}{A_f} j\omega \frac{1}{2\,\pi\, f_c}\right)}{1 + j\omega \frac{1}{2\,\pi\, f_c}} \qquad (5)$$

In eq.(5) the transfer function of the filament control signal for a rate change is A_f. The spot size or wehnelt transfer function is A_s. Both rate changes are superposed in the melt. The crossover frequency between the filament and the spot size / wehnelt is only equal to the electronic crossover frequency f_c in the rate controller when the gain factor K is adjusted to the relation $K = \frac{A_f}{A_s}$.

The model used for the filament-sweep or filament wehnelt combination is linear. But the combination has more similarities with a multiplier, since the wehnelt and the sweep modulate the power of the filament. The only practical implication for the rate controller is the obvious one of having the crossover frequency f_c well inside the bandwidth of the loop. Higher order multiplication terms will now be suppressed in the loop.

The rate controller must be equipped with a number of protections in case mal functions occur. With a fast feedback loop the operator is always too late to respond. Protections which are necessary are minimum and maximum power limiters and indicators for saturation of control signals.

Results obtained with an I-controller are shown in fig 7. The e-gun is a Temescal SFIH-270-2. The figure shows the output of a chart recorder (bandwidth ≈ 6Hz) while Nb is evaporated with different settings of the gain A. As is observed in the figure, the noise suppression is increased when the gain A of the rate controller is increased.

The controller can be extended with a feed forward filter to improve the stability for rate changes. These rate changes occur if one would like to fabricate compositional modulated superlattices or artificial barriers in superconducting junctions .[5,9] The reference voltage I(jω) must be adjusted to obtain the desired change in rate. Since these rate variation are deterministic and not a noise source, a control signal through an appropriate filter can be applied to the filament. The result is an improved stability for fast rate changes.

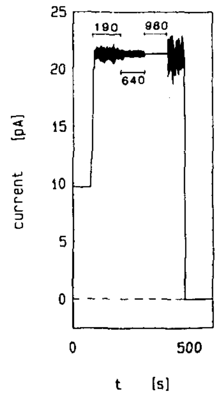

Fig.7 Results obtained for the rate control of Nb by sweeping of the electron spot(SFIH-270-2). The output of a chart recorder (bandwidth ≈ 6Hz) is displayed with different setting of rate controller gain A (arbitrary units). The evaporation noise suppression increases when the bandwidth of the feedback loop is increased by a higher gain setting. The mass spectrometer is used in the single channel mode. The sweep frequency is 120Hz.

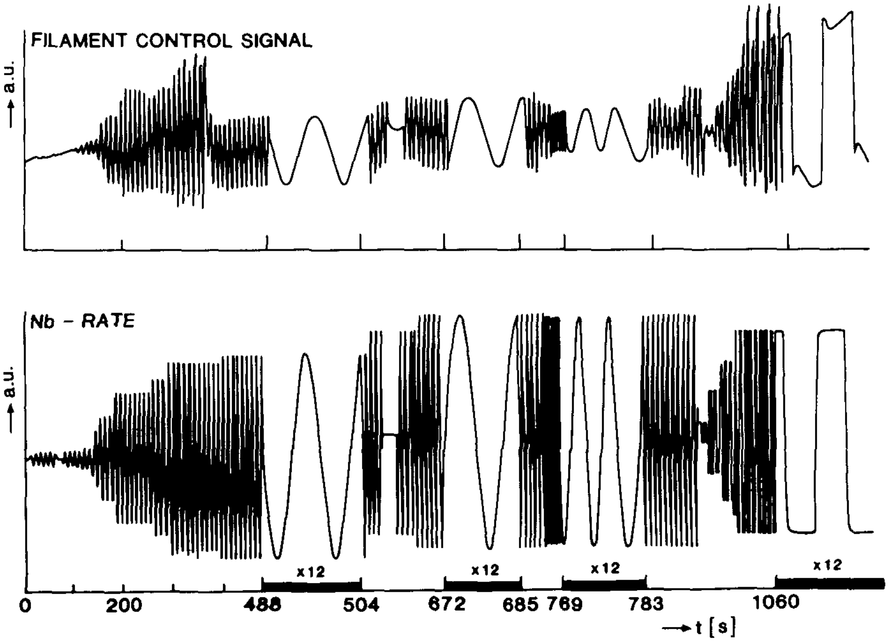

Fig.8a Results obtained for the rate control of Nb with a wehnelt controlled e-gun. The output of the mass spectrometer as well as the control signal to the filament are displayed. The reference input signal I(jω) is a function generator which is set at different waveforms and amplitudes. The time scale is in some parts of the figure enlarged with a factor 12. The lower trace is the Nb rate (the average rate is 0.27 nm/s.). The mass spectrometer is in the single channel mode. The upper trace is the control signal to the filament. The feed forward filter causes the fast response of the control signal to the filament.

Results obtained with a feed forward filter added to an I-controller are shown in fig.8. The e-gun was wehnelt controlled. The control signal of the filament is shown in fig.8a. The extra signal of the feed forward filter is clearly visible. The same feedback system has been used for the materials Nb, V, Ta, Fe, Si, Sn, Ge, Cu, Y and Al. With all materials similar results have been obtained.

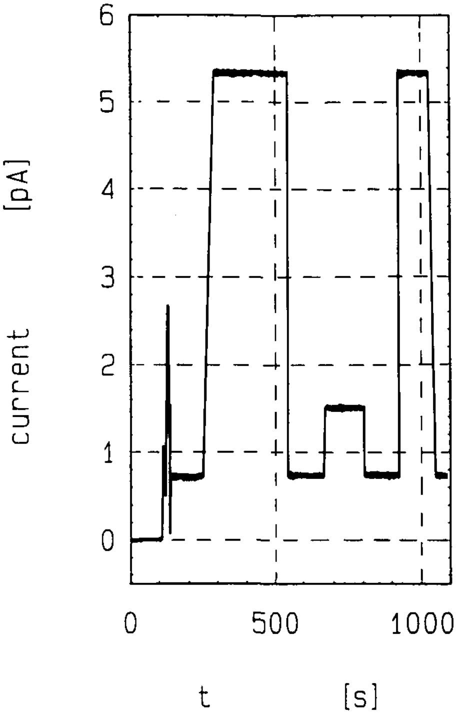

Fig.8b Results obtained for the rate control of aluminium with a wehnelt controlled e-gun during the fabrication of an artificial barrier. The mass spectrometer was multiplexing between oxygen (measured at mass number 16) and aluminium (mass number 27). Both mass numbers were measured 8 ms which results in a maximum bandwidth of 31 Hz. The noise of the electrometer is just visible. It has a rms value of about 4 fA (bandwidth ≈ 6Hz). The maximum evaporation rate of Al is 0.23 nm/s (5.33 pA), the minimum evaporation rate is 22 pm/s (0.72 pA).

BEAM PROFILE

The I-controllers have a large DC stability which is observed in the output voltage of the rate sensor. The feedback loops have been used to make alloys and superlattices. The deposition time of these structures varies from 20 to 60 minutes. They were analyzed by X-ray diffraction techniques. Occasionally observations were made of an additional broadening of the X-ray peaks. This was caused by a drift in deposition rate, while according to the sensor output no changes in deposition rate had occurred. This drift can be caused by the mass spectrometer or by the beam profile. These two effects are difficult to separate in a given experimental configuration, but we believe the major drift is caused by the beam profile and not by the mass spectrometer. The large influence of the beam profile is demonstrated with the following experiment. We calibrated the mass spectrometer versus a quartz crystal. The output of the mass spectrometer was used as a rate signal for the feedback loop during this calibration. We used the e-gun with the sweeping spot. In this loop the average spot size is an extra parameter which can be instantaneously changed. The results are displayed in fig.9. It shows a strong increase in deposition rate observed at the quartz crystal when the average sweep amplitude decreases. The apparent change in the beam profile, results in a different calibration factor between mass spectrometer and quartz crystal. At high rates the difference is about 30 %. The calibration factor has a direct relation with the spot size. If the spot size is changed to the original value, then the original calibration factor will be obtained again. This excludes any influence of the sensitivity of the mass spectrometer.

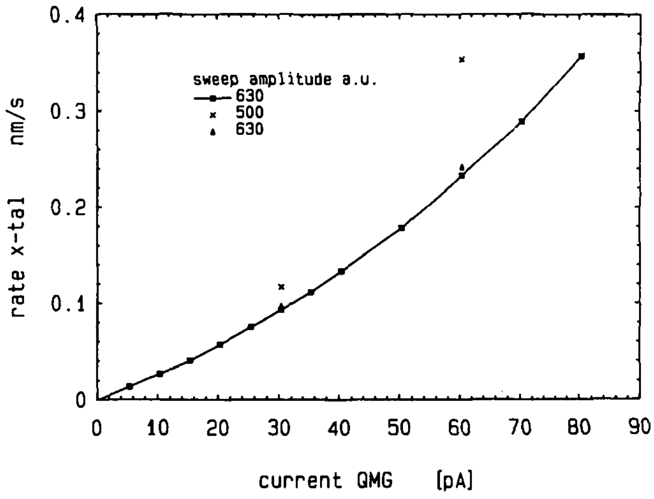

Fig.9 Calibration of the mass spectrometer versus a quartz crystal with different values of the average sweep amplitude (arbitrary units). The squares are the initial calibration points. The crosses are the new calibration points after a decrease in the average sweep amplitude. The triangles show the calibration points when the average sweep amplitude is returned to its original value.

To improve the stability of the rate we equipped a wehnelt controlled e-gun with high frequency sweeping coils (≈ 1kHz) which resulted in an improved stability. We believe this is not only caused by a decrease in the geometrical changes in the melt during the evaporation. The partial pressure of the evaporated flux above the melt is also reduced, and this high pressure is a source of instability for the spatial distribution of the evaporated flux.

The results obtained with the rate controllers show a large suppression of evaporation noise. This implies a fast response of the melt to a change in power, and leads to easily adjustable rate controllers for the feedback of the e-guns. Further improvements in rate stability can be obtained by stable sensors and particular new e-gun and power supply design. The e-guns and power supplies must be redesigned for stable rates in a MBE environment, where high rates and high efficiency are not of prime interest. New demands for the power supply are a DC filament and a very low ripple high voltage supply, with a low output impedance for the fast power fluctuations caused by the rate control. The result will be a reduced evaporation noise generated by the melt. For the e-gun it is desirable to have an adjustable spot size for a better control of the beam profile. The spot does not have to be tightly focussed. If the defocussing is obtained by sweeping of the spot, the sweep frequency must be higher than the response time of the melt. In this case the spot is effectively defocussed for the evaporation which leads to a reduction of the partial pressure above the melt and no extra noise generation by the sweep. The spot size can be easily adjusted in this concept of sweeping at high frequencies.

CONCLUSIONS

To summarize, results obtained by feedback applied to many materials show the possibility of accurate rate control of e-guns. Limits are imposed by the sensitivity and the bandwidth of the sensor.

The large bandwidth of the melt allows the use of an integrating controller. This type of controller is very easy to use and easy to adjust for different materials.

A mass spectrometer is useful as a sensor for rate control. The main advantages are the high sensitivity and the large bandwidth. This results in a feedback loop in a high degree of noise suppression.

Further improvements in rate stability can be obtained by improved design of e-gun and power supply. The objective is a more stable beam profile and less evaporation noise.

Acknowledgements This work is supported by the Foundation for Fundamental Research on Matter (F.O.M.).

REFERENCES

1 K. Ogata, Modern Control Engineering (Prentice-Hall, Inc.,Englewood Cliffs, N.J.,1970)

2 J. Talvacchio, M.A. Janocko, J. R. Gavaler and A.I. Braginski, Advances in Cryogenic Engineering volume 32 (R.P. Reed and A.F. Clark editors),(Plenum Press, N.Y., 1986), pp 527

3 R.H. Hammond, IEEE Trans. Magn. **MAG-11**,201 (1975)

4 W.K. Huber, U. Wegmann, K. Wellerdieck and C.A. Gorter, Proceedings 8th international vacuum congress Cannes, Sept, (1980)

5 R.H.M. van de Leur, A.J.G. Schellingerhout, J.E. Mooij and F. Tuinstra , Appl.Phys.Lett.**52**, 1005, (1988)

6 H.Lutz, J. Vac.Sci. Technol.**15** , 309 (1978)

7 C.A. Gogol and S.H. Reagan, J.Vac.Sci.Technol. A **1**, 252 (1983)

8 S.A. Tretter, Discrete-time signal processing (John Wiley&Sons New York, 1976)

9 A.J.G. Schellingerhout, H.M. Appelboom, J.A. Kokkedee, J. E. Mooij and T.M. Klapwijk, in Anderson Localization, edited by T. Ando and H. Fukuyama (Springer-Verlag Berlin Heidelberg 1988), pp 74

CHAPTER 3

MASS SPECTROMETER CONTROLLED FABRICATION OF SI/GE SUPERLATTICES

R.H.M.van de Leur, A.J.G.Schellingerhout, J.E.Mooij and F.Tuinstra
Department of Applied Physics,Delft University of Technology,
Delft, The Netherlands

We have used a quadrupole mass spectrometer to control deposition rates during fabrication of compositionally modulated Si/Ge superlattices. Its performance has been evaluated by an X-ray diffraction study of a superlattice. The variation of the Si deposition rate was less than 3% during the whole deposition time of 30 minutes. This proves that a mass spectrometer can be succesfully employed as rate monitor in Si molecular-beam-epitaxy systems.

A strong and increasing interest exists at present in strained $Si_{1-x}Ge_x$ alloys and multilayer thin films.[1,2,3] For accurate fabrication, precise control of the deposition rates of Si and Ge is essential. As sensors for rate control quartz crystal monitors, iongauges[4], detectors based on electron impact emission spectroscopy (EIES,Sentinel)[5] or mass spectrometers[6] are used. We employ a quadrupole mass spectrometer (Balzers QMG 511,cross beam) in a time-multiplexed mode to control the deposition rates at a sample frequency of 62 Hz. We have evaluated the performance of the mass spectrometer rate sensor by means of a detailed X-ray diffraction study of a Si/Ge superlattice.This evaluation method allows us to detect deviations between actual deposition rate and rate sensor output where the latter is kept constant by the rate control feedback loop. The Si/Ge superlattice that was studied is compositionally modulated as shown in figure 1. The Ge concentration varies periodically between 5 and 22%. Fluctuations in the deposition rates and consequent nonperiodic concentration variations of concentration result in broadening of X-ray diffraction peaks. The width of the observed diffraction peaks sets an upper limit to the error of our rate monitor.

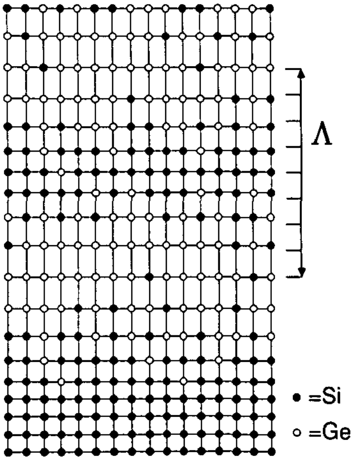

Fig.1 Schematic representation of a strained, compositionally modulated Si/Ge superlattice with modulation period Λ, on the Si substrate. (For clarity, the Ge concentration is chosen to vary around 50% and the displacement and substitution modulation are exaggerated)

Our ultra-high-vacuum system has a turbo molecular pump, a titanium sublimation pump, and several liquid nitrogen shrouds to reach a base pressure in the upper 10^{-9} Pa domain. Two electron beam evaporators provide the possibility of simultaneous evaporation of two materials. The evaporation rate is controlled via the filament current and the Wehnelt shield of the electron beam evaporator. A diagram of the whole feedback loop is shown in figure 2. The rate controller and the demultiplexer are home-built.

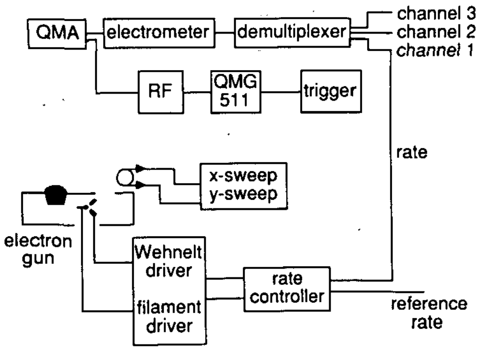

Fig.2 Feedback loop of the deposition rate control. QMA : ionization chamber and mass selection; RF : radio frequency generator; QMG511: mass spectrometer; electron gun : electron beam evaporator;.

We fabricated the compositionally modulated Si/Ge superlattice under consideration, by modulating the average Ge deposition rate of 0.02 nm/s sinusoidally, while the Si rate was kept constant at 0.15 nm/s. The Si(001) substrate, on which the superlattice was grown, was cleaned using Henderson's procedure[7] and heated for a short time in situ at 1150 °C. During deposition of the superlattice the substrate was held at a temperature of 550 °C while the pressure rose to 5×10^{-7} Pa. The frequency of the sinusoidal reference signal and its amplitude were chosen such as to get a modulation period of 3.4 nm and a Ge concentration varying between 5 and 22 %. The lattice parameters of the 350 nm thick superlattice were obtained by X-ray diffraction, using a powder diffractometer. The orientation of the tetragonally distorted superlattice with respect to the Si substrate is $(001)_{sl}$ // $(001)_{sub}$ and $[100]_{sl}$ // $[100]_{sub}$. This orientation, determined by X-ray photographs, implies coherent epitaxial growth. The lattice constants are 0.5488(2) nm in the direction of modulation and 0.5431(2) nm parallel to the substrate. This implies that the superlattice is accommodated to the Si substrate, which is in agreement with the results of People and Bean[8] for $Si_{1-x}Ge_x$ alloys. The modulation period was determined by the 105 periods of the reference signal counted during deposition and the sample thickness of 350 nm measured afterwards. The result is in excellent agreement with the period of 3.40 nm obtained by X-ray diffraction. X-ray diffraction was also used to measure the average composition of the superlattice. With the ratio $2C_{12}/C_{11}$ of the stiffness constants equal to 0.76,[9] and the lattice parameters as mentioned before, the average Ge concentration was calculated to be 0.141. This result is in good agreement with a concentration of 0.145 determined from the thicknesses of the superlattice and a simultaneously deposited layer of pure Si.

A specific problem which arises when a mass spectrometer is used to control the deposition rate of Si is the coincidence of its mass number and that of background gases such as N_2 and the usually more troublesome CO. One method to cope with this problem is to use a mechanical chopper, as has been reported in combination with ion gauge sensors[3], to distinguish the Si from the background gases with mass number 28. A mass spectrometer provides more elegant ways to solve this problem. Instead of controlling the silicon deposition rate with Si^{28}, one can use one of the isotopes Si^{29} or Si^{30} with natural abundances of 4.7 and 3.1%.[10] When Si^{30} is used for rate control, the influence of CO ($C^{12}O^{18}$) is decreased by a factor of about 0.07 and N_2 ($N^{15}N^{15}$) can be neglected completely.[10] Besides Si atoms, the evaporation flux of silicon also contains Si_2 and Si_3 molecules. To determine whether Si deposition control is possible with Si_2 we measured the Si_2 flux versus the Si flux with the mass spectrometer in the time-multiplexed mode. We observed a linear relation between these two fluxes, which shows that Si rate control with Si_2 molecules is possible. Which option for Si rate control has to be used depends on the specific molecular-beam-epitaxy (MBE) apparatus. Whether rate control with Si^{28} is possible depends on the background pressure of gases with mass number 28 and the spatial orientation of sensor and source, because this determines the ratio of background gases and evaporation flux. In our system rate control with Si^{28} is excluded. We prefer to use the Si_2 flux for rate control, although the output signal of the sensor is reduced by a factor 0.04 compared to Si^{28}. When one of the isotopes Si^{29} or Si^{30} would have been used, the reduction would have been larger due to the necessity to increase the resolution of the mass spectrometer to separate the isotope peaks. The output rms voltage noise (band width 1 Hz) when using Si_2 is equivalent to a deposition rate noise of 1.2 pm/s. At a Si deposition rate of 0.15 nm/s this provides a signal to noise ratio which is high enough to obtain rate control. The problem of background gases does not occur for Ge which is controlled on the isotope Ge^{74}.

The stability of the deposition rates on the substrates is determined by the quality of the feedback loop, the rate sensor and the relation between the deposition fluxes at the sensor and the substrates. X-ray diffraction of Si/Ge superlattices provides us with a nice tool to investigate the stability of the deposition rates on the substrates. Superlattices provide the possibility to distinguish the variation in the ratio of the deposition rates of the constituents from the variation in the total rate. This allows us to evaluate the long term (30 minutes) stability of the sensor. We first discuss the effect of a variation in the ratio of both rates, leading to a concentration variation. This effect is similar for superlattices as for alloys. The lattice constant of a $Si_{1-x}Ge_x$ alloy varies linearly with the Ge concentration and is given by a = (0.5431 + 0.0226·x) nm.[11] This implies that a 1 % variation of the Ge concentration in a $Si_{0.86}Ge_{0.14}$ alloy would result in a lattice constant variation of 0.041 %. Among other factors, such as the thickness of the layer, the width of the diffraction peaks is determined by continuous but nonperiodic variations in the lattice constant. Consequently, the widths of the diffraction peaks in $Si_{1-x}Ge_x$ alloys can be related to a variation in concentration. A 1 % variation of the Ge concentration in a $Si_{0.86}Ge_{0.14}$ alloy would lead to a broadening of 58" in the diffraction angle θ when Cukα radiation is used. Information about the stability of the total deposition rate can be obtained from superlattices. Instability of the total rate leads to a variation in the modulation period and consequently to a broadening of the satellite reflections[12,13],which increases with their order. The widths of the small angle superlattice peaks (000m) is proportional to a variation in the modulation period because these widths are hardly affected by lattice defects such as dislocations. Broadening of main reflections of the average lattice is accompanied by a broadening of the satellites belonging to these reflections, even in the absence of a variation in the modulation period. This implies that only the additional broadening with respect to the main reflection provides information about the variation in the modulation period.

In our Si/Ge superlattices a variation in concentration due to a variation in the ratio of the deposition rates of the constituents broadens the main peaks. It is very important to realize that even in the absence of any dislocations, these peaks are broadened due to a concentration variation. Figure 3 shows the rocking curve of the (004) main reflection of the superlattice. The high resolution is obtained with a Si(110) four-crystal monochromator of the type described by Bartels.[14] Due to this high resolution, additional structure can be observed within the 120" wide peak. This peak width implies that the lattice constant perpendicular to the substrate varies by 0.086%. When the accomodation to the substrate is taken into account, using the stiffness constants mentioned before, this variation in lattice constant implies a nonperiodic variation of the average Ge concentration x between 12.7 and 15.5%. Attributing all the broadening to a variation in the Si deposition rate sets an upper limit of 3% to the variation in the relative Si rate. The additional structure in the diffraction peak indicates that this particular sample consists of two parts with a difference in average lattice constant perpendicular to the substrate. This suggests more a jump in the deposition rate than a gradual change. A sample thickness of 300 nm would cause a peak width of about 68". In order to evaluate the stability of the total deposition rate, the width of the satellite reflections (0001) and

$(004\bar{1})$ was determined. Because of their low intensity these satellite reflections were measured on a powder diffractometer. No broadening beyond the instrumental broadening was observed, which shows that the variation in the modulation period is less than 3%. This proves that the absolute Si depostion rate varied less than 3% during the 30 minutes of deposition.

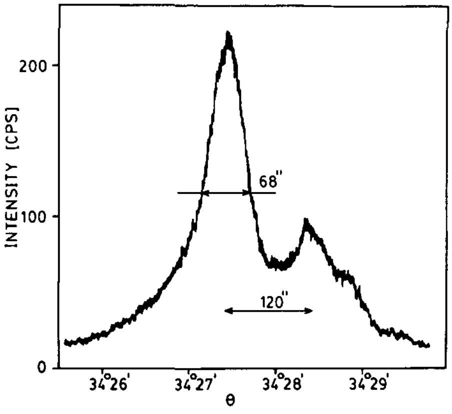

Fig.3 Rocking curve of the (004) main reflection of the compositionally modulated Si/Ge superlattice.

In conclusion, we have shown that a mass spectrometer is a suitable rate sensor in a Si MBE type of system. Even if all diffraction peak broadening is attributed to variations in the Si deposition rate and even if all these rate variation are attributed to the sensor errors, the stability of the mass spectrometer is found to be better than 3%. The problem caused by background gases of mass number 28 can be circumvented succesfully. In addition, we have shown that X-ray diffraction of superlattices provides a good method to evaluate the performance of the deposition rate control.

Acknowledgment. This work is supported by the Foundation for Fundamental Research on Matter (F.O.M.).

REFERENCES

1. J.C.Bean, J.Vac.Sci.Technol.B, 4, 1427 (1986)
2. S.Froyen, D.M.Wood and A.Zunger, Phys.Rev.B 36, 4547 (1987)
3. G.Abstreiter, H.Brugger, T.Wolf, H.Jorke and H.J.Herzog, Phys.Rev.Lett. 54, 2441 (1985)
4. R.H.Hammond, IEEE Trans.Magn. MAG-11, 201 (1975)
5. C.A.Gogol and S.H.Reagan, J.Vac.Sci.Technol. A, 1, 252 (1983)
6. H.Lutz, J.Vac.Sci. Technol. 15, 309 (1978)
7. R.C.Henderson, J.Electrochem.Soc. 119, 772 (1972)
8. R.People and J.C.Bean, Appl.Phys.Lett. 49, 229 (1986)
9. American Institute of Physics Handbook, edited by D.E.Gray (McGraw-Hill, New York, 1972)
10. Handbook of Chemistry and Physics, edited by R.C.Weast (CRC Press, Boca Raton, 1985)
11. H.Stöhr and W.Klemm, Z.anorg.Chem. 241, 314 (1939)
12. A.Segmüller and A.E.Blakeslee, J.Appl.Cryst. 6, 19 (1973)
13. W.J.Bartels, J.Hornstra and D.J.W.Lobeek, Acta Cryst. A42, 539 (1986)
14. W.J.Bartels, J.Vac.Sci. Technol. B 1, 338 (1983)

CHAPTER 4

CRITICAL THICKNESS FOR PSEUDOMORPHIC GROWTH OF SI/GE ALLOYS AND SUPERLATTICES

R.H.M.van de Leur, A.J.G.Schellingerhout, F.Tuinstra and J.E.Mooij

Department of Applied Physics, Delft University of Technology
Delft, The Netherlands

ABSTRACT

A model, based on energy considerations, to determine the critical thickness for pseudomorphic growth of Si/Ge alloys and superlattices is introduced. Comparison with experiments shows a good agreement between the theory and experiment. It is also shown that in films which are initially dislocation-free, the energy barrier for the nucleation of dislocation loops can be crossed by thermal activation if the film is thicker than the critical value provided by the model.

INTRODUCTION

Thin films of $Si_{1-x}Ge_x$ alloys can be grown pseudomorphically i.e.without dislocations on a Si-substrate to a certain thickness. This critical thickness decreases with the Ge concentration x or, equivalently, with increasing difference in the stress-free lattice constants (misfit) of alloy and substrate. Above the critical thickness dislocations are generated. As has been predicted[1] and observed[2,3], these misfit dislocations are situated at the interface between film and substrate and the misfit between the film and the substrate is distributed over misfit dislocations and strain in the film. In this paper we introduce a model, based on energy considerations, describing the relation between thickness and strain in the film. Existing theories of Van der Merwe[1,4] and Matthews[5,6] predict critical thicknesses which, for the case of small misfits in semiconductors, are a factor 5 to 10 smaller than those observed. Our model predicts the critical thickness more exactly. Because this model is based on energy considerations, it provides the thermodynamically stable state and the film has to be kept long enough at an elevated temperature to reach this state by thermal activation. At a sufficient high growth temperature this thermodynamically stable situation is reached during growth. We discuss in this paper the growth of Si/Ge alloys and superlattices on (001) oriented Si substrates. Our model, however, can easily be extented to other epitaxial, lattice mismatched, systems. The only necessary information for our model is the type of dislocation that is formed and the related glide system. The dislocation lines in $Si_{1-x}Ge_x$ alloys are parallel to the <110> directions in the (001) plane and the Burgers vectors lie in the {111} glide planes.[7,8] This implies that the Burgers vector is inclined at 45° to the (001) interface between film and substrate and at 60° to the dislocation line (see figure 1).

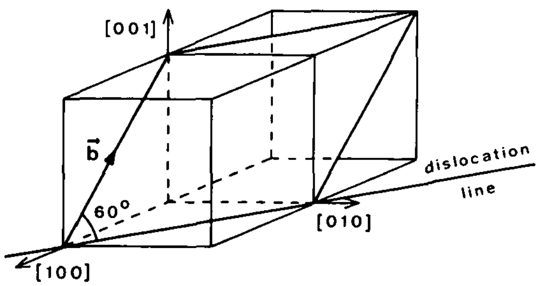

Fig.1 The 60° mixed type dislocation with the Burgers vector in the (111) plane inclined at 45° to the interface.

Theories concerning dislocations are based on the concept of elastically isotropic crystals. The anisotropy ratio $2c_{44}/(c_{11}-c_{12})$ of Si and Ge, however, is about 1.6.[9] This indicates that the isotropy approximation is rather crude. To use the methods based on isotropic crystals it is necessary to have a good approximation for isotropic constants such as the Poisson ratio and the shear modulus in terms of the well known anisotropic constants. The elastic energy in the film, due to the substrate induced strain, has to be calculated using the stiffness constants c_{11} and c_{12} related to the principal axes of the cubic crystal because the (001) planes of the film and the substrate are parallel. Because of this highly anisotropic strain we prefer to use for the Poisson ratio and the shear modulus the expressions $\nu = c_{12}/(c_{11} + c_{12})$ and $G = (c_{11}-c_{12})/2$ which are the elastic constants related to the principal axes of the film. The numerical values used, are the average of those of Si and Ge and deviations from Hooke's law are neglected. Further it is assumed that the substrate-induced strain is constant throughout the whole film.i.e. that the curvature of film and substrate due to the stress is neglected. It has been shown[10] that finite lateral dimensions of the epitaxial system reduce the strain energy per unit volume. We discuss in this paper samples with lateral dimensions which are a few orders of magnitude larger than than the thickness. This allows us to neglect the effect of finite lateral dimensions also.

Si/Ge alloys and superlattices have to be grown at elevated substrate temperatures to achieve monocrystalline growth. The upper limit is set by the condition of planar growth[11] and for superlattices also by the diffusion length. Substrate temperatures therefore are chosen between 550 and 750 ^{o}C, the optimum depending on the Ge concentration. Here the lattice parameters and the elastic constants have values different from those at room temperature. To our knowledge the effect of temperature on the elastic constants of Si and Ge has not been investigated yet, and consequently only the variation in lattice parameters can be discussed quantitatively. $Si_{1-x}Ge_x$ alloys have a stress-free lattice constant[12] which is larger than that of the Si substrate. Due to the fact that Ge has a larger thermal expansion coefficient than Si, cooling down the substrate and epitaxial film will reduce the elastic energy imposed by the substrate and consequently, no extra misfit dislocations will be generated. At a growth temperature of 550 ^{o}C the difference in lattice constants between Si and Ge is 0.0236 nm while this difference at room temperature is 0.0226 nm. However, the difference in expansion of the deposited film and the Si substrate is more significant. In this paper we refer all lattice constants and misfits to room temperature. If we asssume that the thermal expansion of $Si_{1-x}Ge_x$ alloys varies linearly with the Ge concentration x, the misfit between film and substrate is $\Delta\varepsilon = x\cdot(\varepsilon_{Ge}(T) - \varepsilon_{Si}(T))$ larger than at room temperature. Here $\varepsilon_{Ge}(T)$ and $\varepsilon_{Si}(T)$ are the strains of pure Ge and Si due to thermal expansion at temperature T. The numerical values[9] for these strains are $\varepsilon_{Ge}(550^oC)= 3.6\text{x}10^{-3}$,$\varepsilon_{Ge}(750^oC)= 5.2\text{x}10^{-3}$, $\varepsilon_{Si}(550^oC)= 2.0\text{x}10^{-3}$ and $\varepsilon_{Si}(750^oC)= 2.8\text{x}10^{-3}$. For a $Si_{0.5}Ge_{0.5}$ alloy grown at 750 ^oC the misfit is 2.06% at room temperature and 2.18% during growth.

In the next section we discuss the model which describes the relation between thickness and strain in the film and compare it with experimental data reported in literature.[11,13-15] In the last section we show, on the basis of compositionally modulated superlattices, that the energy barrier introduced in our model for the generation of misfit dislocations, can be crossed by thermal activation. In between the fabrication of these superlattices is described and is shown that for the present purpose these superlattices can be treated as alloys with the same average composition.

CRITICAL THICKNESS

One of the possible mechanisms, reported in literature, for the generation of a misfit dislocation line at the interface between an epitaxial, lattice mismatched, film and the substrate is the nucleation and expansion of a semicircular slip loop in the film[5] (see fig.2). The film thickness at which misfit dislocations will be generated has been obtained from the forces that act on the dislocation lines.[5] We derive an expression for the critical thickness based on energy considerations.

The elastic energy per unit length of a screw dislocation is commonly written as

$$\frac{Gb^2}{4\pi}\ln(\frac{\alpha R}{b}) \qquad (1)$$

with R the smallest distance to the free surface, b the length of the Burgers vector, G the shear modulus and α the core parameter which takes into account the core energy of the dislocation. Due to the limited knowledge about the core, an exact determination of the core parameter is not possible. Calculations[16] indicate that α~4 for a srew dislocation in diamond structures such as Si and Ge. In the Peierls-Nabarro model, α depends on the type of dislocation and varies for dislocations with a Burgers vector b=<110>/2 in a {111} glide plane from 3.7 for an edge (ν=0.28) to 4.4 for a pure screw dislocation. The energy of a semicircular slip loop (see fig.2) with radius R and Burgers vector b in the plane of the loop is[17]

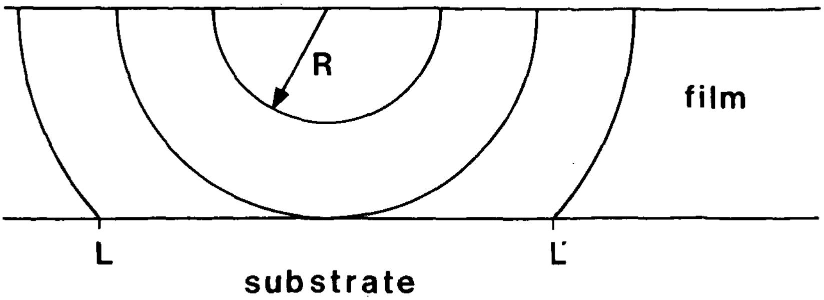

Fig.2 The generation of a misfit dislocation line LL' by nucleation and expansion of a semicircular slip loop with radius R

$$E_d = \frac{\pi R(2-\nu)Gb^2}{8\pi(1-\nu)}\left[-\ln\left(tg\frac{b}{8\alpha R}\right) - 2\cos\frac{b}{4\alpha R}\right] \tag{2}$$

The character of the dislocation changes along the loop from pure edge to pure screw. This expression for the energy is based on a continuum theory and therefore loses its validity when R reaches atomic dimensions. Its exact range of validity depends on the accuracy of the description of the core energy. We are only interested in loops with a radius much larger than the atomic dimensions, which allows us to simplify eq.2. If $R >> b/8\alpha$, so that $tg(b/8\alpha R) \sim b/8\alpha R$ and $\cos(b/4\alpha R) \sim 1$, eq.2 reduces to

$$E_d = \frac{\pi R G b^2(2-\nu)}{8\pi(1-\nu)}\left[-2 + \ln\left(\frac{8\alpha R}{b}\right)\right]. \tag{3}$$

The epitaxial film is subject to biaxial stress and due to the symmetry of the (001) plane the elastic energy per volume is

$$f = \kappa \cdot \varepsilon^2 = 2G\,\frac{1+\nu}{1-\nu}\varepsilon^2, \tag{4}$$

where κ equals $c_{11} + c_{12} - 2c_{12}^2/c_{11}$ and ε is the strain of the film parallel to the interface. This strain is equal to the misfit between the epitaxial film and the substrate as long as no misfit dislocations have been generated. We assumed free relaxation of the strain perpendicular to the film. The released elastic energy when the strain decreases by $\Delta\varepsilon$ is

$$\Delta f = 2G\,\frac{1+\nu}{1-\nu}\varepsilon \cdot 2\Delta\varepsilon. \tag{5}$$

Strain in an epitaxial film can be relaxed by dislocations. Parallel edge dislocations of strength b, separated a distance p, reduce this strain with b/p. In a slip system the strain reduction is determined by the Schmid factor $\cos\varphi_1\cos\varphi_2$ and is

$$b\cos\varphi_1\cos\varphi_2 / p, \tag{6}$$

where φ_1 is the angle between the slip direction and that direction in the interface which is perpendicular to the line of intersection of the slip plane and the surface. The angle between the surface and the normal to the slip plane is indicated by φ_2. For the first loop in the film, p is the size of the film in the direction perpendicular to the dislocation line. It has to be realized that eq.5 provides the energy of a square array of dislocations and thus has to be devided by two to obtain the energy for one loop. Each loop releases strain in a volume $p\pi R^2/2$. Combining eqs. 5 and 6 leads to the following expression for the elastic energy E_e released by a semicircular slip loop with radius R in a film with strain ε

$$E_e = \frac{\pi R^2}{2} b2G(\frac{1+\nu}{1-\nu})\, \varepsilon \cos\varphi_1\cos\varphi_2. \tag{7}$$

In $Si_{1-x}Ge_x$ alloys the slip direction is <110> in the slip planes {111} which gives a Schmid factor $1/\sqrt{6}$ in eq. 7. At the surface the half loop creates a step with an energy

$$E_s = 2R\sigma b\sin\varphi_3, \tag{8}$$

where σ is the surface tension and φ_3 the angle between the dislocation line and its Burgers vector. The half loop might not be perfect and stacking faults with an energy γ will attribute an energy $\pi R^2\gamma/2$ to the loop. We will neglect this contribution to the energy and also assume that no partials are formed.

Until here we discussed the change in elastic energy due to the nucleation of a dislocation loop. To obtain the free energy we also need to know the entropy of the loop. Following the arguments of Nabarro[18] the first contribution to the entropy is the positional entropy of the loop which takes into account the number of ways a loop can be formed in the crystal. Realizing that such a loop lies in a {111} plane, the core of the dislocation may be found on one of the six nearest neighbour atoms in this plane. This gives a contribution of $-1.6k_BT$ per atom on the loop to the free energy, which is an overestimation of its real contribution. The increase in vibrational entropy, arising from lattice distortions around a dislocation, provides a contribution of about $-2k_BT$ per atom to the free energy. For a semicircular loop with radius R we obtain a contribution of the entropy

$$G_S \approx -3.6\, k_BT\pi R/b, \tag{9}$$

where b is the nearest neighbour distance in the {111} plane.

The total free energy

$$G_l = E_d - E_e + E_s + G_S \tag{10}$$

of this perfect semicircular loop increases from zero, when there is no loop (R=0) to a maximum value at $R=R_{max}$ and decreases when the loop expands (see figure 3). When the radius of the loop passes a critical value R_{crit} at which $G_l=0$ again, the system is in a state of lower energy than before the formation of the loop. The radius at which the energy is maximum is provided by the condition $dG_l/dR = 0$, and is

$$R_{max} = \frac{\sqrt{6}b(2-\nu)}{16\pi(1+\nu)\varepsilon}\left[-1 + \ln\left(\frac{8\alpha R_{max}}{b}\right) + \frac{8\sigma(1-\nu)}{Gb(2-\nu)} - \frac{28.8\pi(1-\nu)k_BT}{Gb^3(2-\nu)}\right]. \tag{11}$$

Here we used the appropriate values for φ_1, φ_2 and φ_3 to simplify the equation. The last two terms cancel out using the numerical values for temperatures discussed in this paper.

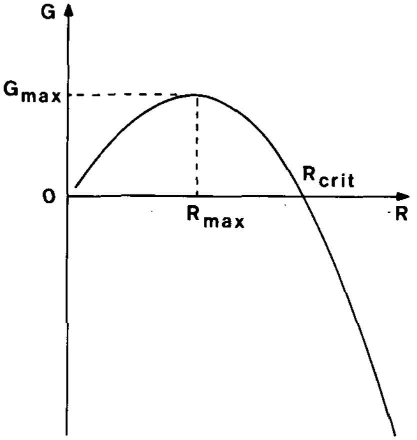

Fig.3 The energy of a semicircular slip loop as a function of its radius. The energy barrier G_{max} has to be crossed to reach R_{crit}, the critical radius for the expansion of these loops.

Matthews[5] argues that if the film thickness is such that a half loop of radius R_{max} cannot fit in the film, the nucleation will not occur, and the film remains coherent. This argument is in fact based on 'forces' acting on the loop. For $R<R_{max}$ the driving 'force' dG_l/dR expels the loop and for $R>R_{max}$ it enlarges the loop. In contrast we base our discussion on purely energy considerations. A half loop will only expand to generate a misfit dislocation line when $R>R_{crit}$. Each state of a loop with a radius smaller than R_{crit} is not the state with the lowest possible energy because the energy of the system without a loop is lower.

The critical radius is provided by the condition G_l=0 and is given by the condition

$$\frac{b}{8R_{crit}}[\ln(\frac{8\alpha R_{crit}}{b})-2]=\frac{\pi(1+\nu)\varepsilon}{\sqrt{6}(2-\nu)}. \tag{12}$$

For films with orientation (001) parallel to the surface and the semicircular loop in the (111) plane, the critical thickness below which the loops can not expand is

$$h_{crit}=R_{crit}\sqrt{2/3}. \tag{13}$$

The numerical value of this critical thickness is about two times the value obtained by the 'force' model of Matthews. The critical thickness is a size barrier beyond which the loop can expand provided that the activation energy G_{max} (see fig.3) to cross the energy barrier is present. In our model this activation energy

$$G_{max}=\frac{R_{max}Gb^2(2-\nu)}{16(1-\nu)}[\ln(\frac{8\alpha R_{max}}{b})-3] \tag{14}$$

is the energy G_l of the semicircular loop with a radius R equal to R_{max}.

In figure 4 the curve indicated by our proposed energy model (EM) shows the relation between critical thicknesses and the strain ε, according to eqs.12 and 13. We assume a constant value for the core parameter α equal to 4 in the calculations. This curve fits remarkably well to the results of Kasper et al.[7,13] (closed circles) without any adjustable parameters. Also indicated in figure 4 are the measurements of Bean et al.[11,14,15] (triangles). To explain these large critical thicknesses, People and Bean[19] derived a semi-empirical relation between the critical thickness of the film and the misfit. With the assumption that misfit dislocations will be generated when the strain energy per unit area, $h\kappa\varepsilon^2$, exceeds the energy of a non interacting screw dislocation $(Gb/20\pi)\ln(h/b)$ at a distance h from the free surface and a dislocation width of 5b they obtained

$$\varepsilon^2=\frac{1.9\text{x}10^{-3}\text{ nm}}{h_c}\ln(\frac{h_c}{0.4\text{nm}}), \tag{15}$$

with h_c the critical thickness. This relation is shown in figure 4 as curve PB. The assumptions on which this relation is based are, however, not quite clear to us. Recently Marée et al.[8] expanded this model by taking into account the 60^o mixed type of dislocation, the dissociation in partials and the core energy of the dislocation. However, they made the same assumptions with respect to the generation of misfit dislocations. Their model predicts a difference in critical thickness between films which are under compressive and those which are under tensile stress. Because they took into account the formation of partials, the energy of the dislocations is less than that of People and Bean. This results in a curve which lies between the curve of our model (EM) and PB .

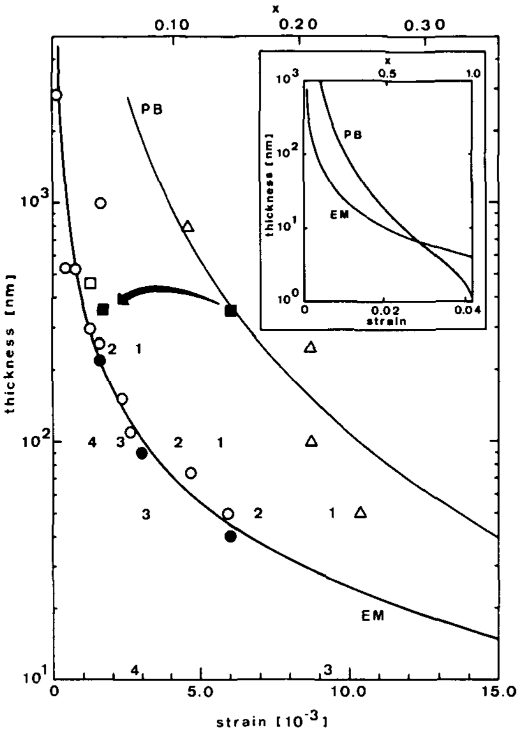

Fig.4 Layer thickness as a function of the strain in the film. Films with a thickness less than the critical value corresponding to their Ge concentration x (upper horizontal scale) are pseudomorphic. Experimental critical thicknesses are indicated by triangles (Bean et al., see refs.14 and 15) and closed circles (Kasper et al., see ref.13). The strain of films with misfit dislocations present is indicated by open circles (ref.13) and numbers 1 to 4 for films with a Ge concentration of 30, 50, 70 and 100% (ref.15). The present work (see text) is indicated by open (sample 3009) and closed (sample 2909) squares and the arrow illustrates the effect of heating as discussed in the text. Theoretical curves are indicated by PB (ref.19) and EM (present work). The inset shows these curves for a larger range of strains, corresponding to a Ge concentration up to 100%.

Despit the fact that Bean et al. obtained much larger critical thicknesses than provided by our model, their results do not contradict our model. The curve EM in figure 4 yields the critical thickness if the energy barrier G_{max} (see fig.3) can be crossed. In the framework of our model the difference in critical thicknesses between the films of Bean et al. and Kasper et al. can be explaned by the assumption that under the growth conditions of Kasper et al. the activation energy G_{max} is present and that this energy is not available for Bean's samples. Therefore it is important to know the experimental conditions, which we will discuss only briefly. Kasper et al. grew their $Si_{1-x}Ge_x$ alloys and superlattices by electron beam evaporation in an ultra high vacuum (UHV) apparatus. During growth with a typical deposition rate of 0.5 nm/s their Si substrates were kept at a temperature of 750 ^oC. They measured the average distance between misfit dislocation lines by means of transmition electron microscopy (TEM) for three different Ge concentrations and several layer thicknesses. Bean et al. grew their $Si_{1-x}Ge_x$ alloys at a lower substrate temperature of 550 ^oC. In contrast with Kasper et al. they derived the critical thickness from ion backscattering and x-ray diffraction. They defined the critical thickness by the value at which the tetragonal distortion no longer increased linearly with the Ge concentration.

If our model gives the correct description of the misfit dislocation generation in Si/Ge alloys and superlattices, all samples with a 'critical' thickness larger than the value provided by eqs.12 and 13 (curve EM in fig.4) should be thermodynamically unstable. To support our model we induced misfit dislocations in Si/Ge superlattices, grown under the same conditions as Bean et al., by thermal activation. Before we discuss this experiment, we first discuss our experimental conditions and show that the Si/Ge superlattices under consideration can be treated as alloys with the same average composition.

SUPERLATTICES

Our superlattices were grown in an UHV apparatus which has a turbo molecular pump, a titanium sublimation pump and several liquid nitrogen shrouds to reach a base pressure in the upper 10^{-9} Pa domain. Two electron beam evaporators provide the possibility of simultaneous deposition of two materials. The evaporation rate is controlled with a mass spectrometer as sensor in the feedback loop[20]. The composition modulation was achieved by modulating the Ge depostion rate sinusoidally while the Si rate was kept constant. The Si(001) substrates on which the superlattices were grown, were cleaned using Henderson's[21] procedure and heated *in situ* for a short time at 1150 ^oC. During deposition of the superlattices the substrates were held at a temperature of 550 ^{o}C. The pressure rose during the epitaxial process to about 5×10^{-7} Pa. X-ray photographs showed that the growth plane of the superlattices was (001) and that the orientation of the superlattices with respect to the substrate is $(001)_{sl}$ // $(001)_{sub}$ and $[100]_{sl}$ // $[100]_{sub}$. This shows that epitaxial growth is achieved. First we discuss the elastic energy in these compositionally modulated superlattices and then the influence of the modulation on the nucleation of dislocation loops is discussed briefly.

The elastic energy of the superlattices is given by eq.4 with a strain ε which varies periodically in the direction perpendicular to the substrate. To obtain the strain ε as a function of the z-coordinate in the direction of modulation we use that $Si_{1-x}Ge_x$ alloys obey Vegard's law, which means that their lattice constant can be written as $a_{SiGe} = a_{Si} + x\cdot\delta a$,with a_{Si} = 0.5431 nm and $\delta a = a_{Ge}-a_{Si}$ = 0.0226 nm at room temperature and x the Ge concentration. When the epitaxial film of the alloy is accommodated to the substrate by elastic strain this strain parallel to the substrate is

$$\varepsilon = -x\cdot\delta a/a_{SiGe}\,. \qquad (16)$$

In our superlattices the modulation in the concentration is in good approximation sinusoidal and thus the Ge concentration can be written as

$$x = x_0[1 + \eta\sin(2\pi z/\Lambda)]\,, \qquad (17)$$

with x_0 ,η and Λ the average concentration and the modulation amplitude and period. If the superlattice is accommodated to the substrate by strain, the lattice constant parallel to the substrate is equal to a_{Si} throughout the whole film. The elastic energy then is in a first order approximation equal to

$$f' = \kappa(1 + \eta^2/2)x_0^2(\delta a/a_{SiGe})^2\,, \qquad (18)$$

with a_{SiGe} the lattice constant of the stress-free alloy with a Ge concentration equal to the average concentration x_0 in the superlattice. The elastic energy in a sinusoidally modulated superlattice thus is enlarged by a factor $(1 + \eta^2/2)$ with respect to the alloy of the same average composition. When a sinusoidally modulated superlattice which is initially in a state given by eq.18 relaxes, i.e. by misfit dislocations, to the energy state without substrate-induced strain it releases an amount of elastic energy equal to

$$\kappa x_0^2(\delta a/a_{SiGe})^2\,. \qquad (19)$$

This is the same amount of elastic energy which is released when an alloy with the same average composition relaxes from the strain state given by eq.16 to the stress free state. This allows us to proceed as if the superlattice were an alloy concerning the elastic behaviour of the superlattice. The only assumption we have to make is that the anisotropy which is inherent to superlattices does not influence the elastic behaviour significantly.

In comparison with the elastic behaviour, the effect of the substitution modulation on the dislocations is less clear and there is only a little literature concerning multilayers.[13,22] The modulation function in these multilayers is ideally a square wave. $Si_{0.85}Ge_{0.15}/Si$ multilayers[13] e.g., indicated that misfit dislocation lines were formed at the interface between the Si-substrate and the film if the separate layers in the superlattice were thinner than the critical thickness of alloys with the same composition. The distance between misfit dislocation lines was almost equal to the distance in an alloy with the same average composition. In our superlattices the modulation period is about 3 nm and much smaller than the critical thicknesses of the corresponding alloys. There are no sharp interfaces in our superlattices due to the sinusoidal composition modulation. For these two reasons it is likely that also with respect to dislocations our superlattices can be treated as if they were alloys.

We will discuss two superlattices, one with a thickness smaller (sample 2909) and one with a thickness larger (sample 3009) than the critical value according to People and Bean. Both sinusoidally modulated superlattices have a modulation amplitude, as defined in eq.17, of 0.56. Due to the substrate-enforced strain, both samples are tetragonally distorted with respect to the cubic symmetry in stress-free alloys. The lattice constants of sample 2909 are 0.5431(2) nm parallel, and 0.5488(2) nm perpendicular to the substrate. This is in agreement with the PB model because this sample has a thickness below the critical value of that model and thus the lattice constant parallel to the substrate is equal to the lattice constant of bulk Si. In the other sample, misfit dislocations relax a considerable fraction of the misfit between film and substrate and the lattice constants are 0.5485(2) nm parallel and 0.5502(2) nm perpendicular to the substrate. The modulation periods in samples 2909 and 3009 are determined by the 105 and 146 periods counted during deposition and the sample thicknesses of 350 and 450 nm measured afterwards. The results are in agreement with the periods of 3.4 and 3.2 nm obained by x-ray diffraction. We take the ratio $2c_{12}/c_{11}$ of the stiffness constants to be 0.76, which is the average value for Si and Ge. With the lattice parameters as mentioned before, the average Ge concentration was calculated to be 0.14 and 0.27 for samples 2909 and 3009. This is in agreement with the concentrations 0.15 and 0.28 obtained from the thicknesses of the superlattices and simultaneously deposited layers of pure Si. Photographs made by an optical microscope (see figure 5) show the surface steps in the <110> directions. The presence of these steps in sample 2909 indicates that there are misfit dislocations in this sample although the lattice constant parallel to the substrate was observed to be that of the Si-substrate. This is explaned by the fact that the dislocation density is so low that the released strain is not observable by the x-ray diffraction technique we used. This allows us to interpret the thickness of this sample as the critical thickness for this particular Ge concentration as is indicated in figure 4.

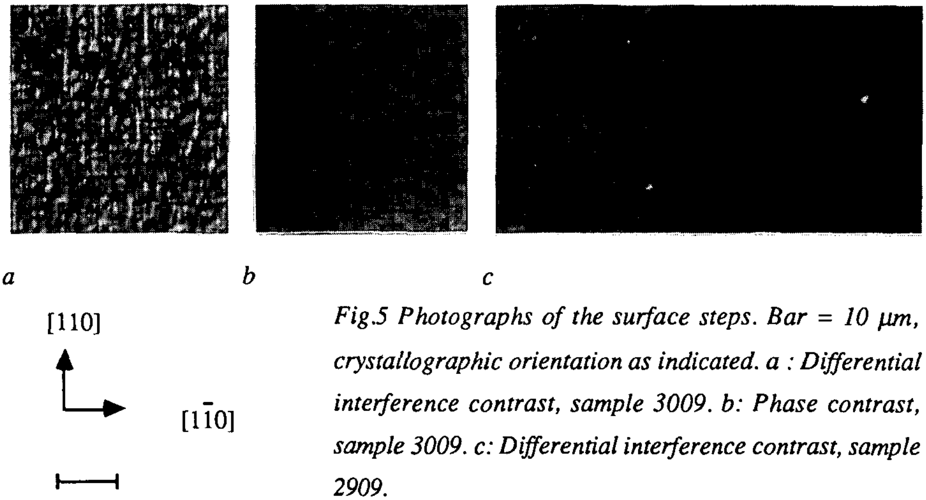

Fig.5 Photographs of the surface steps. Bar = 10 μm, crystallographic orientation as indicated. a : Differential interference contrast, sample 3009. b: Phase contrast, sample 3009. c: Differential interference contrast, sample 2909.

ENERGY BARRIER AND STRAIN

Thusfar we have discussed the relation between the critical thickness and the strain of a film enforced by the substrate. The critical thickness is obtained by eq. 12 if the strain is substituted by the misfit between film and substrate. Knowledge of this critical thickness is important for the fabrication of dislocation-free samples. As long as the interaction between dislocations can be neglected and the thickness of the film is less than the distance between misfit dislocation lines, the models which provide the critical thickness can also be used to obtain the strain-thickness relation of an epitaxial film. In our model this implies that, instead of the misfit, the actual elastic strain has to be substituted in eq.12. The difference between misfit and this strain is then accommodated by misfit dislocations at the interface. Because there is no longer a fixed ratio between the strain in the film and the Ge concentration, the upper horizontal scale in figure 4 loses its relevance for these samples and the lower one has to be used. Under the conditions mentioned above, all films with equal thickness will have the same strain, independent of their composition, provided that the thickness exceeds the critical value corresponding to the concerning Ge concentration. The relation between thickness and strain in this case is provided by the curve EM in figure 4 and by eqs.12 and 13. The experiments of Kasper et al., indicated in figure 4 by open circles, clearly illustrate that films with a thickness larger than the critical value still obey our model. The experiments of Bean et al., however, show a different behaviour as figure 4, where we indicated their strain-thickness relations by the numbers 1,2,3 and 4 for Ge concentrations of 0.3, 0.5, 0.7 and 1.0, reveals. The strain appears to depend on the Ge concentration or, what is equivalent, on the distance between misfit dislocation lines and is no longer a function of the thickness only. This implies that the curve PB, which provides the 'critical' thickness for these films, fails to describe the strain-thickness relation for films in which misfit dislocations are present. Before being able to discuss these results in more detail we have to discuss the experiments which support our idea that the PB model, and all other models which provide a 'critical' thickness larger than the one provided by our model, describe a thermodynamically unstable state.

In order to see whether it is possible to generate misfit dislocations in films thicker than the critical value provided by the EM model, we heated sample 2909 which was grown at 550 ^{o}C, during a few minutes at 750 ^{o}C. After this heat treatment the strain in this sample relaxed to a value close to the strain predicted by the EM model as is shown by the arrow in figure 4. This indicates that the activation energy G_{max} for the nucleation as given by eq.14 can be obtained by a thermal process. A photograph of the surface (fig.6) shows the characteristic square pattern[23] of the <110> dislocation lines.

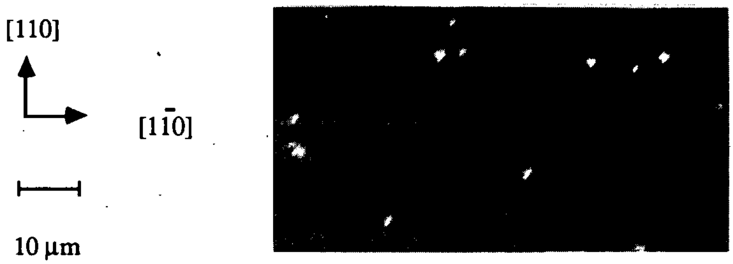

Fig.6 *Differential interference contrast photograph of the surface steps in sample 2909 after the heat treatment as discussed in the text.*
Bar = 10 μm , crystallographic orientation as indicated.

This experiment does not give an answer on the question whether thermal activation or another thermal effect, e.g. the temperature dependence of the elastic constants or critical stress,[24] is responsible for the strain relaxation. This information can be be obtained by measuring the strain in the film as a function of time. The rate of thermally activated processes can be written as

$$v = A\,\omega \exp(\frac{-U}{k_B T}), \tag{20}$$

where ω is a characteristic frequency, U the activation energy and A a constant. This implies that even at low temperatures the process continues, although at a much slower rate than at high temperatures. If the nucleation of semicircular dislocation loops as described by our model is a thermally activated process, samples as 2909 which has a thickness larger than the critical value of our model, should relax strain until the strain obeys eqs.12 and 13. To check this, a sample from the same series as 2909 was heated at 500 °C and we measured by x-ray diffraction the strain of the film parallel to the substrate as a function of the elapsed time. We should note that this 500 °C is below the growth temperature and thus no influence of temperature is expected apart from thermal activation. The strain parallel to the interface is obtained from the reflections (004), (115) and (335) with the assumption that the film has a tetragonal crystal structure. Figure 7 shows the results of these measurements. The decrease of the strain shows that the nucleation can be described by thermal activation and that the film which initially obeyed the relation of People and Bean was at that moment in a thermodynamically unstable state.

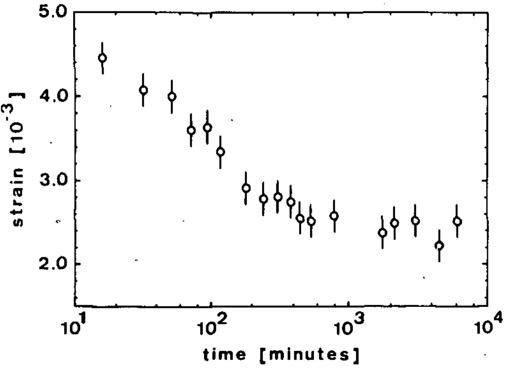

Fig.7 The strain, parallel to the substrate, in the film as a function of the time of heating at 500 °C.

Our sample 3009, with a germanium concentration of 0.27 and a thickness larger than the critical value is also indicated in figure 4. The growth conditions for this sample were identical to those of sample 2909 which obeyed the relation of People and Bean.

DISCUSSION

It is possible to grow Si/Ge alloys without misfit dislocations up to a thickness which is larger than the critical value provided by our model. It is shown by Bean et al. and by us that for the growth at a temperature of 550 ^{o}C a different 'critical' thickness can be defined according to the relation of People and Bean. Our experiment, where we heated a film grown at 550 ^{o}C for some time at 500 ^{o}C, shows that such films are thermodynamically unstable with respect to the strain in the film. This implies that the relation of People and Bean describes a non-equilibrium state and thus is only valid for specific growth conditions especially with respect to the time these films are kept at an elevated temperature. Films grown with different deposition rates will therefore have different 'critical' thicknesses. For device applications it is important to realize that in films which are initially pseudomorphic, dislocations will be generated with a considerable rate at elevated temperatures even if these temperatures are below the growth temperature. Films with a thickness less than the critical value provided by our model are thermodynamically stable and so this value sets the limit for pseudomorphic growth.

In films were the interaction between dislocations can be neglected, the curve EM in figure 4 provides also the relation between strain in the film and its thickness for films thicker than the critical value at thermodynamical equilibrium. This implies that the minimum strain in such films is determined by their thickness only. There will be no more misfit dislocations generated in a film with this minimum strain. Si/Ge alloys and superlattices grown on Si substrates therefore will always be tetragonally distorted. The degree of tetragonal distortion is determined by the thickness of the film. From our heating experiments we conclude that all films with a thickness larger than the value given by curve EM in figure 4 (e.g. the films indicated by the numbers 1 and 2) are thermodynamically unstable. Due to the non-equilibrium character of the phenomena that determine the strain in these films, a model description of these films will be rather difficult.

The residual strain in the sample grown at 550 ^{o}C and heated at 500 ^{o}C for about three days is larger than the value provided by our model. Because we heated the sample after it had been exposed to air, the oxide layer on the film might influence the generation of dislocations and the strain. As mentioned before, the temperature influences the generation of dislocations because the elastic constants of the alloy will be different at 750 and 500 °C. The energy barrier G_{max}, which is calculated to be 8000 k_BT for sample 2909, using the elastic constants at room temperature, is roughly proportional to the shear modulus. Knowledge of the temperature dependence of the elastic constants therefore is essential for further understanding of the generation of misfit dislocations.

The curve EM in figure 4 is based on the 60° type of misfit dislocation and on the assumption that a continuum theory is applicable. Recent TEM observations[25] confirmed that the misfit dislocations for Ge concentration less than 50% are of the 60° type. However, for Ge grown on Si a pure edge type of dislocation was observed. Such an edge dislocation reduces the critical thickness for Ge (x=1) in our model from 5.2 to 1.4 nm. Monte Carlo simulations[26] indicate a significant deviation of atomistic from continuum theories for critical thicknesses in the order of a few nanometer. Both the TEM observations and the Monte Carlo simulation indicate that the quantitative results of our model have to be applied with reserve to Si/Ge alloys and superlattices in which the Ge concentration is larger than roughly 50%. This suggest a possible explanation for the observed small residual stress in the $Si_{0.3}Ge_{0.7}$ and Ge films, indicated in figure 4 by the numbers 3 and 4. This shows that a detailed study of misfit dislocations in films with a Ge concentration larger than 50% and which are at thermodynamical equilibrium is essential for further understanding of misfit dislocation generation in these films. We have shown that the generation of misfit dislocations in films with a low Ge concentration can be described by the EM model.

CONCLUSIONS

We have introduced a model, based on the nucleation and expansion of semicircular slip loops, that describes the observed relation between the strain in an epitaxial Si/Ge film grown on a Si substrate and its thickness. We have also shown that films with a thickness larger than the critical value provided by our model are thermodynamically unstable.

Acknowledgments. We would like to thank Mr. P.F.Colijn of the department of Material Science for making the photographs and prof.A.van den Beukel for a useful discussion.
This work is supported by the Foundation for Fundamental Research on Matter (F.O.M.).

REFERENCES

1. F.C.Frank and J.H.van der Merwe, Proc.Roy.Soc.A **189**, 205 (1949).
2. J.W.Matthews, Phil.Mag. **6**, 1347 (1961).
3. P.Delavignette, J.Tournier, and S.Amelinckx, Phil.Mag. **6**, 1419 (1961).
4. J.H.van der Merwe, J.Appl.Phys. **34**, 123 (1963).
5. J.W.Matthews, J.Vac.Sci.Technol. **12**, 126 (1975)..
6. J.W.Matthews, S.Mader, and T.B.Light, J.Appl.Phys. **41**,3800 (1970).
7. E.Kasper and H.-J. Herzog, Thin Solid Films **44**, 357 (1977).
8. P.M.J.Marée, J.F.van der Veen, K.L.Kavanagh, J.C.Barbour,C.W.T.Bulle-Lieuwma, and M.P.A.Viegers, J.Appl.Phys. **62**, 4413 (1987).
9. D.E.Gray, ed., *American Institute of Physics Handbook* (McGraw-Hill, New York, 1972).
10. S.Luryi and E.Suhir, Appl.Phys.Lett. **49**, 140 (1986).
11. J.C.Bean, T.T.Sheng, L.C.Feldman, A.T.Fiory, and R.T.Lynch, Appl.Phys.Lett. **44**, 102 (1984).
12. H.Stöhr and W.Klemm, Z.Anorg.Chem. **241**, 314 (1939).
13. E.Kasper, H.J.Herzog, and H.Kibbel, Appl.Phys.**8**, 199 (1975).
14. A.T.Fiory, J.C.Bean, L.C.Feldman, and I.K.Robinson, J.Appl.Phys.**56**, 1227 (1984).
15. J.C.Bean, L.C.Feldman, A.T.Fiory, S.Nakahara, and I.K.Robinson, J.Vac.Sci.Technol. A **2**, 436 (1984).
16. A.Maradudin, J.Phys.Chem.Solids **9**, 1 (1959).
17. J.P.Hirth and J.Lothe, *Theory of dislocations*, (Wiley, New York, 1982).
18. F.R.N.Nabarro, *Theory of crystal dislocations*, (Clarendon, Oxford, 1967).
19. R.People and J.C.Bean, Appl.Phys.Lett. **47**, 322 (1985) and Appl.Phys.Lett. **49**, 229 (1986).
20. R.H.M.van de Leur, A.J.G.Schellingerhout, J.E.Mooij, and F.Tuinstra Appl.Phys.Lett. **52**, 1005 (1988).
21. R.C.Henderson, J.Electrochem.Soc.**119**, 772 (1972).
22. J.W.Matthews and A.E.Blakeslee, J.Crystal Growth **27**, 118 (1974).
23. E.P.Kvam, D.J.Eaglesham, C.J.Humphreys, D.M.Maher, J.C.Bean, and H.L.Fraser in *Microscopy of Semiconducting Materials*, edited by A.G.Cullis and P.D.Augustus, (Inst. Phys. Conf. Ser. No.87, 1987) pp.165-168.

24. J.Y.Tsao, B.W.Dodson, S.T.Picraux, and D.M.Cornelison, Phys.Rev.Lett. **59**, 2455 (1987).
25. Y.Kohama, Y.Fukuda, and M.Seki, Appl.Phys.Lett. **52**, 380 (1988).
26. B.W.Dodson and P.A.Taylor, Appl.Phys.Lett. **49**, 642 (1986).

CHAPTER 5

FABRICATION OF LOW-CAPACITANCE JOSEPHSON-JUNCTIONS

A.J.G. Schellingerhout, C.A. v.d. Jeugd, J.Romijn and J.E. Mooij

Department of Applied Physics and Centre for Submicron Technology,
Delft University of Technology,
Delft, The Netherlands

A procedure is developed to fabricate very small area (0.01 μm^2), low-capacitance Josephson-junctions, using a shadow evaporation technique. In this procedure a free-hanging bridge is used of size 0.1 μm x 0.25 μm. Wet-etching yields insufficient resolution for this purpose. Therefore reactive ion-beam etching (RIBE) was employed to fabricate the bridge as described in this paper.

A tri-level resist stencil [1] is used consisting of a high-molecular weight PMMA of 100 nm thick on a germanium intermediate layer of 25 nm on top of a 300 nm thick polyimide layer. After e-beam exposure and development, the pattern containing the bridges of 0.1 μm x 0.25 μm is transferred to the germanium layer with RIBE using CCl_2F_2. The bridge is formed with RIBE of the polyimide using O_2 at an angle of 45° and 135° with respect to the surface of the substrate. For the RIBE a home-made Kaufman-type [2] ion-source is used. The junctions are obtained by subsequent evaporation of the first electrode-metal at an angle of 60°, oxidizing in O_2-atmosphere and evaporation of the second electrode-metal at an angle of 120 °

bridge (0.1 μ m x 0.25 μ m)

CCl_2F_2 -RIBE of Ge

tri-level resist stencil

O_2 - RIBE of polyimide

PMMA etch-mask

Junction fabrication

Fig.1 Scheme of the fabrication process.

REFERENCES

[1] L.D. Jackel, R.E. Howard, E.L. Hu, D.M. Tennant and P. Grabbe, Appl. Phys. Lett. 39, 268 (1981)

[2] According to a design of J.M.E. Harper, Research Report, IBM Thomas J. Watson Research Centre, Yorktown Heights, New York.

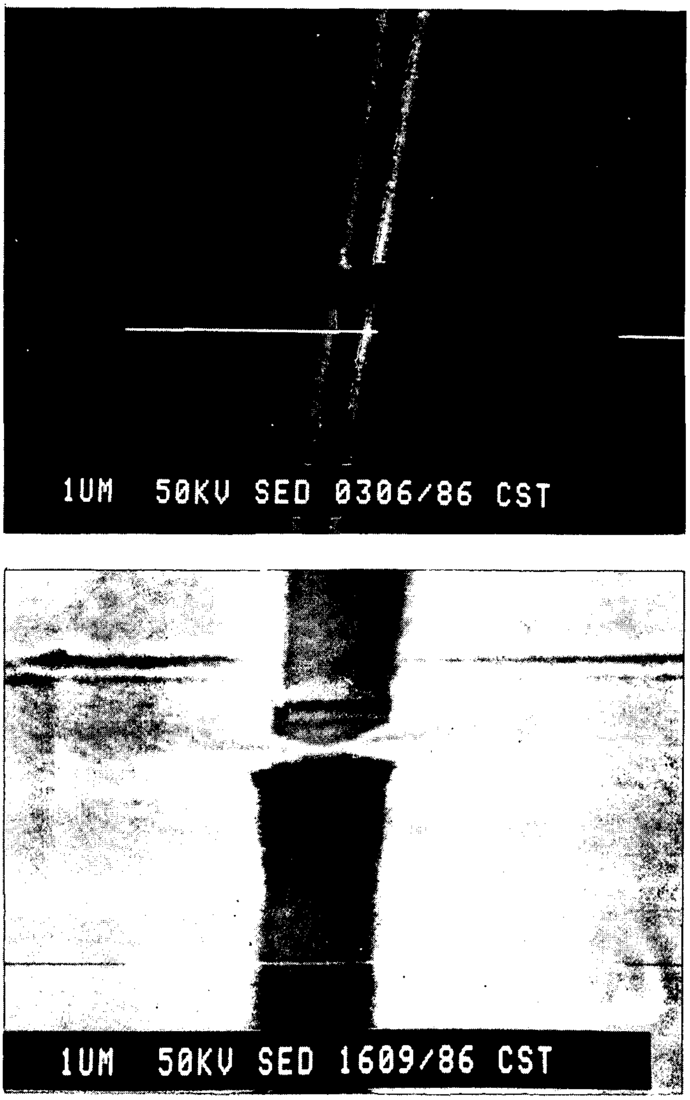

Fig.2 View of the bridge structure.

CHAPTER 6

OXYGEN CONCENTRATION AND MICROSTRUCTURE OF GRANULAR ALUMINIUM

A.J.G. Schellingerhout, J.A. Kokkedee, E.J. van Kersbergen,
J.E. Mooij and T.M. Klapwijk*
Department of Applied Physics, Delft University of Technology, Delft,
The Netherlands
*Department of Applied Physics, University of Groningen, Groningen,
The Netherlands

ABSTRACT

Granular aluminium is fabricated with high quality control of the aluminium flux and partial pressure of oxygen. Results show the critical aspects of the fabrication of the material when the composition is in the vicinity of the metal insulator transition. Based on measurements with a quartz crystal rate monitor, a model is derived for the incorporation of oxygen in granular aluminium during the evaporation of aluminium. The oxygen concentration of granular aluminium with resistivities from 10^{-4} Ωcm to 10 Ωcm, is obtained from four different methods : Rutherford back scattering (RBS), electron probe micro analysis (EPMA), anodization and rate monitoring. These measurements are compared with calculated resistivities as a function of the oxygen concentration. A model for the microstructure of granular aluminium is suggested to explain the experimental results.

INTRODUCTION

Granular aluminium is a material which is fabricated by deposition of aluminium in the presence of a substantial partial pressure of oxygen. The physical properties of this material are strongly dependent on small changes in the aluminium rate relative to the oxygen pressure. Resistivity versus temperature curves for four different oxygen concentrations are shown in fig.1. The drastic changes in the curves are caused by only a factor of two change in the aluminium deposition rate. As is observed, there is large influence on the resistivity, the superconducting critical temperature and temperature dependence of the resistivity. Granular aluminium has been used in many experiments on weak and strong localization and for many investigations concerning superconducting properties. The microstructure has primarily been studied by transmission electron microscopy. Based on these studies, the granular aluminium with a resistivity from 10^{-4} Ωcm to 10 Ωcm, is modeled with metallic grains with an average diameter of approximately 3 nm in an insulating matrix of aluminium.[1] However little is known about the oxygen concentration (or aluminium oxide concentration) in granular aluminium. A clear cut understanding of the dependence of the resistivity on the oxygen concentration is important for experimental as well as theoretical aspects.

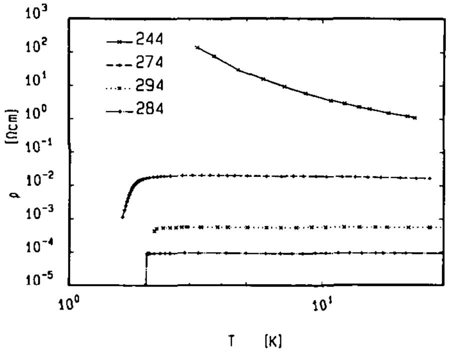

fig.1 Resistivity versus the temperature of the four granular aluminium layers with different oxygen concentrations. Sample 244 is in the insulating regime.

In this paper we report on the fabrication of granular aluminium in an ultra high vacuum (UHV) system with feedback applied to the oxygen flux and to the aluminium flux. Resistance measurements show the very strong dependence of the resistivity on the aluminium rate (with a constant oxygen pressure), which requires tightly controlled fabrication of the material when the composition is in the vicinity of the metal insulator transition. The aluminium flux is measured with a mass spectrometer. Based on calibration of the mass spectrometer output versus the output of a quartz crystal rate monitor with different partial pressures of oxygen, a model is made for the incorporation of oxygen in granular aluminium during the deposition of aluminium. The oxygen concentration of granular aluminium is determined using four different methods: Rutherford back scattering (RBS), electron probe micro analysis (EPMA), anodization and an oxidation model. The measured concentrations are compared with estimates based on simple models for the microstructure of granular aluminium.

FABRICATION

The granular aluminium is fabricated by evaporation on sapphire (012) substrates held at room temperature. The system with all the important components is shown in fig.2. The aluminium is evaporated with an electron gun. The flux of the e-gun and the partial pressure of oxygen are measured with a mass spectrometer, which is time multiplexed between oxygen (measured at mass number 16) and aluminium (measured at mass number 27). The output of the mass spectrometer is demultiplexed in two signals. One is used as the rate signal for the aluminium feedback loop, the other is used as the oxygen pressure signal for the oxygen controller. The rate control of the electron gun has been discussed. [2] A computer generates the reference signals for both feedback loops, which opens the possibility for making multilayer structures with different compositions of the granular aluminium. During fabrication several signals are available with information about the evaporation process. The oxygen channel of the mass spectrometer and the ion gauge give the oxygen pressure. The mass spectrometer is calibrated against the ion gauge prior to every evaporation run. All other background gases can be ignored before and during the evaporation of aluminum, as has been verified by taking mass spectra during open loop deposition. Thus the ion gauge and the mass spectrometer provide output signals only related to the oxygen pressure. The aluminium channel of the mass spectrometer gives the aluminium rate independent of the oxygen background pressure. No Al_xO_y was detectable in the mass spectrum during the evaporation of aluminium, which means that only aluminium and oxygen atoms arrive at the substrate. The quartz crystal is used to calibrate the aluminium rate of the mass spectrometer output signal. During the fabrication of the granular aluminum, the X-tal displays a signal proportional to the deposited mass.

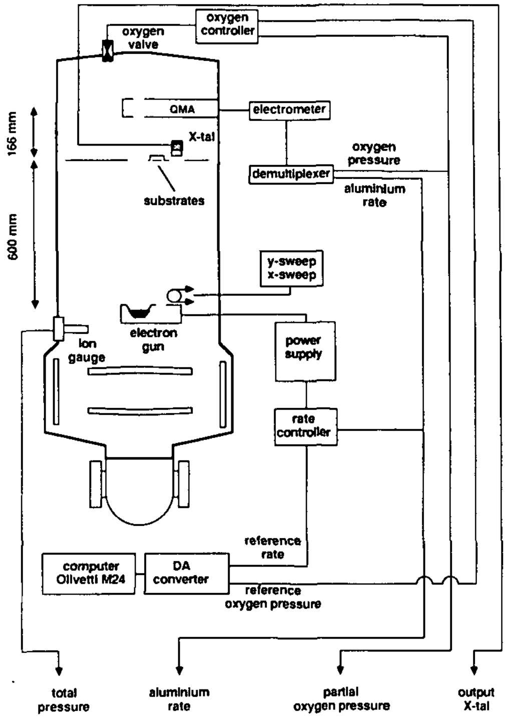

fig.2 Schematic drawing of the UHV system. The position of important components in the evaporation chamber are shown. The electron gun is a Balzers ESQ 300U with filament and wehnelt control. The mass spectrometer QMA is a Balzers QMG 511. The box with x-sweep y-sweep symbolizes the current drivers for the home built high frequency sweeping coils, which are added to the electron gun to improve the stability of the beam profile. The rate controller and the demultiplexer are also home built.

We found that rate control of the aluminium flux was also needed to obtain a stable oxygen pressure. The wide bandwidth output signals of the mass spectrometer showed fast fluctuations in oxygen pressure correlated with fluctuations in the aluminum evaporation rate. This is caused by gettering of oxygen by freshly deposited aluminium on the walls of the evaporator. An estimate, based on an evaporation rate of 0.1 nm/s at a distance of 0.6 m, results in a pumping speed much larger than of the turbo molecular pump (500 l/s). The increase in pumping speed by gettering on the walls was also observable in the calibration constant between the ion gauge and the mass spectrometer. The constant changed with different evaporation rates of aluminium. During the fabrication of the samples the mass spectrometer and not the ion gauge, is used for the oxygen feedback signal. The mass spectrometer is closer to the substrate and will provide the best signal for the flux of oxygen on the substrate. The noise to signal ratio of the aluminium evaporation rate was always smaller than 0.5 % (bandwidth = 1 Hz) in the rate range of 0.04 to 0.3 nm/s. These numbers for the rate stability are based on the noise of the output voltage of the mass spectrometer.

OXYGEN INCORPORATION

During the formation of granular aluminium, oxygen must be incorporated in the deposited film of aluminium. The bonding of oxygen on a clean aluminium surface has been investigated. [3] However, the bonding of oxygen on a growing aluminium layer has, as far as we are aware of, not been studied. If the aluminium is oxidized an extra mass flux will be observable on a quartz crystal rate monitor. The complete oxidation of aluminium to aluminium oxide will lead to the substantial increase of observed mass flux on the crystal with a factor $\alpha = 1.88$, the mass ratio between an Al_2O_3 molecule and two Al atoms. The increase is only observable if the aluminium flux can be controlled independently of the oxygen pressure. This experiment with the quartz crystal can be executed in the present system, because the aluminium flux is controlled independently with the mass spectrometer. The results are shown in fig. 3.

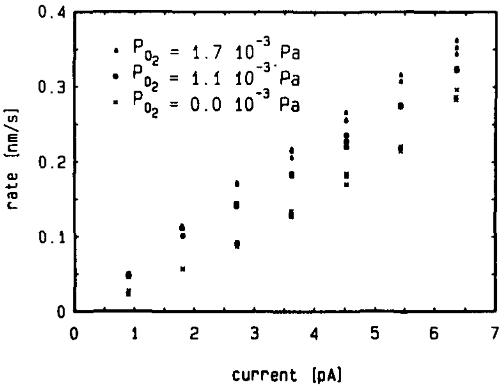

fig.3 Output of the quartz crystal rate monitor versus different settings of the output current of the mass spectrometer. The calibration is repeated for two oxygen pressures. The density $\rho = 2.7\mathrm{x}10^3$ *kg/m*^{3} *which implies that the X-tal output corresponds to the aluminium rate for the points measured with zero back ground pressure of oxygen.*

The output of the quartz crystal for several settings of the output current *I* of the mass spectrometer is shown. The output current of the mass spectrometer, which is set at a constant value by the feedback loop, is related to the aluminium flux. This calibration procedure is performed with no back ground pressure of oxygen, a partial pressure of $1.1\mathrm{x}10^{-3}$ Pa and a partial pressure of $1.7\mathrm{x}10^{-3}$ Pa. A quartz crystal rate monitor measures the mass flux. The mass flux F with unit kg/m^{2}s is obtained from fig.3 by multiplying the rate with the density ρ which was used to program the rate monitor. The density ρ is a scaling factor. In fig. 3 we used $\rho = 2.7\mathrm{x}10^3$ kg/m^3, to make the rate output of the crystal equal to the evaporation rate of aluminium when no oxygen is present. The value of the oxygen pressure is obtained by calibration of the mass spectrometer to the ion gauge prior to the evaporation of aluminium. Some qualitative remarks can be made about fig.3. The calibration curve of the aluminium rate of the crystal versus the output current of the mass spectrometer is nonlinear. This is observed with many materials. The oxygen has an influence on the curves. At high aluminium rates a constant extra mass flux of oxygen occurs, while at low aluminium rates the aluminium seems to oxidize completely, since the extra mass flux of oxygen is independent of the oxygen pressure.

The influence of the oxygen pressure on the position of curves in fig. 3 is explained with a simple model with the assumptions (1) The mass flux of oxygen $F_{O2} = \beta\, p_{O2}$ with p_{O2} is the pressure of oxygen and β is a constant (2) The maximum absorbed mass flux of oxygen $F_{O2} = (\alpha\text{-}1)\, F_{Al}$,with F_{Al} is the aluminium mass flux. The first assumption implies a constant extra mass flux of oxygen independent of the aluminium rate but linear in the back ground pressure while the second assumption means that the complete oxidation of aluminium to stochiometric Al_2O_3 determines the maximum concentration of oxygen. The extra mass flux of oxygen will be independent of the oxygen pressure but linear with the aluminium mass flux. The cross over aluminium flux between the two regimes is $F_{Al} = (\beta\, p_{O2}) / (\alpha\text{-}1)$.

A least squares estimation has been made with the data plotted in fig.3 for α, β and the mass flux of Al for the different output currents of the mass spectrometer $F_{Al}(I)$. To show the predictions of the model more clearly we have replotted the data in fig 4. In this figure we have eliminated the nonlinear back ground of the calibration of the mass flux of aluminium versus the output current of the mass spectrometer by subtracting the least squares optimized aluminium mass flux from the mass flux given by the crystal. This results in the extra deposited oxygen mass flux F_{O2} which we have used as y axis. The least squares optimized value of F_{Al} is used as the x axis. The dotted lines in fig. 4 are the predictions of the model for the two pressures. The least squares optimized value of $\alpha = 1.93$ which compares well with the theoretical value 1.88. The least squares optimized value of $\beta = 1.3\mathrm{x}10^{-4}$ kg/m^{2}s Pa. This value can be used to derive a sticking coefficient s for the oxygen on the granular aluminium. The obtained value for the sticking coefficient is $s = 0.09$ which shows that the predicted value for β is reasonable.

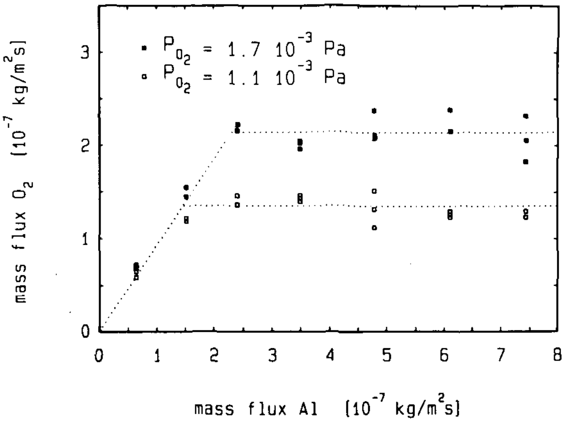

fig.4 Mass flux of oxygen versus the mass flux of aluminium. The dotted line shows the least squares optimized prediction of the model with $\alpha = 1.93$ and $\beta = 1.3 \times 10^{-4}$ kg/m^{2}sPa.

The model for the incorporation of oxygen in the aluminium gives a good description for the data of the quartz crystal rate monitor. A more advanced model is needed in the cross over region of the complete oxidation of aluminium to aluminium oxide. However, with the present data this oxidation model can be applied. As the maximum incorporation is limited by the formation of aluminium oxide, it is very likely that the oxygen is incorporated in the granular aluminium in the aluminium oxide phase.

OXYGEN CONCENTRATIONS

To investigate the influence of the oxygen concentration in granular aluminium on the resistivity, we determined the oxygen concentration of four different compositions. The resistivity of these four composition is measured as a function of temperature. The results are shown in fig.1. One composition is in the insulating regime. Electrical measurements on this composition are reported elsewhere. [4] The other three compositions are in the metallic regime. The oxygen concentrations of the electrically characterized compositions are measured with four different techniques.

A) Oxidation model.

The oxygen concentration can be determined with the oxidation model derived from the data of the quartz crystal rate monitor. The two parameters are the mass spectrometer output current and the oxygen pressure during evaporation. The pressure during all four evaporations was 1.1×10^{-3} Pa.

B| Electron probe micro analysis (EPMA).

A microprobe is used for the measurements of the oxygen concentration. The amount of characteristic aluminium X-ray radiation is measured from the granular aluminium layers. These values are compared with the amount of radiation from a reference layer of pure aluminium with equal thickness. An aluminium concentration for the granular aluminium layers is derived from the ratio of the radiation of the layer and the reference layer.

C| Anodization.

Anodization can be used for a controlled oxidation of aluminum. The charge necessary to oxidize the aluminium is used to obtain the oxygen concentration. The layers are anodized with a constant current source in a solution of 3 % H_3PO_4 in H_2O, which is adjusted to a pH= 7 with KOH [9], with a cathode made of carbon. The anodized area was defined with photoresist. The current density was 0.95 mA/cm^2. The voltage V(t) across the anodized layer and the derivative dV(t)/dt are monitored during the anodization process. The anodization process measures the oxidation of aluminium in the layers as a function of the depth. The depth resolution gives the possibility of detecting gross inhomogeneities in the evaporation direction.

To relate the amount of charge passing through the layers with the aluminium concentration, the charge must be completely used to oxidize the aluminium to the trivalent state with no trapped charge in the oxidized layer. The latter two assumptions have been verified. [5] However, not all the charge is used to oxidize aluminium. Part of the charge is used to liberate oxygen at the surface of the oxidized layer. This coulombic efficiency η is close to a 100 % for voltages below 15 -20 V and decreases at higher voltages.[5] The thickness of aluminium oxide formed for every volt across the layer, stays constant during the growth with a value of 1.38 ± 0.03 nm/V, according to the same study of the anodization properties. The voltage versus time traces monitored during the anodization of the four granular aluminium layers and a reference layer of pure aluminium are shown in fig. 5. If the coulombic efficiency is constant, the V(t) curves will be straight lines. The small curvature in fig. 5 can be explained by a drop in coulombic efficiency, since a similar curvature is observed in the anodization of pure aluminium. This makes the explanation of the curvature being caused by inhomogeneity in the layers of granular aluminium not very likely.

The method we have used to obtain the oxygen concentration of the layers is determined from the derivative of the anodization curve for granular aluminium and the anodization curve for pure aluminium.. The oxygen mass concentration can be obtained with the relation:

$$n = \frac{3M_O}{3M_O + 2M_{Al}\frac{a}{a-1}} = \frac{8}{8 + 9\frac{a}{a-1}} \qquad (1)$$

$$a = \frac{(dV(t)/dt)_{gral}}{(dV(t)/dt)_{al}} \qquad (1a)$$

with M_O is the mass of an oxygen atom and M_{Al} is the mass of an aluminium atom.

This relation is obtained with the following assumptions: (1) There are no leakage currents. (2) The number of aluminium atoms relate to the current as $N_{Al} = (\eta I t) / (3 e)$, with η is the coulombic efficiency, I is the current and t is the time. Equation (1) is independent of the coulombic efficiency. If this efficiency is dependent of the thickness of the anodized layer of aluminium oxide, equation (1) can still be applied if the derivative is taken at equal voltages for the granular aluminium layer and the aluminium layer. The measured derivatives during the anodization are shown in fig. 5. The oxygen concentration as a function of the depth can be obtained with equation (1), but the V(t) curves should be deconvoluted with the depth resolution of the anodization process.

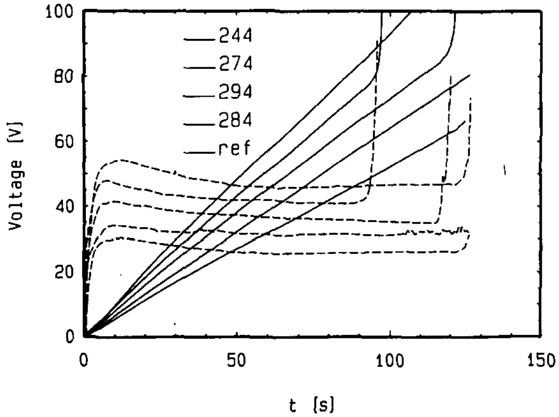

fig.5 The voltage versus time traces during the anodization of the four granular aluminium compositions and a reference layer of pure alumnium. The dotted lines are the derivatives. The samples were anodized with a current density J= 0.95 mA/cm^2. The top curve is sample 244. The bottom curve is the reference layer of aluminium.

DI RBS.

The aluminium and oxygen concentration are obtained by Rutherford back scattering experiments. The substrate on which the layers are grown is single crystalline aluminium oxide (sapphire). The granular aluminium composition can be compared with the substrate composition, which serves as a reference for pure aluminium oxide. This experiment is capable of detecting accurately the deviations of the composition of granular aluminium from pure aluminium oxide.

Table I

sample	ρ 4.2 K Ωcm	mass spectrometer current pA	output X-tal nm/s	Oxygen mass concentration n [%]				
				oxidation model		anodization	EPMA	RBS
				pressure Pa				
				1.1 10e-3	0.37 10e-3			
244	40	1.38	0.075	47	29.5	28		30.0 ±1
274	2.0 e-2	1.57	0.091	47	26.7	25	29	26.5 ±1
284	1.0 e-4	2.72	0.13	35	16.4	14	21	17.5 ±1
294	5.5 e-4	2.02	0.11	43	21.5	21	24	19.5 ±1

Table I Data of the four compositions used for the oxygen concentration measurements. The partial oxygen pressure during the evaporation was $1.1x10^{-3}$ Pa. The mass spectrometer was calibrated versus the ion gauge before every evaporation. The differences were always beneath 5 %. The ion gauge was used as the reference during this research. The reference aluminium rate and the reference oxygen pressure for the feedback loops were adjusted according to this calibration constant. The density programmed on the X-tal rate monitor was $2.7x10^3$ kg/m^3. The oxidation model has the oxygen pressure as a parameter. The results in one column assumes equal pressures between X-tal and substrates position while the results in the other column assumes a lower pressure at the substrate position. The value of this pressure is optimized to the oxygen concentrations obtained from the RBS measurements

The results of the oxygen measurements of the four compositions are summarized in table I. The oxygen concentrations, obtained from the oxidation model, are much to high when these results are compared with the other methods. A difference in oxygen flux between the substrate position and the quartz sensor position must be assumed. A real difference in this flux could exist in our system (fig.2), because of the position of the oxygen inlet valve relative to the substrate. The oxygen should be sprayed directly on the substrates and the quartz crystal. An additional advantage will be a reduction of the correlated behavior of the fluctuations between the aluminium rate and the oxygen pressure. To obtain a better correspondence between the oxygen concentration of the oxidation model and the other methods, a new pressure is calculated. The value is obtained by least squares fitting between the RBS data and the pressure in the oxidation model. These results are also shown in Table I. If the model is correct it will provide also information about the oxygen concentration in the granular aluminium and the fabrication parameters. The parameters are the aluminium evaporation rate and the oxygen pressure.

The anodization, the RBS and the EPMA show all similar results for the oxygen concentration measurements. The RBS data is probably the most reliable and accurate. It is difficult to determine the oxygen concentration with an EPMA. The EPMA concentration measurements are based on the ratio the intensities of aluminium characteristic X-rays between the granular aluminium layer and a pure aluminium layer. The oxygen concentration of granular aluminium has been reported at a composition at the metal insulator transition. [6] The measurement was performed with RBS. The result was a mass concentration of 32.7 %. This value is higher than we observe with the same technique in sample 244 which is in the insulating regime.

CALCULATED RESISTIVITIES

The resistivity as a function of the oxygen concentration has been calculated with percolation models of the microstructure of granular aluminium. The models are only intended to obtain an estimate for the dependence of the resistivity on the oxygen concentration and not to obtain the resistivity as a function of temperature, since the models do not contain localization effects nor electron electron interactions. The calculated resistivities will only be reasonable estimates for temperatures high enough to neglect these effects. To calculate the resistivity of granular aluminium, a model for the microstructure must be specified. The microstructure has been suggested being randomly closed packed [7] with grains of approximately 3 nm with a relatively narrow size distribution. [1] In the following calculations the grain size distribution is ignored and the size is kept constant at a value of 3nm.

The first model of the microstructure we used for the calculations, is a site percolation model on a simple cubic (sc) lattice and a face centered cubic (fcc) lattice. The lattices were filled with spheres with an occupation probability. The resistance between two neighboring sites is a scaling factor in the model. In both lattices we used a value for the site to site resistance to obtain the resistivity of pure aluminium at highest possible aluminium concentration in the model. The use of fcc and sc lattices near the metal insulator transition instead of the randomly packed structure of granular aluminium has been discussed. [7] The resistivity is calculated with a computer for a lattice with a 1000 points (10x10x10) for different occupation probabilities. The oxygen concentration is calculated from the occupation probability, with the assumption that the unpacked fraction is filled with aluminium oxide. The percolation threshold oxygen concentrations are: 0.39 ±0.02 (sc) and 0.40±0.02 (fcc) in agreement with earlier calculations. [8]

The second model of the structure uses 'grains' coated with aluminium oxide. The 'grains' are cubes on a simple cubic lattice or rhombic dodecahedrons on a face centered cubic lattice. These 'grains' are connected by tunnel barriers of aluminium oxide with a barrier height of 2 eV. [9,10] The barrier thickness *d* is a random variable with a uniform distribution. This is a bond percolation model. The resistivity is calculated as a function of the barrier thickness *d*. Several standard deviations have been used for the barrier thickness distribution. The oxygen concentration is obtained by calculating the oxygen necessary to sustain the average oxide coatings on the grains. This model has an obvious metal insulator transition when the aluminium is completely oxidized.

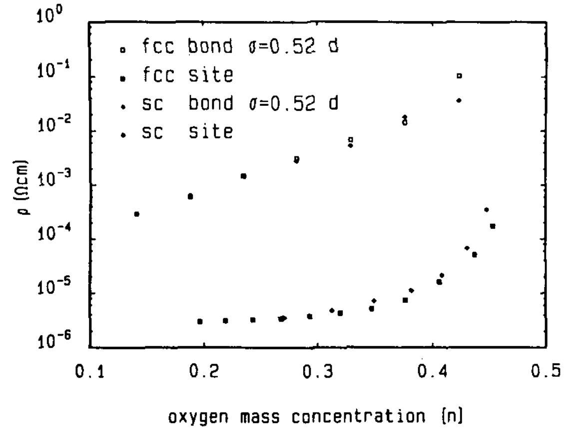

fig.6 Resistivity of 10x10x10 site and bond percolation networks for two different 3D lattices as a function of the oxygen mass fraction n. Threshold concentrations are (sc) 0.39±0.02 and (fcc) 0.40±0.02

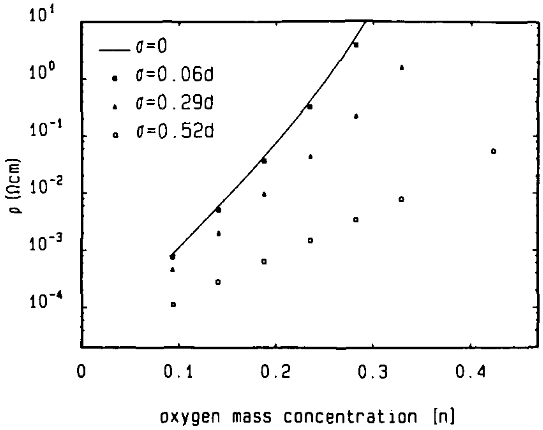

fig.7 Resistivity of 10x10x10 simple cubic bond percolation networks for three different standard deviations σ of the barrier thickness distribution. The thickness d corresponds to the barrier thickness necessary to sustain a lattice with a mass fraction oxygen n. The solid line corresponds to the exact solution of the model.

The results of the calculations on both models are shown in fig.6. As is observed, the bond percolation model shows a much higher resistivity at equal oxygen concentrations. The influence of the standard deviation of the barrier thickness distribution is shown in fig.7. A large decrease in resistivity is observed when the standard deviation is increased.

The calculated resistivity as a function of the oxygen concentration can be compared to the measured resistivity at several oxygen concentrations. The metal insulator transition occurs at a much lower oxygen concentration compared to the site percolation calculations. The higher metal concentration at the metal insulator transition is usually observed in granular mixtures (thin insulating coatings around metallic grains). [11,12] The order of magnitude of the resistivity shows also a large discrepancy be. To obtain a better correspondence we drop the assumption of a geometrical isotropic material. If an asymmetry is suggested in the microstructure, a better correspondence will be obtained between the measured and calculated data. The asymmetry can be caused by a difference in the microstructure in the direction of growth of the layer compared to the structure in the plane of growth. The average thickness of the oxide coatings around the grains cold differ in both directions. An asymmetry in the microstructure of granular aluminium has been suggested by measurements of the temperature and angular dependence of the critical field. [13] We have observed a difference in the resistivity which was measured parallel and perpendicular to an evaporated layer of granular aluminium (These measurements were performed on samples 244.). [4] Both results suggest an asymmetry in the microstructure.

The critical site percolation probability in three dimensions for several lattices correspond all to the same critical probability density of ≈ 0.15. In two dimensions this value is ≈ 0.44. [14] The critical percolation densities have been expressed, for clarity, in the critical mass concentration of oxygen in fig. 8. We have assumed for the calculations of the critical mass concentration of oxygen that the oxygen is only present in the aluminium oxide phase. The shaded transition areas represent the uncertainty in the calculated critical percolation probability as well as the density of amorphous aluminium oxide. The metal insulator transition in the preceding calculations of site percolation models of the microstructure are in agreement with this general result in three dimensions. A qualitative better correspondence will be obtained when the average thickness of the oxide coating is larger in the direction of growth. The metal to insulator transition will shift to a lower oxygen concentration with an increased conductivity parallel to the layers at lower oxygen concentrations. A qualitative understanding of the properties of granular aluminium can be obtained with a site percolation model with a smaller bonding probability in one direction (The direction of growth.). This model will show a three dimensional behavior, but will probably before it becomes insulating show a two dimensional behavior. In this composition range the structure consists of layers with a correlation length. The structure will go from three dimensional to weakly coupled layers. The layers could decouple completely in a narrow composition range. When the material becomes insulating, the percolation clusters will have a smaller average size in the direction of growth. With this simple asymmetry added to the microstructure model many of the properties of granular aluminium can be qualitative better understood.

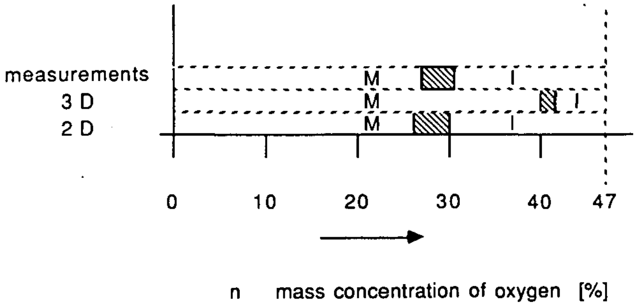

fig.8 Critical oxygen mass concentrations for site percolation at the metal insulator transition in two and three dimensions. These concentrations are compared with the measured results.

CONCLUSIONS

We have measured the oxygen incorporation and oxygen concentration of granular aluminium. Based on these measurements we have two major conclusions.

First, the fabrication of the material is very critical. For the fabrication of materials near the metal insulator transition a very homogeneous concentration of the constituents is always crucial. This work shows that this also applies for granular aluminium. In table I it is observed that the resistivity range from 1×10^{-4} to 40 Ωcm is spanned by only a factor of two in deposition rate. An extra complication for the fabrication of granular aluminium is the correlated behavior between oxygen pressure and aluminium rate. If an electron gun is applied for the evaporation, a high quality rate control system will be essential.

Second,the measured and calculated oxygen concentration versus resistivity shows a not satisfactory agreement. If the model for the microstructure of granular aluminium in the investigated resistivity range is extended with an asymmetry, a better correspondence will be obtained between calculated and measured oxygen concentrations.

Acknowledgment. This work is supported by the foundation for Fundamental Research on Matter (F.O.M.). We would also like to thank Dr H. de Rugy and Mr P. Saliot of ISA Riber for performing the RBS measurements and Dr D. Schalkoord for performing the EPMA measurements.

REFERENCES

1 G. Deutscher, H. Fenichel, M. Gershenson, E. Grünbaum and Z. Ovadyahu, J. Low Temp. Phys.**10**, 231, (1973)

2 A.J.G. Schellingerhout, M.A. Janocko, T.M. Klapwijk and J. E. Mooij, (submitted to Review of Scientific Instruments)

3 J.E. Crowell, J.G. Chen and J.T. Yates Jr, Surface sci **165**, 37, (1986)

4 A.J.G. Schellingerhout, H.M. Appelboom, J.A. Kokkedee, J.E. Mooij and T.M. Klapwijk, (to be submitted to Phys Rev B)

5 R.C. Plumb, J.E. Lewis, J. Electroch Soc, **105**, 496, (1958)

6 M. Kunchur, P. Lindenfeld, W.L. McLean and J.S. Brooks, Phys Rev Lett **59** , 1232, (1987)

7 G. Deutscher, O. Entin-Wohlman, S. Fishman and Y. Shapira, Phys. Rev. B **21**, 5041, (1980)

8 S. Kirkpatrick, Rev. Mod. Phys .**45**, 574, (1973)

9 D. McBride, G. Rochlin and P. Hansma, J. Appl. Phys. **45**, 2305, (1974)

10 R. Meservey, P.M. Tedrow and J.S. Brooks, J. Appl. Phys. **53**, 1563, (1982)

11 G. Deutscher, M. Rappaport and Z. Ovadyahu, Solid Stat Comm **28**, 593, (1978)

12 B. Abeles, H.L. Pinch and J.I. Gittleman, Phys Rev Lett **35** , 247, (1975)

13 S.A. Dodds, S.N. Harrington, R.S. Newrock and K. Loeffler, Phys. Rev. B **33**, 3115, (1986)

14 H. Scher and R. Zallen, J.Chem.Phys **53**, 3759, (1970)

CHAPTER 7

STRONG ELECTRIC FIELD EFFECT IN GRANULAR ALUMINIUM

A.J.G. Schellingerhout, H.M. Appelboom, J.A. Kokkedee, J.E. Mooij and T.M. Klapwijk*

Department of Applied Physics, Delft University of Technology, Delft,

The Netherlands

*Department of Applied Physics, University of Groningen, Groningen,

The Netherlands

ABSTRACT

A strong electric field dependence of the resistivity is observed in insulating granular aluminium. This field dependence is described by the relation $R= R_E\ exp((E_o/E)^{0.5})$. The resistance of the granular aluminium has been measured parallel and perpendicular to the evaporated layers. In the perpendicular geometry the non linear resistance has been observed over six orders of magnitude. The resistivity parallel and perpendicular shows an unexplained difference. Two models for electric field effects have been used to interpret the measurements. They are an existing model for electric field effects in granular metals and a variable range hopping model with a coulomb gap which has been extended with the electric field dependence. The variable range hopping model shows the observed square root dependence of the electric field. The application of variable range hopping to granular aluminium is discussed.

The metal insulator transition (MI) in 3-dimensions has been a topic of considerable interest in recent years.[1-5] Granular aluminium shows a MI-transition when the oxygen to aluminium ratio is changed.[6] We have investigated the dependence of the resistance of granular aluminium as a function of the electric field. The resistance has been measured perpendicular to the evaporated layers (junction geometry) and has also been measured parallel to the evaporated layer (the reference layer). Both samples are evaporated during the same evaporation run to assure an identical composition of the granular aluminium in both layers. The junction geometry allows to measure the electric field effect over a wide range of resistance values. Prior measurements of the electric field effect have been reported.[7] In this paper we have extended the temperature range of the measurements with a dilution refrigerator, confirmed that the observed non linearity is caused by an electric field effect, and compared the measurements with the predictions for the electric field effect of two theoretical models which have been suggested to explain the temperature dependence of the resistivity of granular aluminium. The variable range hopping model with a coulomb gap shows the observed $R= R_E \exp((E_o/E)^{0.5})$ dependence of the electric field.

The measurements perpendicular to the granular aluminium are performed by sandwiching the layer between two well conducting aluminium layers. Both contact layers consist out of a pure aluminium layer for a low spreading resistance and a granular aluminium layer with a $\rho_{4.2\ K}$ of about 10^{-5} Ωcm to increase the super conducting critical temperature. Thus the multilayer consists out of five layers in which the third layer has the composition near the MI-transition. The junction geometry is fabricated out of the multilayer by selective anodization of the aluminium.[8] The electrolyte is a solution of KOH and H_3PO_4 adjusted to a pH of 7. The area of the junctions are 8 x 8 μm^2 and 16 x 16 μm^2 . The granular aluminium is fabricated in an UHV system by evaporation on sapphire substrates at room temperature. The aluminium flux and the partial pressure of oxygen are measured simultaneously with a mass spectrometer and are both controlled by two feedback systems. The output voltage of the aluminium rate signal shows a rms noise of 0.5 % (band width= 1 Hz). The substrate to source distance is 60 cm while the sensor to source distance is 76 cm. The multilayers are fabricated in one continuous evaporation run by changing the reference signals to the feed back loops. These reference signals are generated with a computer. The output signals of the mass spectrometer during a similar evaporation run are shown in fig.0a. The Rutherford backscatter spectrum of the multilayer is shown in fig.0b. During the deposition of the 100 nm thick layer with a composition near the MI transition, an auxiliary shutter is opened to evaporate the reference layer on a different substrate. The distance between the substrates for the reference layer and the junction is 2 cm. The deposition conditions during the opening of the auxiliary shutter are an oxygen pressure of p_{O2}= $1.1x10^{-3}$ Pa and an aluminium rate of 0.041 nm/s. The rate is obtained by calibration against a quartz crystal with no oxygen present. The partial pressure of oxygen is obtained by calibration of the mass spectrometer output to an ion gauge output before the evaporation of aluminium. During the evaporation run the calibration constant changes because the pumping speed for oxygen is very much increased by the evaporation of aluminium. This change is observable in fig.0a. Both outputs show a strong correlation, but with a different aluminium rate there is a change in the calibration constant. The mass spectrometer is used for the oxygen pressure signal because it is closest to the substrates.

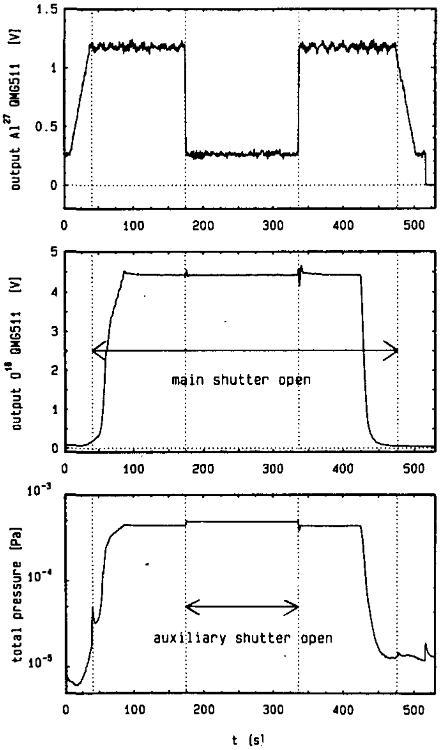

Fig.0a Evaporation sequence for a multilayer (This sample has a thinner layer with a composition near the MI-transition.).The mass spectrometer (Balzers QMG511) is multiplexing (8 ms) between O^{16} and Al^{27}. The multilayer for the junction geometry is deposited during the opening of the main shutter. The reference layer is deposited during the opening of the auxiliary shutter. The output of an ion gauge is simultaneously monitored. The calibration constant between the pressure reading of the iongauge and the mass spectrometer output changes at different evaporation rates of aluminium.

If the aluminium rate is zero, the ion gauge reading will be $1.1x10^{-3}$ Pa. The large noise in the aluminium rate is caused by aliasing of high frequency noise by the very low sample frequency (1.5Hz) of the measurement apparatus.

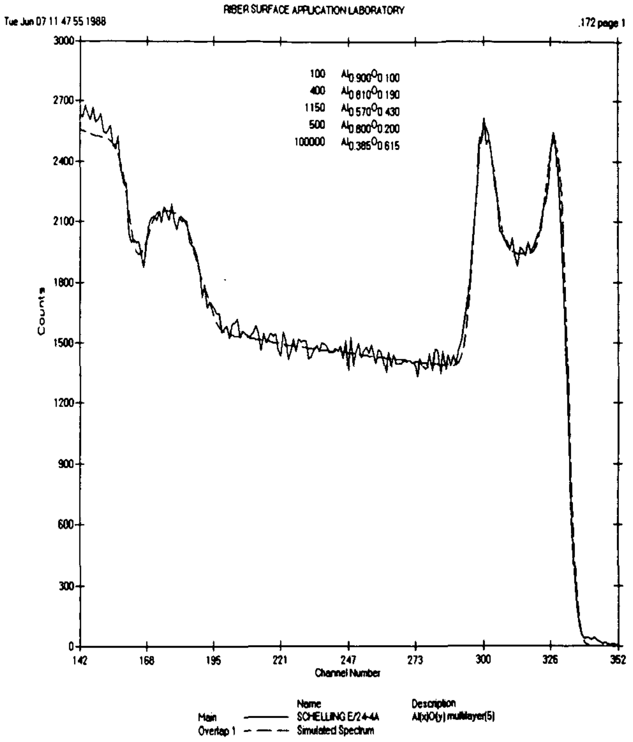

Fig.0b Rutherford backscatter spectrum of the fabricated multilayer. The surface edge energy of oxygen is 0.73 MeV, channel 196. The surface edge energy of aluminium is 1.10 MeV, channel 333. The aluminium and oxygen concentrations for the evaporated multilayer are shown in the insert. The thickness is given in Å.

The resistance of the reference layer and the junction has been measured. Both geometries show at low voltages a resistance independent of the voltage. In this linear regime the resistances can be compared with the known resistance versus temperature relations of granular aluminium. The junction and the reference layer show the same temperature dependence of the resistance with the relation $R=R_T exp\ ((T_o/T)^{0.5})$.[9] This implies insulating granular aluminium. The reference layer has a $T_o = 220$ K. The resistivity $\rho_{4.2\ K}$ is 40 Ωcm which is in agreement with the experimental value of T_o.[10] The resistance measurements perpendicular to the layer in the junction geometry results in an identical value for T_o, but the resistivity is higher: $\rho_{4.2\ K}$= 400 Ωcm. This is a remarkable result. We do not believe this is caused by inhomogeneity of the sample caused by the evaporation process.

In principle measuring perpendicular and parallel to a layer is an important test for homogeneity, but it is unlikely that an inhomogeneity caused by the evaporation process would result in an identical T_0. It is also unlikely that the difference in resistivity is caused by a difference in real junction area and the measured junction area, since we have two closed spaced junctions with an area four times larger. Both junctions gave an identical resistivity. A possible explanation is an asymmetry in the microstructure of granular aluminum. This has been suggested in relation to measurements of superconducting critical fields.[11] In the following the prefactors will be ignored and only the constants in the exponents will be used.

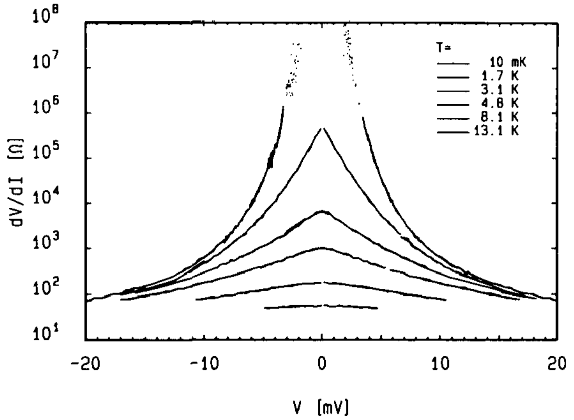

Fig.1 Derivative dV/dI on a logarithmic scale versus the voltage for a sample in the junction geometry. The top curve is measured at 10 mK. The bottom curve is measured at 13.1 K.

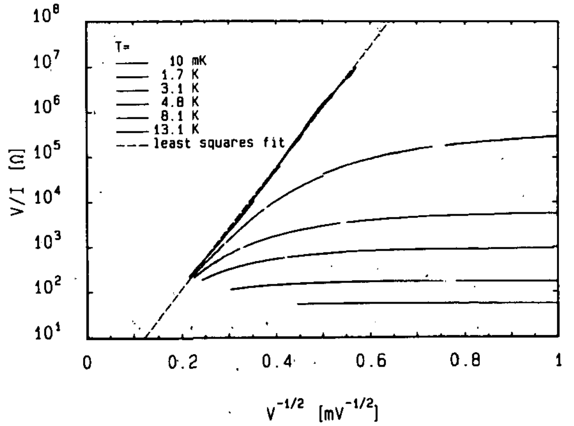

Fig.2 Resistance of a junction versus the voltage. The extra line is a least squares fit to $R = R_E \exp((V_0/V)^{0.5})$*.The top curve is measured at 10 mK. The bottom curve is measured at 13.1 K.*

A non linear behavior was observed when the voltage across the junction was increased above a few millivolts. Figure 1 shows the derivative dV/dI on a logarithmic scale versus the voltage across the junction. All curves converge at high voltage to the same value which indicates that the conduction becomes temperature independent. The resistance versus voltage at 10 mK can be fitted to the relation $R=R_E exp((V_o/V)^{0.5})$. The curves are shown in fig.2. At low temperature and low voltage extra noise is observed reminiscent of the random telegraph noise[12] but with a much larger amplitude. In fig.3 the V(I)-characteristic at 100 mK is shown. The insert shows the switching of the current at a constant bias voltage. The resistance of the reference layer shows the non linearity with an identical voltage dependence. Only the voltage has to be scaled with the ratio of both lengths. This scaling behavior implies that the observed curvature is caused by an electric field effect and that the curvature is not caused by the small dimensions in the junction geometry. In fig.4 the V(I)-characteristics of the junction and the reference layer are plotted. They have been scaled with their length ratio, but no fitting has been involved. To exclude the possibility of heating of the sample with respect to the substrate, we calculated the heating contribution. This model uses the temperature relation for the resistance $R=R_T exp((T_o/T)^{0.5})$: a thermal boundary resistance $R_k=C/T^3$ and a current source for the resistance measurement. According to the calculations, the curvature can not be explained by heating of the film with respect to the substrate.

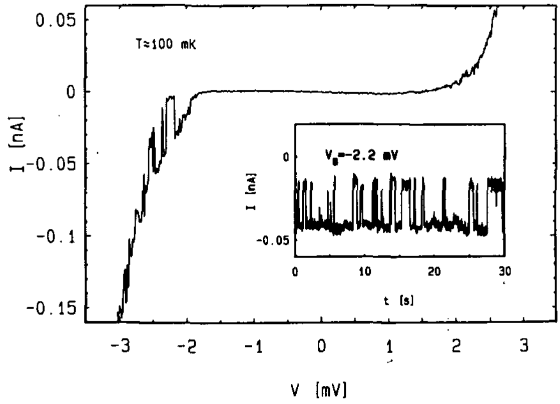

Fig.3 V(I)-characteristic of a junction at 100 mK. The insert shows the current switching versus time at a constant bias voltage

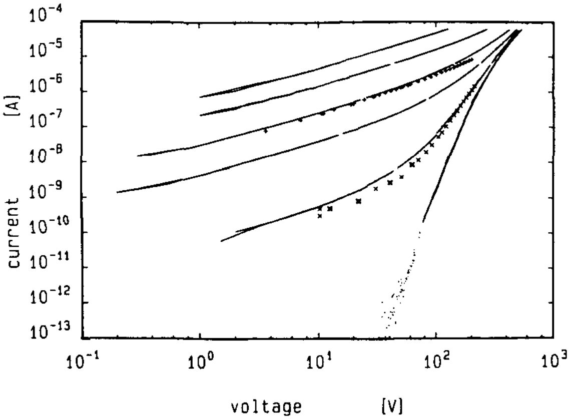

Fig.4 V(I)-characteristics of the reference layer (crosses= 1.2 K, plusses= 4.2 K).The junction results are also plotted. They are scaled with the length ratio (2.5x10^4) and the resistivity ratio. The top curve is measured at 13.1 K. The bottom curve is measured at 10 mK.

Electric field effects have been observed in granular metal systems.[13] [14] The model for the explanation of the field effect is based on metallic grains embedded in an insulating matrix. The grains in the matrix follow the relation $E_c.d=$ const, in which E_c is the charging energy of the grains and d is the distance between the grains. This model predicts a temperature dependence $R=R_T exp\ ((T_o/T)^{0.5})$ and an electric field dependence $R=R_E\ exp(E_o/E)$. These predictions were in agreement with experimental results in granular Ni-SiO_2 films.[13] [14] This model does not describe our present results. First, it does not predict the right exponent for the electric field effect, since we observe a best fit for the high field conduction with the relation $R=R_E\ exp((E_o/E)^{0.5})$. Second, if we force our measurements to fit the $exp(E_o/E)$ behavior the calculated grain size will be about 10 nm at 1.66 K. This value is inconsistent with the grain size of granular aluminium observed by electron microscopy.[15] The applicability of this model to granular aluminium has also been questioned on the basis of structural grain size distributions.[9]

Electric field effects are predicted in variable range hopping conduction. [16-18] These non linear effects are observed in several systems.[19] [20] A variable range hopping model with a coulomb gap results in a low field dependence $R=R_T exp\ ((T_o/T)^{0.5})$.[21] This conduction mechanism has been suggested for granular aluminium,[9] based on the observed $exp\ ((T_o/T)^{0.5})$ dependence. We have to extend the variable range hopping model with a coulomb gap to obtain the high field dependence of the conduction. The density of states $g(\ \varepsilon)= \alpha(\ \varepsilon\text{-}\mu)^2\ \kappa^3/e^6$ is obtained with a simple derivation for the coulomb gap.[22] (κ=dielectric constant μ=Fermi level and α=constant.) This results in a low field temperature dependence $R=R_T exp$

$((T_o/T)^{0.5})$ with $T_o = \beta e^2/\kappa a_l k_B$ and the hopping length $L_T \approx a_l(T_o/T)^{0.5}$ in which a_l is the localization radius and β is a constant .[22] To obtain the high field resistance dependence, we follow the arguments of Shklovskii [23] which are based on making a new effective density of states caused by the electric field energy eEL_E. This results in a high field dependence $I(E) \propto \exp(-(E_o/E)^{0.5})$ with $E_o = 4\,(3/\alpha)^{1/3} e/\kappa a_l^{\,2}$ and the hopping length $L_E \approx (e/E\ \kappa)^{0.5}$. The high field dependence of the resistance is identical to what we observe in the granular aluminium. The microscopic variables a_l and κ have been calculated with the measured value of $E_0 = 1.10^7$ V/m and $T_0 = 220$ K. The values obtained are $a_l = 4$ nm and $\kappa = 6.10^{-9}$. An estimate for the coulomb gap Δ is 24 meV.[22] For temperatures lower than 350 mK and electric fields smaller than 3×10^3 V/m, both hopping lengths L_T and L_E are larger than 100 nm. This implies a larger hopping distance than the thickness of the layer in the junction geometry, which could lead to the large noise observed in the junction observed in fig. 3.

The application of the concept of the coulomb gap to granular metals is not completely clear. Arguments are made in favour of as well as against the application. [24-26] If scaling theory [27] is applied to granular metals, with the grain size as characteristic length scale, a reasonable estimate will be obtained for the critical conductivity at the Anderson transition.[28] [29] The length scale near the MI-transition diverges which causes a screening out of the coulomb energy on the scale of a single grain in the metallic regime.[30] In the insulating regime the localization radius diverges and becomes larger than an individual grain which opens the possibility of applying variable range hopping. In our samples we measure a localization radius of 4 nm which is larger than an individual grain. Closer to the MI-transition localization radii of 20 nm have been inferred from magnetoresistance measurements.[10] The large dielectric constant κ shows the strong screening of the coulomb interaction near the MI-transition.[31,3] A high dielectric constant can also be expected in a classical approximation for insulating granular metals.[14] Farther away from the MI-transition in the insulating regime the models which are based on individual grains are expected to be valid as is the case in Ni-SiO_2.[14]

In summary, we have observed a strong electric field dependence in insulating granular aluminium. The measurements are interpreted with a variable range hopping model with a coulomb gap.

Acknowledgment. This work is supported by the Foundation for Fundamental Research on Matter (F.O.M.).

REFERENCES

1 W.L. McMillan and J. Mochel, Phys. Rev. Lett. **46**, 556 (1981)

2 G. Hertel, D.J. Bishop, E.G. Spencer, J.M. Rowell and R.C. Dynes, Phys. Rev. Lett. **50**, 743 (1983)

3 M.A. Paalanen, T.F. Rosenbaum, G.A. Thomas and R.N.Bhatt, Phys. Rev. Lett. **51**, 1896 (1983)

4 Anderson Localization edited by T. Ando and H. Fukuyama (Springer-Verlag Berlin Heidelberg 1988)

5 M. Kunchur, P. Lindenfeld, W.L. McLean and J.S. Brooks, Phys. Rev. Lett **59**, 1232 (1987)

6 R.C. Dynes and J.P. Garno,Phys. Rev. Lett **46**, 137 (1981)

7 A.J.G. Schellingerhout, H.M. Appelboom, J.A. Kokkedee, J.E. Mooij and T.M. Klapwijk, in Anderson Localization edited by T. Ando and H. Fukuyama (Springer-Verlag Berlin Heidelberg 1988)

8 H. Kroger, L.N. Smith and D.W. Jillie, Appl. Phys. Lett. **39**, 280 (1981)

9 T. Chui, G. Deutscher, P. Lindenfeld and W.L. McLean, Phys. Rev. B **23**, 6172 (1981)

10 H.K. Sin, P. Lindenfeld and W.L. McLean, Phys. Rev B **30**, 4067 (1984)

11 S.A. Dodds, S.N. Harrington, R.S. Newrock and K. Loeffler, Phys. Rev. B **33**, 3115 (1986)

12 E.K. Track and D.E. Prober, in proceedings of LT 18 Kyoto 1987 Japanese J. of Appl. Phys. **26** , 1635 (1987) suppl 26-3

13 P. Sheng, B. Abeles and Y. Arie, Phys. Rev. Lett. **31**, 44 (1973)

14 B. Abeles, P. Sheng, M.D. Coutts and Y. Arie, Adv. Phys. **24**, 407 (1975)

15 G. Deutscher, H. Fenichel, M. Gershenson, E. Grünbaum, and Z. Ovadyahu, J. Low Temp. Phys. **10**, 231 (1973)

16 M. Pollak and I Riess, J. Phys C **9**, 2339 (1976)

17 N. Apsley and H.P. Hughes, Phil. Mag. **30**, 963 (1974)

18 N. Apsley and H.P. Hughes, Phil. Mag. **31**, 1327 (1975)

19 N. Apsley, E.A. Davis, A.P. Troup and A.D. Yoffe, in Proceedings of the 7th international conference on amorphous and liquid semiconductors in Edinburgh (1977) p.447

20 A.N. Ionov, M.N. Matveev, I.S. Slhimak and R. Rentch, JETP Lett **45**, 310 (1987)

21 A.L. Efros, J. Phys. C **9**, 2021 (1976)

22 A.L. Efros and B.I. Shklovskii, in Electron-electron interactions in disordered systems (North Holland, Amsterdam, 1985) p.409

23 B.I. Shklovskii, Soviet Phys Semi **6**, 1964 (1973)

24 E. Simanek, Solid State Commun. **40**, 1021 (1981

25 B.I. Shklovskii and A.L. Efros, Electronic Properties of Doped Semiconductors, Springer (1984)

26 O. Entin-Wohlman, Y. Gefen and Y. Shapira, J.Phys. **C16**, 1161 (1983)

27 E. Abrahams, P.W. Anderson, D.C. Licciardello, and T.V. Ramakrishnan, Phys. Rev. Lett. **42**, 673 (1979)

28 Y. Imry, Phys. Rev. B **24**, 1107 (1981)

29 C. van Haesendonck and Y. Bruynseraede, Proc. LITPIM Suppl. (PTB-PG-1), pp 279 (PTB Braunschweig, 1984)

30 Y. Imry and M.Strongin, Phys. Rev. B **24**, 6353 (1981)

31 Y. Imry and Y. Gefen, Phil Mag B **50**,203 (1984)

CHAPTER 8

ANALYSIS OF $Y_1Ba_2Cu_3O_{7-Y}$ THIN FILMS ON SAPPHIRE SUBSTRATES MADE BY ELECTRON BEAM EVAPORATION.

A.J.G. Schellingerhout, R.H.M. van de Leur, D. Schalkoord, D. van der Marel and J.E. Mooij

Department of Applied Physics, Delft University of Technology, Lorentzweg 1,
2628 CJ Delft, The Netherlands.

ABSTRACT

We have analyzed the structure and properties of $Y_1Ba_2Cu_3O_{7-y}$ films on (012) sapphire substrates. The films were obtained by evaporation of the metals in a UHV system with an oxygen beam directed at the substrate. Analysis was performed by X-ray diffraction and electron probe microanalysis [EPMA], after annealing in addition by scanning electron microscopy [SEM] and Auger electron spectroscopy. Without annealing no superconductivity was obtained although sufficient oxygen could be incorporated during growth. The copper does not oxidize. After annealing in oxygen superconductivity is found with an onset temperature of 80-90 K and zero resistance at 30-40 K. A grain-like pattern of 3-5 μm typical size is seen. Chemical reactions between layer and substrate are observed.

INTRODUCTION

After the discovery of Bednorz and Müller [1] of superconductivity at high temperatures in materials with perovskite-type structure, followed by the rapid increase of T_c observed in $Y_1Ba_2Cu_3O_{7-y}$ by Chu et al. [2], there has been an explosion in the number of publications on high T_c superconductors. The fabrication of thin films of $Y_1Ba_2Cu_3O_{7-y}$ was soon successful. The best results have been obtained on single crystal $SrTiO_3$ substrates, with films having a narrow resistive transition and a high T_c of 91 K (Chaudhari et al. [3], Naito et al. [4]). Films on sapphire have a much broader transition [4]. With e-beam evaporation no superconductivity is obtained without annealing in oxygen after the actual evaporation. As sapphire substrates are much more generally available than strontium titanate it is important to understand why the use of sapphire leads to films of much lower quality. We report on our results with $Y_1Ba_2Cu_3O_{7-y}$ films on sapphire substrates, both before and after annealing.

FABRICATION

The films were fabricated in a UHV system which is drawn in figure 1. The copper and yttrium were evaporated with two electron beam guns, the barium with an effusion cell (purity Cu 99.99%, Ba 99 % and Y 99.9%). The flux of the three metals was measured with the aid of a cross-beam mass spectrometer,which operated in a three channel time-multiplexed mode. The output of the mass spectrometer was demultiplexed and the signals used to stabilize the evaporation rate of the three metals. The aim was to make the high T_c superconductor with the composition $Y_1Ba_2Cu_3O_{7-y}$. The evaporation rate of the Ba was about 0.3 nm/s and the other rates were adjusted to obtain the ratio 1:2:3 for Y, Ba and Cu. The evaporation time was about 40 minutes for a film thickness of about 1 µm, adapted to the typical depth of analysis in normal electron probe microanalysis [EPMA] practice.

The oxygen was sprayed onto the substrates during evaporation to get locally a high effective pressure. The oxygen flow was measured to be 2 ml/min, which resulted in a system pressure before evaporation of.1.10^{-2} Pa. Five outlets were used at about 5 cm from the substrates. The oxygen flux was large enough to allow $Y_1Ba_2Cu_3O_7$ to be formed with the evaporation rate used if the oxygen were to react in the right way. The strong gettering of oxygen by Ba and Y reduced the pressure as measured with the ion gauge during evaporation to 2.10^{-4} Pa. One has to realize that the pressure reading is strongly influenced by the location of the ion gauge. The maximum oxygen flow was limited by the mass spectrometer, as its sensitivity and baseline were influenced when the system pressure was increased too much.

The system contained a heated and a non-heated substrate holder, consequently during every evaporation run we obtained films deposited at different substrate temperatures. Concentration differences due to the beam profile of the evaporating metals were small.The substrate material was (012) sapphire. No buffer layers were used.

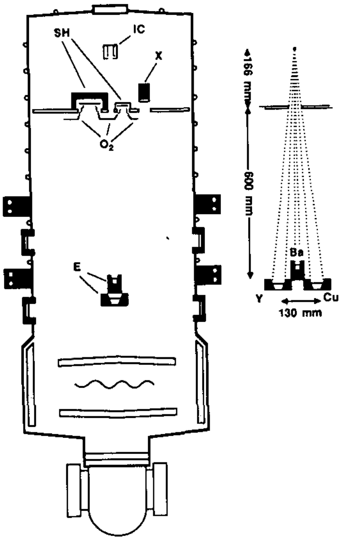

Fig. 1 Schematic drawing of the UHV-system. X= X-tal, SH = substrate holder, IC = mass spectrometer (Balzers QMG 511), E = effusion cell and e-guns, O_2 = oxygen beam.

RESULTS BEFORE ANNEALLING

The fabricated films were smooth and shiny and had a dark brown appearance. When exposed to humid air the samples slowly degraded in about halve an hour. No observable changes occurred in pure oxygen, pure carbon dioxide or pure nitrogen on the time scale of one day. The films deposited on heated substrates seemed more stable. The resistance of the films was always very high, of the order of megaohms.

Analysis of the layers was performed with an EPMA-instrument of Jeol (Superprobe 733) using an $Y_3Fe_5O_{12}$ standard for Y analysis, a K-458 glass (31.93 mass % of O_2, 23.08 mass % of Si, 3.07 mass % of Zn, 41.92 mass % of Ba) for the Ba and O analysis and pure Cu for the Cu analysis. As a reference small grains high-T_c $Y_1Ba_2Cu_3O_{7-y}$, made by powder technology, were analyzed. After application of corrections for matrix effects this analysis yielded a composition $Y_{1.0}Ba_{2.0}Cu_{3.0}O_{6.3}$.

The analysis of the films as evaporated always showed a higher oxygen concentration than needed to oxidize the Ba and Y. In some films, in particular with high substrate temperatures, we even found a higher concentration of oxygen than necessary to form $Y_1Ba_2Cu_3O_7$, so it seemed that enough oxygen was incorporated in the films during evaporation.

X-ray diffraction performed on films, evaporated with substrate temperatures from room temperature to 400 °C, indicated amorphous material with two diffuse rings. Films fabricated at temperatures between 600 °C and 800 °C showed, apart from the diffuse rings, the crystal structure of fcc Cu (figure 2). So these films contained small precipitates of pure Cu. To investigate the oxidation properties of copper we evaporated pure copper under conditions similar to those during the $Y_1Ba_2Cu_3O_{7-y}$ runs. The copper was not oxidized at room temperature, which is in agreement with measurements by Yu et al. [5]. We found we could achieve successful oxidation to CuO with a 100 eV oxygen ion beam directed at the substrate. The ion flux at the substrate was larger than the copper flux.Similar results have also been obtained by Guarnieri et al. [6].

fig.2 Wide angle Debye-Scherrer X-ray photograph, Cu radiation. The spots arise from the sapphire substrate. The X-ray photo shows the copper rings and a faint diffuse ring from an amorphous material.

The equilibrium pressure of oxygen as a function of temperature is given for CuO by Smyth and Roberts [7] and for Cu_2O by Allmand [8]. These equilibrium diagrams indicate that it is difficult to evaporate CuO or Cu_2O under vacuum conditions, as was experienced by Naito et al.[4], because the oxides dissociate when heated. Judging from the equilibrium oxygen pressure, only formation of Cu_2O is likely between 600 and 800 °C at the effective local oxygen pressure in our system. For oxidation to CuO in this temperature range a much higher oxygen pressure is required, about 10^{-1} Pa at 600 °C. The intensities of the X-ray diffraction lines for films evaporated at temperatures higher than 600 °C indicated that the major fraction of the copper in our film was not oxidized. We expect the same is true for the copper in films fabricated at temperatures below 600 °C, although metallic copper could not be observed there by X-ray diffraction. As the copper remained largely unoxidized in our films, the preparation of $Y_1Ba_2Cu_3O_{7-y}$ in the proper crystal structure seems impossible in our system. An extra anneal in oxygen at higher pressures to form the high T_c phase is necessary. The high oxygen content in our films as inferred from the EPMA data can be explained by incorporation of oxygen in the films in the form of Ba peroxides.

RESULTS AFTER ANNEALLING

After annealing in pure oxygen the films became superconducting. The typical annealing procedure was: An increase from room temperature to 800 °C in 3 hrs, 4 hrs at 800 °C, followed by a decrease to room temperature in 8 hrs.Typical resistive transitions are given in figure 3.

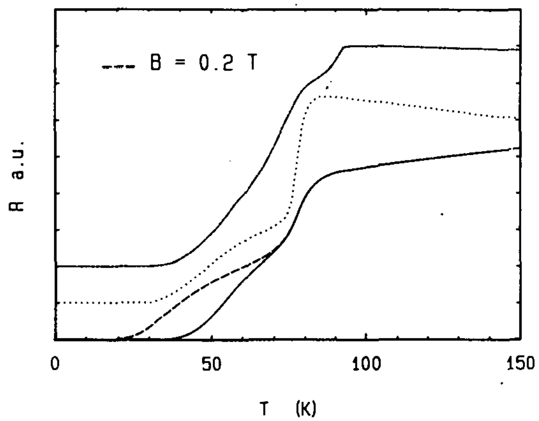

fig.3 Resistive transitions of films of $Y_1Ba_2Cu_3O_{7-y}$ *on sapphire substrates.The resistances at 150 K are 58 Ω (upper curve), 501 Ω and 25 Ω (lower curve). The dashed line is a transition in a transverse magnetic field of 0.2 T (lower curve). This field has a marked effect on the low resistance part of the resistive transition.*

The superconducting onset occurs at 80 to 90 K, but the transition width is always very broad, about 40 K. All curves have a resistive tail, which is strongly influenced by a transverse magnetic field. Positive as well as negative temperature coefficients are observed. The substrate temperature during evaporation has very little influence on the final resistive transition obtained after annealing.The films remained smooth and shiny after the annealing procedure. Figure 4 shows a secondary electron image made with a scanning electron microscope (SEM) (JEOL 840). The pattern in the layer is made by ion beam etching with Ar.

The X-ray diffraction yields the orthorhombic (high T_c) or tetragonal structure.The lines are considerable broadened, therefore the actual splitting which distinguishes between these two structures can not be observed. Preferential orientation of the small crystallites (≈ 20 nm as determined from line width) is not observed. There are always some X-ray lines which cannot be identified and hence the material is not single phase.

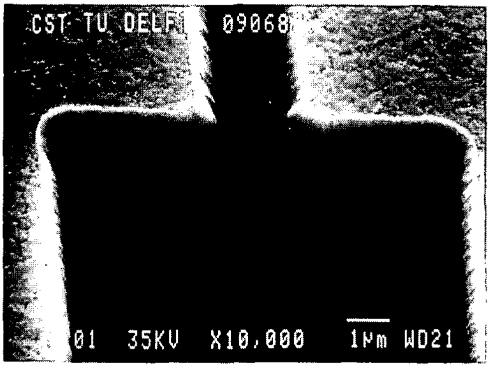

fig.4 Argon ion beam etched structure in a film of $Y_1Ba_2Cu_3O_{7-y}$ on a sapphire substrate. The bar is 1 μm. (V=35kV, substrate tilted with respect to beam).

The I-V characteristic of a narrow line of 20 μm width, made with ion beam etching, is shown in figure 5. The calculated $\rho_{225\ K}$ is 140 μΩm. A line with a width of 5 μm, etched in the same film, had a $\rho_{225\ K}$ which was 10 times higher. This line did not become superconducting, the resistance decreasing with only 30 % on cooling from 80 K to 4.2 K.

When the layers were inspected with the SEM and the backscattered electrons were used for image formation, a grain-like structure with dimensions much larger than the inferred X-ray grain size is observed in the films. Figure 6 shows a backscattered-electron image, the left side shows the grain-like structure in the film. The part on the right in this figure was etched with an Ar ion beam until 10 % of the thickness of the superconducting layer was left. The grain structure is seen to be continuous between the two halves of the figure, but the grain boundaries become thicker deeper in the film. The contrast in figure 6 between the two halves has been enhanced artificially . Figure 7 is a magnification of figure 6. The same area is given with backscattered and secondary electrons. Although the grain structure is visible in the secondary-electron image, the backscattered-electron image shows the grains more clearly. In the grain boundaries the presence of Si was detected with EPMA. In order to get an idea of the Si concentration in the boundaries Auger analysis was performed with a lateral resolution of the electron beam adapted to the dimensions of the boundaries. This resulted in an estimate of 30 at. % Si. The origin of the Si is not clear. A layer of Cu evaporated in the same UHV system contained no Si as determined by EPMA with a detection limit < 35 ppm Si, so the UHV system itself and the Cu source are not suspected.

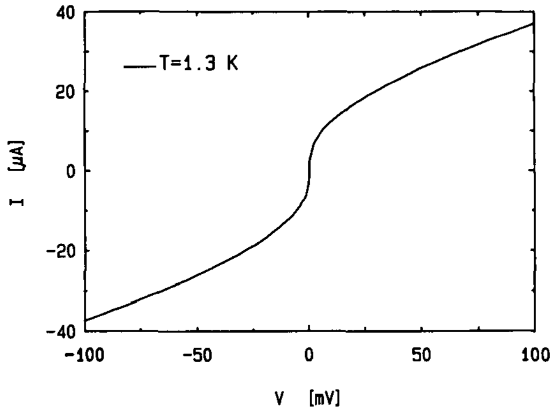

fig.5 I-V characteristic of a line obtained with Ar ion beam etching. Dimensions of the line: 20 μm x 2000 μm. T = 1.3 K.

Efforts to improve the width of the resistive transition were not very successful. We believe this is caused by a chemical reaction of the evaporated material with the substrate. Our conclusion, which is in agreement with Hammond et al. [9], is based on several observations. EPMA before and after annealing yielded a different metal composition. The resistive transition was not much influenced by considerable changes in metal composition or annealing procedure for temperatures between 750 and 800 °C. With an annealing temperature of 900°C the $BaAl_2O_4$ crystal structure could be identified by X-ray diffraction. After removal of the superconducting layer with a 10% solution of acetic acid, a thin transparent layer of about 30 nm thickness was found to remain. Although these observations show evidence for chemical reactions, we could not detect Al with EPMA in the films we used for our measurements. Also the relation between the resistive transition and the large grain structure detected in the films is not clear. Other measurement techniques are applied at present to obtain more information concerning the material inside the grain.

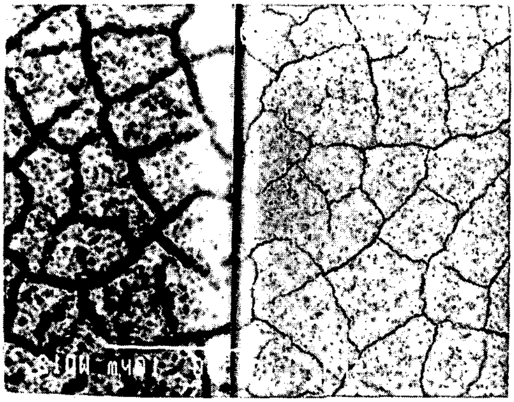

fig.6 Surface of an Y1Ba2Cu3O7-y film after anneal. Backscattered electrons are used for image formation. In the right hand half of the figure, 90 % of the film thickness has been removed by Ar etching. The bar is 10 mm. (V=25kV, substrate perpendicular with respect to beam).

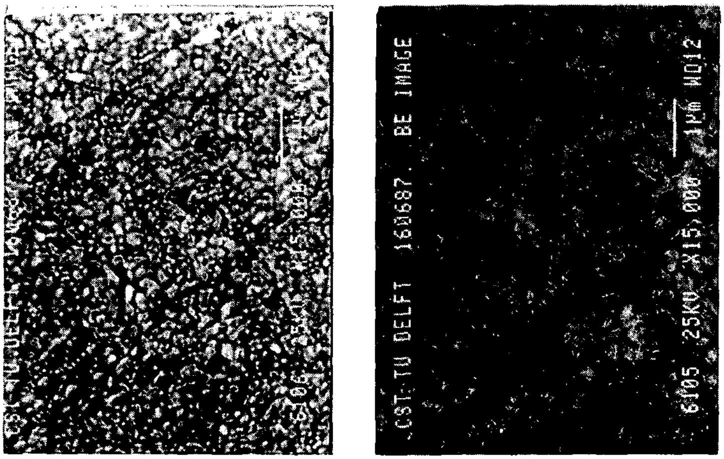

fig.7 Surface of an $Y_1Ba_2Cu_3O_{7-y}$ film after anneal. Detail from fig. 6. Upper photograph is a secondary electron image (SE), the lower is a backscattered image (BE). The bar is 1 µm. (V=25kV, substrate perpendicular with respect to beam).

CONCLUSIONS

It seems unlikely that high-T_c $Y_1Ba_2Cu_3O_{7-y}$ can be obtained during growth by straightforward evaporation of metals and the application of a beam of molecular oxygen. A minimum requirement to form high-T_c $Y_1Ba_2Cu_3O_{7-y}$ is the oxidation of copper, which does not occur at the attainable values of the effective oxygen pressure on the substrate. The use of an oxygen ion beam may be advantageous.

The magnetic field dependence and the strong increase of resistance in narrow lines indicate that the tail in the resistive transition is associated with the detected grain boundaries on a scale of several micrometers. The material within the grains has a reduced onset temperature and a broadened transition, as seen in the upper part of the R(T) curve. This might well be caused by impurity phases, for example due to chemical reactions with the substrate.

Acknowledgment: This work has been supported by the Dutch foundation for Fundamental Research (F.O.M.). We thank all those at our Delft University of Technology who made the fabrication and analysis of these films possible. We thank L. Demaegd and L. de Wulff of Bekaert Belgium for help with the scanning Auger analysis.

REFERENCES

1 J.G. Bednorz and K.A. Müller, Z. Phys. B **64**, 189 (1986)

2 M.K. Wu, J.R. Ashburn, C.J. Torng, P.H. Hor, R.L. Meng, L. Gao, Z.J. Huang, Y.O. Wang, and C.W. Chu, Phys. Rev. Lett. **58**, 908 (1987)

3 P. Chaudhari, R.H. Koch, R.B. Laibowitz, T.R. McGuire and R.J. Gambino,.Phys. Rev. Let. **58**, 2684 (1987)

4 M. Naito, R.H. Hammond, B. Ho, M. Hahn, J.W.P. Hsu, P. Rosenthal, A.F. Marshall, M.R. Beasley, T.H. Geballe and A. Kapitulnik, submitted to J. Material Res.

5 K.Y. Yu, W.E. Spicer, I. Lindau, P. Pianetta and S.F. Lin, Surface Science **57**, 157 (1976)

6 C.R. Guarnieri, S.D. Offsey, J.J. Cuomo, J. Vac. Sci. Technol (to be published)

7 F.H. Smyth and H.S.Roberts, J. American Chem. Soc. **42**, 2582 (1920)

8 A.J. Allmand, J. Chem. Soc. **95** , 2163 (1909)

9 R.H. Hammond, M. Naito, B. Ho, M. Hahn, P. Rosenthal, A. Marshall, N. Missert, M.R. Beasley, A. Kapitulnik, and T.H. Geballe, Extended Abstracts MRS symposium on High Temperature Superconductors, Anaheim, California, April 23-24, 1987

APPENDIX I

GROWTH AND CHARACTERISATION OF A SINUSOIDALLY MODULATED NB/V SUPERLATTICE

R.H.M.van de Leur, A.J.G.Schellingerhout, J.E.Mooij and F.Tuinstra

Department of Applied Physics, Delft University of Technology.
Delft, The Netherlands

A modulated superlattice has been fabricated of Nb and V with sinusoidal variation of composition. This variation has been imposed during growth by modulating the deposition rates. X-ray diffraction shows the sample to be monocrystalline

In recent years there have been several reports on metallic superlattices and layered structures [1..4]. They concern the alternate deposition of two materials. Often interdiffusion smoothes the interface between the layers causing an interface of a few atomic layers of an alloy. We report the growth of a metallic superlattice with a sinusoidal composition modulation that has been imposed during the growth by modulating simultaneously the deposition rates of the two metals Nb and V. These elements both have the b.c.c. structure. We succeeded in making a metallic superlattice with a small mosaic spread (1.5 deg) and a long coherence length (50 nm) in spite of the 10 percent difference in lattice constant of the pure materials.

The superlattice was grown on a sapphire (012) substrate by electron beam evaporation. In our UHV apparatus the evaporation rates are controlled by a feedback system in which the actual evaporation rates are sampled by a mass spectrometer. We made films of Nb and V under the deposition conditions given by O'Neal and Wyatt [5,6]; i.e. a depostion rate of 1.0 nm/s and a substrate temperature of 1070 K. During evaporation the initial residual gas pressure of 10^{-8} Pa rose to 5×10^{-6} Pa (mainly hydrogen) when Nb was deposited at a rate of 1.0 nm/s. A Nb film of 1 μm thickness deposited under these conditions had a superconducting critical temperature of 9.1 K and a resistance ratio R_{293}/R_{10} of 40.

The sinusoidal deposition rates, which were chosen to avoid too large stresses in the superlattice, are given by

$$R_{Nb} = 1.3 + 0.9 \sin(2\pi\nu\cdot t)$$

$$R_{V} = 1.2 - 0.9 \sin(2\pi\nu\cdot t) ,$$

with $\nu = 0.10\ s^{-1}$, in atomic layers of the pure materials per second.

Due to the large diffusion constants of Nb and V at 1070 K the given deposition conditions led to an alloy when both materials were deposited with these sinusoidal rates. Lower substrate temperatures resulted in a powder diffraction pattern, sometimes with strong texture, depending on temperature.

To avoid interdiffusion, which is inherent to high temperature, and also have epitaxial growth, which is strongly dependend on the substrate material, we first deposited a thin (10nm) layer of the alloy NbV on a substrate at 1070 K. The superlattice with a thickness of 400 nm was grown on top of this layer at a relative low temperature of 400 K. We now observed a single crystal diffraction pattern. (see fig.1)

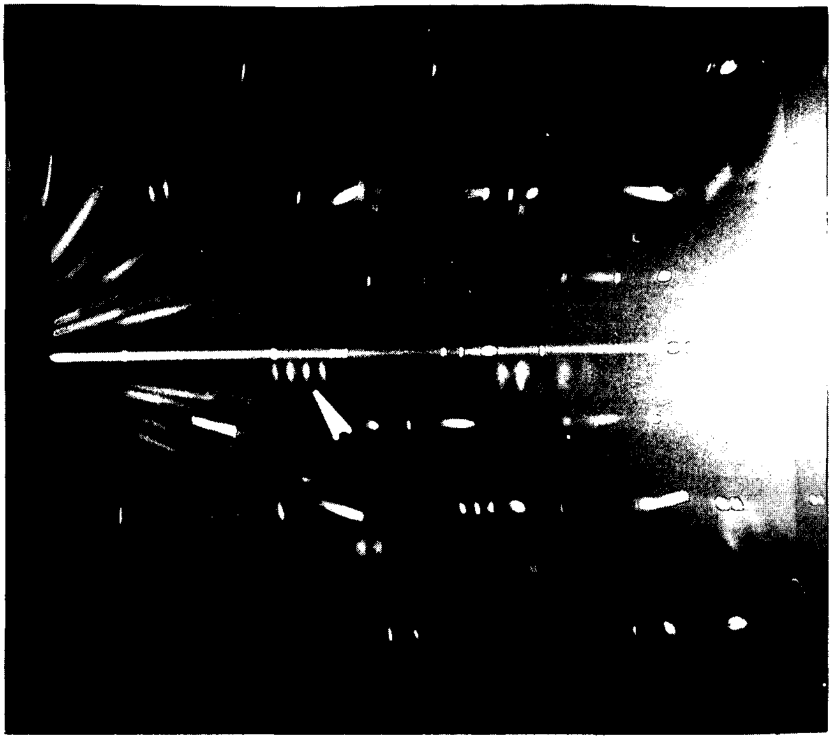

fig.1 Oscillation photograph of the superlattice and the substrate. The arrow points towards the (002) main reflection (at 2θ is 58.6 deg.,Cu radiation) flanked by its satellites. At the left hand side the beamstop.

The orientation of the superlattice is roughly given by

$$(001)_{sl} \,//\, (012)_{sapphire} ,$$

$$[\bar{1}10]_{sl} \,//\, [100]_{sapphire} .$$

We have to draw attention to the fact that the (001) plane of the superlattice and the (012) plane of the sapphire are not exactly parallel but make an angle of about 3 degrees. This offset also has been seen by Hertel et al.[7] for Nb/Ta multilayers on sapphire. The modulation vector is perpendicular to the (012) plane of the sapphire (see fig.1), which was also shown by optical reflection to be the substrate surface. An angle of 3 degrees is also found by Florjancic et al.[8] between the (110) of Nb and the (001) of sapphire and by us between the (001) of Nb and the (012) of sapphire.

Because Nb and V have different lattice constants, a modulation in the density induces a modulation in the lattice constant. If we assume that the lattice constant of a NbV alloy varies linearly with the Nb fraction [9] a cubic average lattice is to be expected. A nonlinear variation would result in a tetragonal lattice.

Small angle diffraction only gives information about the modulation in the electron density because the modulation in the lattice constant does not contribute to the satellite reflections of the direct beam. Small angle diffraction at the superlattice gave only a first order peak within the detection limit (5×10^{-4}), proving that the superlattice has a sinusoidal electron density distribution or nearly so. This (0001) reflection is very narrow, proving that the density modulation is of high quality over a large distance.

To see whether the sinusoidal rates also led to a sinusoidal lattice constant distribution we used a simple one dimensional model with average lattice constant a, in which both the relative electron density $1 + A\cdot\cos(2\pi na/\Lambda)$ and the lattice spacing $a - B\cdot\sin(2\pi na/\Lambda)$ are sinusoidally modulated with a period Λ and amplitudes A and B respectively. The intensity of the diffracted X-ray for such a superlattice is in good approximation given by the Fouriertransform of the elctron distribution peaked at the atomic sites :

$$I_0 f^2(\theta) \frac{1}{\sin\alpha}[\,1 + \frac{mA}{\xi}]^2\, J_m{}^2(\xi)$$

where

f = average atomic form factor.

$1/\sin\alpha$ = geometric factor, α is the angle between the substrate surface and the lattice plane.

J_m = mth order Bessel function.

$\xi = 2\pi B(\frac{1}{a} + \frac{m}{\Lambda})$.

I_0 = scaling constant including the Lorentz-polarisation constant and absorbtion correction.

This model was used to fit the measured intensities of several main reflections and their satellites. In figure 2 we show the ω-2θ scan through the (103m) reflections, where each peak is separately scanned by a one circle diffractometer. The intensities calculationed with the parameters a= 0.315 nm, Λ= 3.48 nm, A= -0.34 and B=0.33 are also given. This fit shows that our model gives a reasonable good description of the superlattice in spite of the fact that the intensities of the satellites are very sensitive to small variations in the parameters. In fact the adequateness of this model is limited by the accuracy of the deposition rates. The parameters indicate that there is no observable diffusion, which would result in smaller amplitudes, of the constituents.

We have shown that it is possible to fabricate a monocrystalline metallic superlattice with a preliminary imposed sinusoidal modulation in spite of a lattice mismatch of 10% between the pure materials.

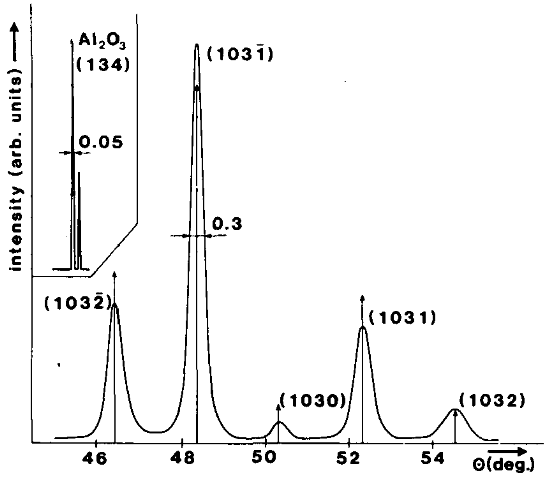

fig.2 The (103) main reflection and its satellites. The instrumental broadening is indicated by the (134) reflection of the substrate.

Acknowledgment: This project is supported by the Foundation for Fundamental Research (F.O.M.).

REFERENCES

[1] D.B.McWhan et al., J.Appl.Phys.54,3886 (1983).
[2] S.M.Durbin et al., J.Phys.F 11, L223 (1981).
[3] I.K.Schuller, Phys.Rev.Lett.24, 1597 (1980).
[4] M.G.Karkut et al., Phys.Rev.B.32,4800 (1985).
[5] J.E.O'Neal and R.L.Wyatt, Thin Films 2, 71 (1971).
[6] J.E.O'Neal and R.L.Wyatt, Thin Films 2, 1 (1971).

[7] G.Hertel et al., Superconductivity in d- and f-band Metals, W.Buckel and W.Weber eds.,1982.

[8] M.Florjancic et al. J.de Phys.Coll C4, 129 (1985).

[9] H.A.Wilhelm et al. J.of Metals 6, 915 (1954).

APPENDIX II

CRITICAL MODULATION AMPLITUDE IN MONOCRYSTALLINE NB/V AND TA/V SUPERLATTICES

R.H.M.van de Leur, A.J.G.Schellingerhout, F.Tuinstra and J.E.Mooij

Department of Applied Physics, Delft University of Technology
Delft, The Netherlands

Superlattices of Nb/V and Ta/V with an average concentration of 50% V and a sinusoidal modulation of the concentration have been fabricated. Monocrystalline growth is only obtained up to a critical value of the modulation amplitude, which corresponds to a maximum V concentration of about 85% in both types of superlattices. At this critical amplitude the strain energy is about one half of the energy of a superlattice with a maximum V concentration of 100%. The period of modulation, varied between 1 and 12 nm, has been found to have no influence on the critical amplitude .

INTRODUCTION

The growth of layered metallic structures and modulated alloys of transition metals has been extensively reported in literature[1]. Particularly the Nb/Ta superlattice[2,3] has attracted much attention. Because Nb and Ta have the same lattice constant, there are no strain effects in the superlattice and monocrystalline growth is easily achieved. We report the growth of Nb/V and Ta/V superlattices; here the constituent metals have a difference in lattice constant of 10%. To minimize the elastic energy in the superlattices the variation in the concentration is chosen to be sinusoidal. Nb and V[4] as well as Ta and V[5] form solid solutions for every concentration of V. A two phase region has been reported below 1573 K in TaV alloys[5,6,7]. We found no evidence for a second phase in our deposited films.

GROWTH

The superlattices were grown in a UHV apparatus with two electronbeam evaporators by modulating the evaporation rates of the constituent metals simultaneously of opposite phase. The rates are controlled with a mass spectrometer in a feedback loop. The superlattices were grown on (012) α-Al_2O_3 substrates. In order to initiate epitaxial monocrystalline growth, a 10 nm thick buffer layer of the corresponding alloy was deposited on the substrate at 1070 K. Subsequently the substrate temperature was reduced to ~450 K and the deposition rates were modulated. The resulting superlattices have a typical thickness of 500 nm. The growth direction was (001). Due to shadow effects of the substrate holder, a narrow line of the pure materials was deposited at the edges of the superlattice. By measuring the thickness of these strips with an alpha-step (Tencor) we checked the average composition of the superlattices. In a previous paper[9] we showed the absence of interdiffusion or decomposition in a Nb/V superlattice; accordingly the concentration variation remains sinusoidal.

For both the NbV[4] and the TaV[8] alloy there is a small deviation from Vegard's law. In a first approximation the lattice constants of the alloys change linearly with compositions. Therefore the superlattices will be strained periodically. No strain is to be expected from the epitaxial growth on the substrate. The epitaxial films of Nb,Ta,V and the alloys NbV and TaV, 200nm thick, on the α-Al_2O_3 substrate showed no deviation from the bulk lattice constants. The lattice mismatch between the substrate and the film apparently is accommodated in a very thin layer. The strain effects of the epitaxial growth thus are removed from the superlattices by the buffer layer. In our case the buffer layer is in fact the substrate for the superlattice.

ELASTIC ENERGY

For a cubic crystal with isotropic strain ($\varepsilon_{xx} = \varepsilon_{yy}$) in the (001) or xy plane, there are no shear stresses and the elements of the stress tensor are given by

$$\sigma_{xx} = \sigma_{yy} = (c_{11} + c_{12})\varepsilon_{xx} + c_{12}\varepsilon_{zz}$$
$$\sigma_{zz} = 2c_{12}\varepsilon_{xx} + c_{11}\varepsilon_{zz}$$
$$\sigma_{xy} = \sigma_{yz} = \sigma_{zx} = 0,$$

where c_{11} and c_{12} are the stiffness constants. In the case of free relaxation in the z-direction, the strain in this direction is

$$\varepsilon_{zz} = -2(c_{12}/c_{11})\varepsilon_{xx} \,,$$

and the elastic energy per volume is determined only by the elastic constants and the strain in the xy plane, i.e.

$$f' = \varepsilon_{xx}{}^2.\kappa \; = \varepsilon_{xx}{}^2.\frac{E}{1-\nu}$$

with κ equals $c_{11} + c_{12} - 2c_{12}{}^2/c_{11}$, E the Young modulus and ν the Poisson constant. In a monocrystalline superlattice, modulated in the z-direction, the lattice parameter parallel to the xy plane is constant throughout the whole crystal.

With a rectangularly modulated superlattice (multilayer) it is possible to determine the elastic constant κ for the two materials which form the layered structure, even beyond the elastic limit as long as the sample remains monocrystalline. In a multilayer composed of the materials A and B (one, or even both might be alloys) with lattice constants a and b respectively, the lattice constant X in the xy plane is given by

$$X \; = a\cdot[1 + \varepsilon_{xx}(A)] = b\cdot[1 + \varepsilon_{xx}(B)],$$

and thus $\varepsilon_{xx}(A)$ and $\varepsilon_{xx}(B)$ can be measured.The elastic energy per surface area, averaged over the whole sample is

$$f = d_A.f'(A) + d_B.f'(B) \;,$$

with d_A and d_B the thickness of the layers A and B respectively. Minimizing f with respect to

$\varepsilon_{xx}(A)$ (or $\varepsilon_{xx}(B)$) gives an expression for $\varepsilon_{xx}(A)$ in terms of $\kappa(A)$ and $\kappa(B)$. When one of the κ's is known, the other one can be calculated. On the other hand, if both κ's are unknown, a second multilayer with different (d_A,d_B) is needed to determine the elastic constants.

In a sinusoidally modulated superlattice A/B the concentration of element A varies from one atomic layer to the other. The concentration of element A in the mth atomic plane of a superlattice with an average concentration of 50% A is then given by

$$c_A(m) = \frac{1}{2}[1 + \eta\cdot\sin(2\pi Xm/\Lambda)],$$

with η the amplitude, Λ the period of the modulation and X the average lattice constant. When the alloy AB of the elements with lattice constants a and b has a lattice constant that varies linearly with the concentration, the strain in the mth atomic plane is given by

$$\varepsilon_{xx}(m) = \frac{X}{X + [c_A(m)-\frac{1}{2}]\delta x} - 1 = -[c_A(m) - \frac{1}{2}]\cdot\frac{\delta x}{X}[1 - \{c_A(m) - \frac{1}{2}\}\cdot\frac{\delta x}{X}],$$

with δx the difference in lattice constants of the constituent elements. In the second expression we omitted higher order terms. Of course, for bcc lattices the lattice constant has to be divided by two to get the appropriate number of atomic planes. When we use the same elastic constant κ throughout the superlattice, the elastic energy

$$f' = \int \kappa\,\varepsilon_{xx}^2(m)\,dm$$

is given by

$$f' = \frac{1}{2}\kappa\cdot\left(\frac{\eta\,\delta x}{2X}\right)^2$$

and thus independent of the modulation period Λ, as derived also by Cahn[10].

RESULTS AND DISCUSSION

In Fig.1 the composition and the modulation period of the fabricated Nb/V and Ta/V sinusoidally modulated superlattices are shown. The vertical lines indicate the range of the composition variation in the superlattice. Superlattices indicated with full lines are monocrystalline. The crystallinity of the superlattices has been determined by a Debye-Scherrer type of X-ray photographs. The criterium for monocrystalline growth was the absence of additional broadening of the diffraction spots with respect to the alloys films. The maximum concentration of V for monocrystalline growth is 88% (η=0.76) and 84% (η=0.68) for Nb/V and Ta/V respectively, as can be seen in Fig.1. The elastic constants[11] and the lattice parameters as measured for thin epitaxial layers on (012) sapphire of Nb, Ta and V are given in Table 1.

Table 1. Elastic constants and lattice parameters

	Nb	Ta	V	
a	0.3300	0.3298	0.3029	±0.0005 nm
c_{11}	246	267	228	GPa
c_{12}	134	161	119	GPa
c_{44}	28.7	82.5	42.6	GPa
κ	234	234	223	GPa

With Vegard's law, this yields the values 0.032 and 0.029 for $\eta\delta x/2X$ of Nb/V and Ta/V respectively. In other words, the maximum strain ε_{xx} in Nb/V is 3.2% and in Ta/V 2.9%. This is much less than the 4.3% corresponding to a superlattice with modulation amplitude η = 1. If we take for κ a value averaged over the constituent elements, the maximum strain energies for Nb/V and Ta/V are 0.12 and 0.10 GJ/m^3 respectively.

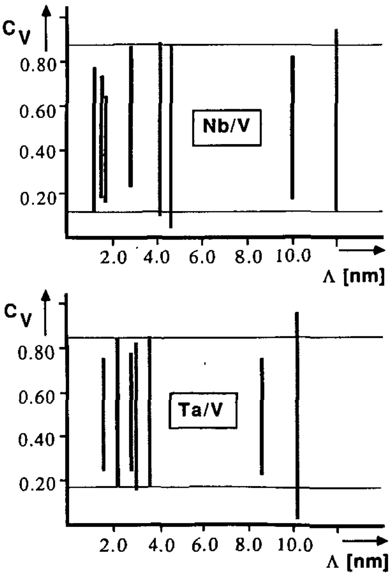

Fig.1 Concentration variation and modulation period of the sinusoidally modulated superlattices. Full lines indicate monocrystalline samples.

CONCLUSION

We have shown that the monocrystalline growth of sinusoidally modulated Nb/V and Ta/V superlattices with an average concentration of 50% V is limited by a critical amplitude of modulation η of about 72%, corresponding to a maximum strain energy of about 0.11 GJ/m^3 (11 meV /atom). This energy is only half the elastic energy of a superlattice with a modulation amplitude η of 100%.

Acknowledgement: This work is supported by the Foundation for Fundamental Research on Matter (F.O.M.)

REFERENCES

1. see e.g. Synthetic Modulated Structures, (L.L.Chang & B.C.Giessen eds.), Academic Press, 1985
2. S.M.Durbin, J.E.Cunningham, M.E.Mochel and C.P.Flynn, J.Phys.F. 11, L223 (1981)
3. Y.Nishihata, M.Nakayama, H.Kato, N.Sano and H.Terauchi, J.Appl.Phys. 60, 3523 (1986)
4. H.A.Wilhelm, O.N.Carlson and J.M.Dickinson, Trans.AIME 6, 915 (1954)
5. W.Rostoker and A.Yamamoto, Trans.ASM 46, 1136 (1954)
6. O.N.Carlson, D.T.Eash, and A.L.Eustice, Proc.AIME 2, 277 (1959)
7. A.P.Nefedov, E.M.Sokolovskaya, A.T.Grigor'ev, I.G.Sokolova, and N.A.Nedumov, Russ.J.Inorg.Chem. 9, 486 (1964)
8. V.N.Eremenko, L.A.Tret'yachenko and R.I.Yakhimovich, Russ.J.Inorg.Chem. 5, 1110 (1960)
9. R.H.M.van de Leur, A.J.G.Schellingerhout, J.E.Mooij and F.Tuinstra, Solid State Comm. 60, 633 (1986)
10. J.W. Cahn, Acta Metall. 9, 795 (1961)
11. D.I.Bolef, J.Appl.Phys. 32, 100 (1961)

APPENDIX III

A STRONG VOLTAGE DEPENDENCE OF THE CONDUCTIVITY IN GRANULAR ALUMINIUM

A.J.G. Schellingerhout, H.M. Appelboom, J.A. Kokkedee, J.E. Mooij and T.M. Klapwijk*

Department of Applied Physics, Delft University of Technology, Delft, The Netherlands

*Department of Applied Physics, Groningen University, Groningen, The Netherlands

INTRODUCTION

There have been many investigations in the transport properties of granular aluminium near the metal-insulator transition. Our intention is to investigate the electrical conduction of this material on a short length scale in the range of 20 to 1000 Å. This makes it possible to explore the conduction when the length scale of the sample is of the same order as the diverging length scale near the metal-insulator transition. When granular aluminium of this thickness is enclosed between two superconductors, a superconductor-insulator-superconductor (SIS) or a superconductor-normal metal-superconductor (SNS) junction is created and the superconducting properties can be explored, similar to experiments performed by BARRERA and BEASLEY [1] on NbSi. We report results on a length scale of a 1000 Å to investigate the properties of granular aluminium in this regime.

EXPERIMENTAL

The investigated samples consist of a thin granular aluminium layer sandwiched between two good conducting aluminium layers, which serve as electrodes. These layers are evaporated in an UHV-system.The substrate, held at room temperature during deposition, is (012) sapphire. The partial pressure of oxygen and the aluminium deposition rate are controlled with a feedback system. The oxygen pressure is 5.10^{-4} Pa and the aluminium rate is 46 Å/min. The trilayer is evaporated in one continuous run by changing the aluminium rate and the oxygen pressure. Small squares are patterned by a selective anodization process similar to SNAP used by KROGER et al. [2]. The completed structure is drawn in Fig.1

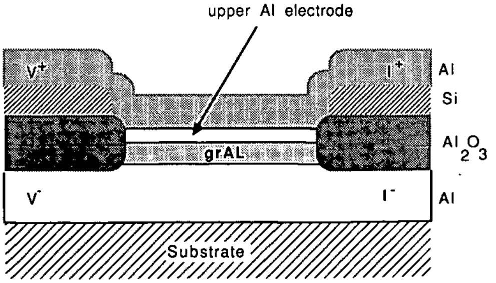

Fig.1 Cross-sectional view of an Al-grAl-Al junction. The barrier thickness is 1000 Å .The area of the junction is 8x8 μm^2. The silicon layer is a protection against shorts

With a second shutter which was opened during the deposition of the 1000 Å granular aluminium layer, we made a layer of the same composition as the barrier on a separate substrate. It is used as a reference for the barrier composition.

MEASUREMENTS

Resistance versus temperature measurements were performed on the junction and on the reference layer. The resistance of the reference layer follows the known relation

$$R(T) = R_o \exp((T_o/ T)^{0.5}) \qquad (1)$$

For this composition T_o was 220 K ,with $r_{4.2\ K}$ of 40 Ω cm.Similar results have been obtained by SIN et al. [3]. The granular aluminium is clearly in the insulating regime. The resistance of the junctions showed the same temperature dependence (1), with an identical T_o , although the measured $\rho_{4.2\ K}$ was surprisingly high : 400 Ω cm.

We observed strong changes in the conductance at higher voltages. The measured I(V) characteristics are shown in Fig.2 on logarithmic scales. Changing the measurement voltage for example from 0.1 to10 mV, leads to conductance changes of three orders of magnitude. At high voltages all the curves seem to converge to the same curve, independent of temperature

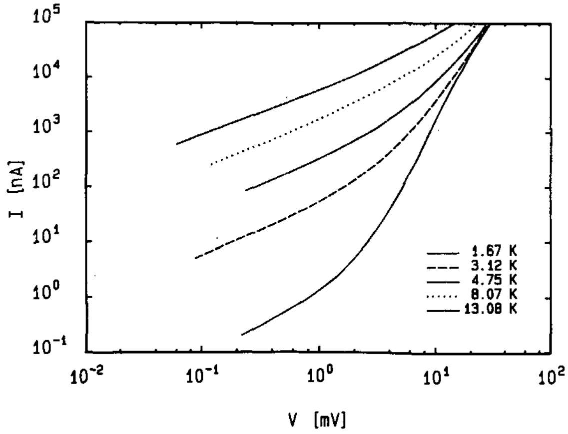

Fig.2 I(V) characteristics of a 8x8 μm^2 Al-grAl-Al junction.

DISCUSSION AND CONCLUSION

A possible explanation for the non-ohmic conduction is the high electric field in the granular aluminium. Strong field effects have been observed by others (see MOTT and DAVIS[4] and EFROS and POLLAK [5]). We compare the thermal energy $k_B T$ to the energy gained by an electron in an electric field eEL_E, with L_E a characteristic length. We propose the following qualitative model. At low field the conduction is governed by the temperature according to (1), at high fields the conduction is dominated by the electric field and hence independent of temperature.

We can define a cross-over field

$$e E_c L_E \approx k_B T \qquad (2a)$$

and hence a cross-over voltage

$$V_c = E_c d \qquad (2b)$$

with d the thickness of the barrier. In Fig. 3 we have plotted the derivative dV/dI of the I(V) curves. We have found that the high voltage behaviour can be fitted to the relation

$$dV/dI = R_o \exp((V_o / V)^{0.5}) \qquad (3)$$

with R_o and V_o arbitrary constants. To obtain a cross-over voltage V_c from the experimental data in Fig.3 we used the voltage where the dV/dI at zero voltage equals (3). In Fig.4 the values of V_c are plotted versus the temperature

With Fig.4 and (2) it is possible to make an estimate for L_E which is about 50 Å. This value is compatible with distances between localized states or different grains.

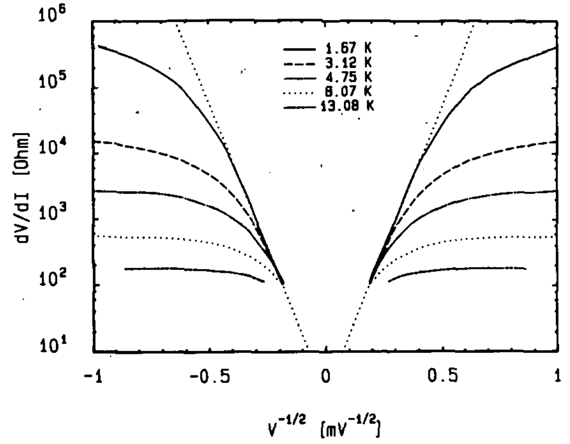

Fig.3 Differential resistance dV/dI versus the inverse voltage across an 8x8 μm^2 junction. The extra dotted straight line is a least squares fit to (3).

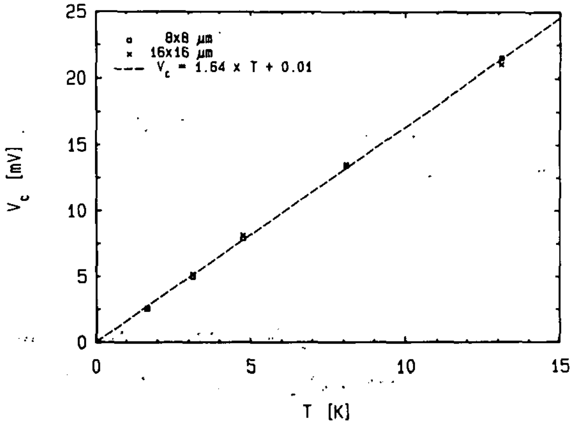

Fig.4 Cross-over voltage V_c versus temperature for two samples (8x8 μm^2 and 16x16 μm^2). The line is a least squares fit for all the data.

With Fig.4 and (2) it is possible to make an estimate for L_E which is about 50 Å. This value is compatible with distances between localized states or different grains.

In conclusion, we have observed a strong voltage dependence of the resistance in granular aluminium, which can be explained with an electric field effect. This effect should also be observable in lines of granular aluminium although it might be difficult to distinguish the electric field effect from a heating effect. We realize the necessity for junctions with a different barrier thickness to confirm that the electric field is causing the non-ohmic behaviour.

Acknowledgement: This project is supported by the Foundation for Fundamental Research (F.O.M.).

REFERENCES

1. A.S. Barrera and M.R. Beasley, Applied Superconductivity Conference 1986, Baltimore IEEE trans. mag. to be published
2. H.Kroger, L.N. Smith and D.W. Jillie Appl. Phys.Lett.39(3),(1981),280
3. H.K. Sin, P. Lindenfeld and W.L. McLean Phys.Rev.B30(1984),4067
4. N.F. Mott and E.A. Davis , Electronic processes in non-crystalline materials (Clarendon press, Oxford,1979)
5. A.L. Efros and M. Pollak , Electron-electron interactions in disordered systems (North Holland,Amsterdam,1985)

APPENDIX IV

ION SOURCE

REFERENCES

1 H.R. Kaufman, AIAA J. 15, 1025 (1977)

2 G. Aston, H.R. Kaufman and P.J. Wilbur, AIAA J. 16, 516 (1978)

3 H.R. Kaufman, J.Vac. Sci. Technol. 15, 272 (1978)

4 H.R. Kaufman, J.J. Cuomo and J.M.E. Harper, J.Vac. Sci. Technol. 21, 725 (1982)

5 J.J. Cuomo, J.M.E. Harper and.H.R. Kaufman, J.Vac. Sci. Technol. 21, 737 (1982)

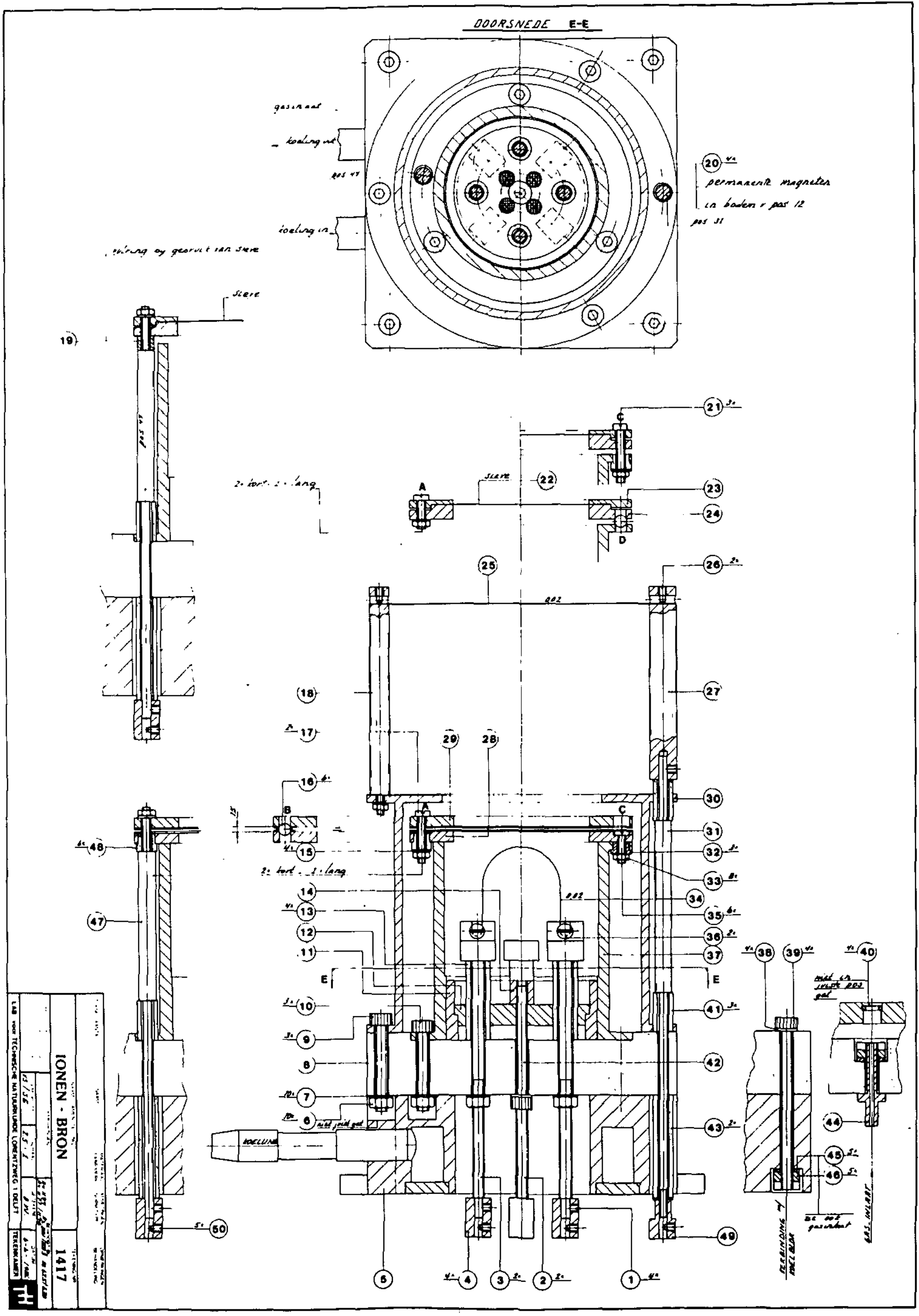
DOORSNEDE E-E
gasinlaat
koeling uit
pos 47
koeling in
20 4x
permanente magneten
in boden v pos 12
pos 31
Steve
19
pos 44
2x kort 2x lang
A
Steve
22
21 3x
23
24
D
25
26 2x
Ø82
18
27
2x 17
29
28
16 6x
B
C
30
31
32 3x
15 4x
33 8x
2x kort 3x lang
34
14
35 6x
13 4x
36 2x
12
37
11
E
E
38 4x
39 4x
40 4x
10 3x
41 3x
9 3x
8
42
7 10x
6 10x
niet juist gat
43 2x
KOELING
44
45 5x
46 5x
5
4 4x
3 2x
2 2x
1 4x
49
50 5x
47
48 6x
verbinding
niet ...
gasinlaat
IONEN - BRON
1417
LAB voor TECHNISCHE NATUURKUNDE LORENTZWEG 1 DELFT
TEKENKAMER
TH

SUMMARY

This thesis contains a number of papers which have at first glance little in common. However the common aspect shared in almost every chapter is the fabrication of complex multilayers and alloys in which a stable evaporation rate is essential. The structures are evaporated with electron guns in an ultra high vacuum system. The evaporation rate is stabilized by applying feedback. Chapter 1, the introduction, deals with the relationship between the chapters and the original aim of this research project. The project was to investigate Josephson junctions with a barrier material with a metal insulator transition.

The next chapter deals with the general principles of rate control of electron gun evaporators. This chapter has been written after four years of experience with feedback systems. Further improvements in the rate stability can be achieved by redesigning electron guns and power supplies.

The coherence of the super period of artificially fabricated superlattices has a relation with the evaporation rate. In chapter 3, a fabricated Si/Ge superlattice has been used to measure the quality of the total feedback loop. The coherence of the super period is measured with x-ray diffraction techniques from which the maximum drift and noise of the evaporation rate during the fabrication is derived. The instabilities in the Si evaporation rate are below 3% during the 30 minutes evaporation process.

A model for the critical layer thickness for dislocation free growth of Si/Ge superlattices and alloys on Si substrates is discussed in chapter 4. The model shows good agreement with experimental results. Layers without dislocations with a thickness beyond the value given by the model can be fabricated. However the layers will be thermodynamically unstable, as is shown by experiments on superlattices.

Chapter 5 discusses a method for the fabrication of Josephson junctions with a very small capacitance which is achieved by a small area (0,01 μm^2). The fabrication method uses reactive ion beam etching and shadow evaporation techniques.

Granular aluminium is a material which is often used for the investigations in weak and strong localization and superconducting properties. In chapter 6, the oxygen concentration of the granular aluminium is determined for layers with several resistivities. This information is

used for a better understanding of the microstructure of the material. The measured oxygen concentrations in relation with the resistivities cannot be understood with the commonly used microstructure model.

The resistance of granular aluminium shows a strong dependence of the electric field. This effect is discussed in chapter 7. The measurements are interpreted with two models for electric field effects. The model based on variable range hopping with a coulomb gap in the density of states shows the measured electric field dependence.

The final chapter deals with the fabrication of thin layers of the high T_c superconductor $Y_1Ba_2Cu_3O_{7-y}$ on sapphire substrates. The copper could not be oxidized during the evaporation process, as is inferred from x-ray measurements. The superconducting crystal structure could only be fabricated after annealing in oxygen. The onset of the superconductivity was 80-90 K. However, zero resistance is only achieved at 30-40 K.

SAMENVATTING

Dit proefschrift bevat een aantal publicaties die op het eerste gezicht weinig gemeen hebben. De rode draad door dit proefschrift is de fabricage van complexe multilagen en legeringen waarbij een goed gecontroleerde opdampsnelheid essentieel is. De opgedampte structuren zijn gefabriceerd met electronenstraalverdampers in een ultrahoog vacuum systeem. De stabiliteit van de opdampsnelheid wordt bereikt door middel van terugkoppeling. Hoofdstuk 1, de introductie, beschrijft de relatie van de hoofdstukken, die geschreven zijn als aparte publicaties, met de doelstelling van het onderzoek. Zoals blijkt uit de introductie is deze doelstelling niet bereikt.

Het volgende hoofdstuk behandelt de algemene principes van het terugkoppelen van electronenstraalverdampers. Het is geschreven na vier jaar ervaring met dit type terugkoppelsysteem. Er worden in dit hoofdstuk ook enige suggesties gedaan voor verdere verbeteringen van de stabiliteit van de verdampingsnelheid.

De coherentie van de opgedampte kristallijne kunstmatige superroosters heeft een eenduidige relatie met de opdampsnelheid. In hoofdstuk 3 wordt met een opgedampt Si/Ge superrooster de kwaliteit van het totale terugkoppelsysteem gemeten. Met röntgendiffractie wordt de coherentie van de superperiode gemeten, waarmee een afschatting gemaakt kan worden van de maximale instabiliteit en drift van de opdampsnelheid gedurende het opdampen van het superrooster. De variatie in de silicium opdampsnelheid is volgens deze analyse kleiner dan 3% gedurende 30 minuten.

Een model voor de kritische laagdikte voor de groei van Si/Ge legeringen en superroosters zonder dislocaties op Si substraten wordt behandeld in hoofdstuk 4. Het model laat een goede overeenstemming met experimenteel bepaalde kritische laagdikte zien. Lagen van Si/Ge met een dikte groter dan de kritische laagdikte volgens dit model kunnen echter wel gemaakt worden. Deze lagen zijn dan thermodynamisch instabiel zoals blijkt uit experimenten verricht aan een superrooster.

Hoofdstuk 5 beschrijft een methode voor het maken van Josephson juncties met een zeer klein oppervlak (0.01 μm^2). De methode is gebaseerd op reactief ionen etsen in combinatie met schaduw-opdamptechnieken.

Granulair aluminium is een veel gebruikt materiaal voor onderzoek naar zwakke en sterke localisatie en voor onderzoek naar supergeleidende eigenschappen. In hoofdstuk 6 wordt geprobeerd met behulp van de gemeten zuurstof concentratie nieuwe inzichten te verkrijgen in de microstructuur van dit materiaal. Deze zuurstof-concentratie metingen, in relatie tot de gemeten soortelijke weerstand, kunnen niet in overeenstemming gebracht worden met het bestaande model van de microstructuur voor granulair aluminium.

Granulair aluminium blijkt een sterke elektrisch-veld-afhankelijkheid van de weerstand te hebben. Hoofdstuk 7 behandelt metingen aan dit effect. Deze metingen worden vergeleken met bekende theoretische modellen voor het electrisch-veld-effect. Het model met 'variable range hopping' met een 'Coulomb gap', geeft de correcte electrisch-veld-afhankelijkheid van de weerstand.

Het proefschrift wordt afgesloten met een hoofdstuk over de fabricage van dunne lagen van de nieuwe hoge T_c super geleider $Y_1Ba_2Cu_3O_{7-y}$. De ervaring met het constant houden van de opdampsnelheid is gebruikt voor een voorspoedige fabricage van dit materiaal, waarbij drie fluxen gecontroleerd moesten worden. Met röntgendiffractie metingen wordt aangetoond dat het koper gedurende het opdampproces niet geoxideerd wordt. De supergeleidende kristalstructuur kon alleen gemaakt worden na uitstoken van de lagen in een zuurstof atmosfeer. De supergeleiding begint te ontstaan bij 80-90 K. De weerstand werd pas nul bij ongeveer 30-40 K.

LEVENSLOOP

A.J.G. Schellingerhout

Aug 1960		Geboren op 26 augustus te Gouda
Aug 1972-	Juni 1978	Middelbaar onderwijs aan de Rijksscholengemeenschap te Gouda. Eindexamen: Atheneum b.
Sept.1978-	Nov 1983	Studie Technische Natuurkunde aan de Technische Hogeschool te Delft. Afstudeer vakgroep: Fysische Kristallografie.
Dec 1983-	Sept 1986	Promotie onderzoek aan de Technische Hogeschool Delft in de vakgroep vaste stof-supergeleiding o.l.v. Prof. J.E. Mooij and Prof T.M. Klapwijk.
Okt 1986-	Nov 1986	Consultant bij Westinghouse R&D center Pittsburgh U.S.A.
Dec 1986-	Dec 1987	Voortzetting promotie onderzoek.
Jan 1988-		Militaire dienst
April 1988-		Adviseur bij I.S.A. Riber Frankrijk.